A.C. Susceptibility and Magnetoresistivity Measurements on Amorphous FeZr Alloys

by

Hao Ma

A thesis
presented to the University of Manitoba
in partial fulfillment of the
requirements for the degree of
Master of Science
in
Physics

Winnipeg, Manitoba

ISBN 0-315-63234-8

A.C. SUSCEPTIBILITY AND MAGNETORESISTIVITY MEASUREMENTS ON AMORPHOUS FeZr ALLOYS

BY

HAO MA

A thesis submitted to the Faculty of Graduate Studies of the University of Manitoba in partial fulfillment of the requirements of the degree of

MASTER OF SCIENCE

I hereby declare that I am the sole author of this thesis.
I authorize the University of Manitoba to lend this thesis to other institutions or individuals for the purpose of scholarly research.

Hao Ma

I further authorize the University of Manitoba to reproduce this thesis by photocopying or by other means, in total or in part at the request of other institutions or individuals for the purpose of scholarly research.

Hao Ma

The University of Manitoba requires the signature of all persons using or photocopying this thesis. Please sign below, and give address and date.

Abstract

The A.C. magnetic susceptibility and magnetoresistivity of a series of amorphous $Fe_{100-x}Zr_x$ samples with x=8,9,10,11 have been measured. Critical point exponents determined by A.C. susceptibility measurements show, in each case, that in the asymptotic region γ, β and δ, characterizing the transition at T_c exhibit values close to those calculated for the isotropic 3-D Heisenberg model, while the effective Kouvel-Fisher exponent, $\gamma^*(T)$, displays a non-monotonic temperature dependence with a maximum value at a temperature above T_c.

The present work also investigated the spontaneous resistive anisotropy (SRA) of each sample, which basically is the difference between the longitudinal and transverse magnetoresistance extrapolated to zero induction (B). Observations for $Fe_{91}Zr_9$, $Fe_{90}Zr_{10}$ and $Fe_{89}Zr_{11}$ clearly show that a non-zero SRA develops at the ordering temperature T_c, in excellent agreement (within 2%) with the value for T_c obtained from A.C. susceptibility measurements. The onset of a non-zero SRA is a clear indication that ferromagnetic-like order is established at least over a distance comparable with the electron mean free path. This SRA, however, persists to the lowest attainable temperature ($1.5K$) with no obvious change in the vicinity of the proposed transverse-spin freezing temperature, T_{xy}, while the coefficient of the non-linear term in the A.C. susceptibility does exhibit an anomaly in this temperature region.

The interpretation of the magnetic properties of the amorphous $Fe_{100-x}Zr_x$ alloys with $x < 15$ has been a controversial subject for a number of years.

The present work using SRA and non-linear field dependent susceptibility measurements to investigate the magnetic phase transitions are new techniques, which have produced some very interesting data which will certainly contribute to a better understanding of the amorphous $Fe_{100-x}Zr_x$ system. To this end, however, a more detailed study would be desirable.

Acknowledgement

I would like to express my deep appreciation to my supervisor, Professor Gwyn Williams; his helpful comments and suggestions contributed immeasurably to the success of this project. Special thanks are also owed to Dr. Henry Kunkel for his invaluable help throughout the duration of my work.

I would also like to thank Professor J. O. Ström-Olsen for providing some of the samples used in this investigation, Dr. J. Page for providing the apparatus needed for some of the measurements, Mr. Michael S. Westmore for generating the effective exponent plots, and all those who either directly or indirectly assisted me in the completion of my thesis.

Contents

Chapter 1

Theoretical Concepts

Introduction

The magnetic properties and the magnetic phase transitions that are observed in amorphous $Fe_{100-x}Zr_x$ alloys with composition near $x = 10$ have recently attracted much attention. Measurements of the zero-field-cooled magnetization in this system indicate that not only does the magnetization appear abruptly at the ordering temperature, T_c, near $200\,K$, but also a sudden drop of the magnetization is observed at lower temperatures around $50\,K$ (designated T_{xy}) [1][9].

The explanation of these phenomena has generated much controversy, and some of the questions still being debated are as follows:

(1) What kind of magnetic order do these materials really possess in the so called ferromagnetic state ($T_{xy} < T < T_c$)?

(2) What subsequently happens in the so-called re-entrant phase ($T < T_{xy}$)? Does the drop in magnetization correspond to an abrupt vanishing of the spontaneous magnetization, and hence to a well-defined phase transition?

Numerous measurements have been made on the $FeZr$ system near this composition. The techniques used range from macroscopic static magnetization measurement[2] and A.C. susceptibility[3] to microscopic measurements such as small angle neutron scattering (SANS) [4], Mössbauer spectroscopy[5][7], and also direct observation of domain structure using Lorentz transmission electron microscopy[6]. Despite the range of techniques used, the conclusions remain controversial.

A number of authors[2] have observed that the critical exponent values describing the upper "ferromagnetic" transition near T_c are considerably larger than those predicted for the 3-dimensional homogeneous Heisenberg ferromagnet, which seems to indicate that short range magnetic order persists for temperatures well above T_c, possibly because of the amorphous structure. This observation in conjunction with the SANS data of Rhyne and Fish [4] (which show that the spin correlation length $\xi(T)$ fails to diverge at T_c but exhibits an essentially constant value of 23Å down to helium temperatures) leads to the conclusion that the long−range ferromagnetic ordering of the conventional type may not develop in these alloys at any temperature, and the possibility that the system enters a "wandering−axis" ferromagnetic state[7] at T_c has been raised. The lower temperature T_{xy} then indicates the transition to a spin−glass like state with random spin freezing in the xy plane, i.e. transverse spin−glass ordering[5].

By contrast, Kaul *et al.*[3] obtained β, δ, and γ exponent values (in the temperature range very close to T_c) consistent with the 3-D classical Heisenberg model, and hence claimed that the transition at T_c is a true paramagnetic to ferromagnetic one, with T_{xy} again indicating a transition from the ferromagnetic state to a spin glass state (in transverse direction).

A ferromagnetic structure (in the temperature range $6K \leq T \leq 290K$) was suggested by the work of Senoussi and Hadjody[6], which showed that domains as large as $50\mu m$ could be observed using Lorentz transmission electron microscopy. This kind of domain structure, however, was still found to

exist at temperatures lower than T_{xy}, which seems to suggest that this lower temperature "transition" arises from an increase in coercivity at low temperature, rather than from a real phase transition. The magnetic hardness interpretation is strongly supported by Read *et al.* on the basis of their magnetic measurements[8].

In the present work, systematic measurements of A.C.susceptibility and longitudinal and transverse magnetoresistance have been done on a series of $Fe_{100-x}Zr_x$ samples with $x = 8, 9, 10, 11$, in an attempt to clarify the nature of the magnetic ordering that occurs. The remaining sections of Chapter One will give some theoretical background on the magnetic properties of materials; Chapter Two will describe the experimental appartus used in our measurements and the data analysis and discussion will be presented in Chapter Three.

1.1 Critical-Point Exponents and A.C. Susceptibility

1.1.1 Critical-Point Exponents

For many magnetic systems an appropriate order parameter is the magnetization M, because M is a measure of the degree to which the magnetic moments are aligned throughout the crystal. An important means of investigating the onset of magnetic order is through the critical exponents, which describe the behavior of the system near the critical point occuring at temperature $T = T_c$. There are basically three major exponents which are used to describe the static behavior of a magnetic system, these are the spontaneous magnetization or order parameter exponent β, the initial susceptibility exponent γ and the magnetic critical isotherm exponent δ which are defined as[10]:

$$M \sim (-t)^{\beta} \quad \text{when} \quad t \to 0^{-} \ , \quad H = 0 \tag{1.1}$$

$$\chi_T \sim t^{-\gamma} \quad \text{when} \quad t \to 0^{+} \ , \quad H = 0 \tag{1.2}$$

$$M \sim H^{1/\delta} \quad \text{when} \quad t = 0 \ , \quad H \to 0 \tag{1.3}$$

where $t = (T - T_c)/T_c$; $0^{+}(0^{-})$ indicates the approach to $t = 0$ from $t > 0$ ($t < 0$), and H indicates the internal field. The reason we focus on the critical exponents rather than the complete functional form of their behavior is twofold. The first is the fact that, the function describing the magnetic response of the system can be expanded by a power series in field or temperature, and

when considering the behavior sufficiently near the critical point, the leading term in this power series dominates. Hence the critical-point exponents are readily determined, while the complete function may not be. Secondly, as we shall see, the value of these exponents are related to the magnetic order of materials, so by studying these exponents we can obtain information about the magnetic order of a sample.

The theory dealing with critical phenomena attempts to achieve two objectives. The first is to find theoretical models which describe correctly the interaction between the magnetic moments in the material, leading to a determination of the values of the critical-point exponents. The second is to study the relationship between the various exponents. As we will see later the second objective can be achieved using the static scaling law, which is a model independent approach to properties near the critical-point. The static scaling law gives the relationship between the exponents rather than specific numerial values for any of the critical-point exponents.

1.1.2 Theoretical Models

The principal difference between the various models is that they treat the exchange interaction in different ways. These different models generate different sets of critical-point exponents, which are listed in table 1.1.

Mean Field Model

Table 1.1: Theoretical exponent values for various models

Model	β	γ	δ	Ref.
Mean-field Model	0.5	1	3	[1]
3d-Ising Model	0.312	1.25	5	[1]
3d-Heisenberg	0.365	1.386	4.80	[6]
3d-Disordered	0.5	2	5	[7]

The first phenomenalogical theory dealing with ferromagnetism was the mean field model (proposed by Pierre Weiss), in which it was assumed that the spins interact with one another through a molecular field proportional to the average magnetization, i.e. the effective field ($\mathbf{H}_{eff}$), which is given by:

$$\mathbf{H}_{eff} = \mathbf{H} + \lambda \mathbf{M}(T, H), \tag{1.4}$$

where $\mathbf{H}$ is the external field, $\mathbf{M}$ is the magnetization, and λ is the exchange constant. The Hamiltonian of this magnetic system can be written as:

$$\mathcal{H} = -g\mu_B \sum_{i=1}^{N} \mathbf{S}_i \cdot \mathbf{H}_{eff}, \tag{1.5}$$

where $\mathbf{S}_i$ is the spin of the ith atom. A thermal average yields the following

expression for the magnetization

$$M = M_0 B_S(y), \tag{1.6}$$

where

$$M_0 = Ng\mu_B S, \tag{1.7}$$

$B_S(y)$ is the Brillouin function with

$$y = \frac{Sg\mu_B}{k_B T}(H + \lambda M), \tag{1.8}$$

and g, μ_B, k_B, represent the conventional physical constants. A power series expansion of the Brillouin function in the region defined by the critical exponent definitions (Eqs. 1.1−1.3) leads to

$$\beta = \frac{1}{2} \qquad \gamma = 1 \qquad \delta = 3 \tag{1.9}$$

These are the so-called mean field exponents.

Ising Model and Classical Heisenberg Model

A more realistic model explicitly takes the direct inter-atomic exchange interactions into consideration. The interaction Hamiltonian can be written

as:

$$\mathcal{H}^{(D)} = -\sum_{ij} J_{ij} \mathbf{S}_i^{(D)} \cdot \mathbf{S}_j^{(D)}, \tag{1.10}$$

where the parameter D is the spin dimensionality and J_{ij} indicates the interaction strength between atoms i and j. A study of Eq.1.10 allows us to determine the dependence of critical properties on both spin dimensionality D as well as lattice dimensionality, and thereby to examine the predictions of a variety of physical models near their critical points. Of these models only the 3-d Ising model (D=1) and 3-d classical Heisenberg model (D=3) are able to reproduce to a certain extent the existing data for the magnetic system. The former model simplifies the problem by assuming a high degree of uniaxial anisotropy, while the latter assumes a completely isotropic exchange. The forms of the exchange term in these two cases are:

$$\mathcal{H} = -\sum_{ij} J_{ij} S_i^z S_j^z \qquad \text{Ising} \tag{1.11}$$

$$\mathcal{H} = -\sum_{ij} J_{ij} \mathbf{S}_i \cdot \mathbf{S}_j \qquad \text{Heisenberg} \tag{1.12}$$

with the Ising model assuming the spin system possesses two discrete orientations $+1$(up) and -1(down), while the Heisenberg model places no restriction on the orientation of the spins.

Unfortunately both of the above models can not be solved analytically; as a result we can only obtain exponent values using numerical solutions.

Disordered System, S-K Model

The theoretical model for the quenched disordered system was first suggested by Edwards and Anderson[11] and then subsequently solved by Sherrington and Kirkpatrick[12] for the $S = 1/2$ Ising model. This method is referred to as the SK-model, and is applicable to spins which are bond disordered.

In this model they assume that the spins are coupled by infinite-ranged random interactions independently distributed with a Gaussian probability density i.e.

$$\mathcal{H} = -\sum_{i<j} J_{ij} S_i S_j, \qquad S_i = \pm 1 \tag{1.13}$$

with the J_{ij} distributed according to

$$p(J_{ij}) = \left[(2\pi)^{1/2} J\right]^{-1} \exp\left[-\frac{(J_{ij} - J_0)^2}{2J^2}\right] \tag{1.14}$$

where J_0 and J are scaled by

$$J_0 = \frac{\bar{J}_0}{N} \qquad\qquad J = \frac{\bar{J}}{N^{1/2}} \tag{1.15}$$

From this assumption they calculated the phase diagram shown in Fig.1.1 which predicts that the parameters $j = \bar{J}_0/\bar{J}$ and $k_B T/\bar{J}$ determine the magnetic state of a system.

Numerical studies of the SK-like model in the ferromagnetic region[13]

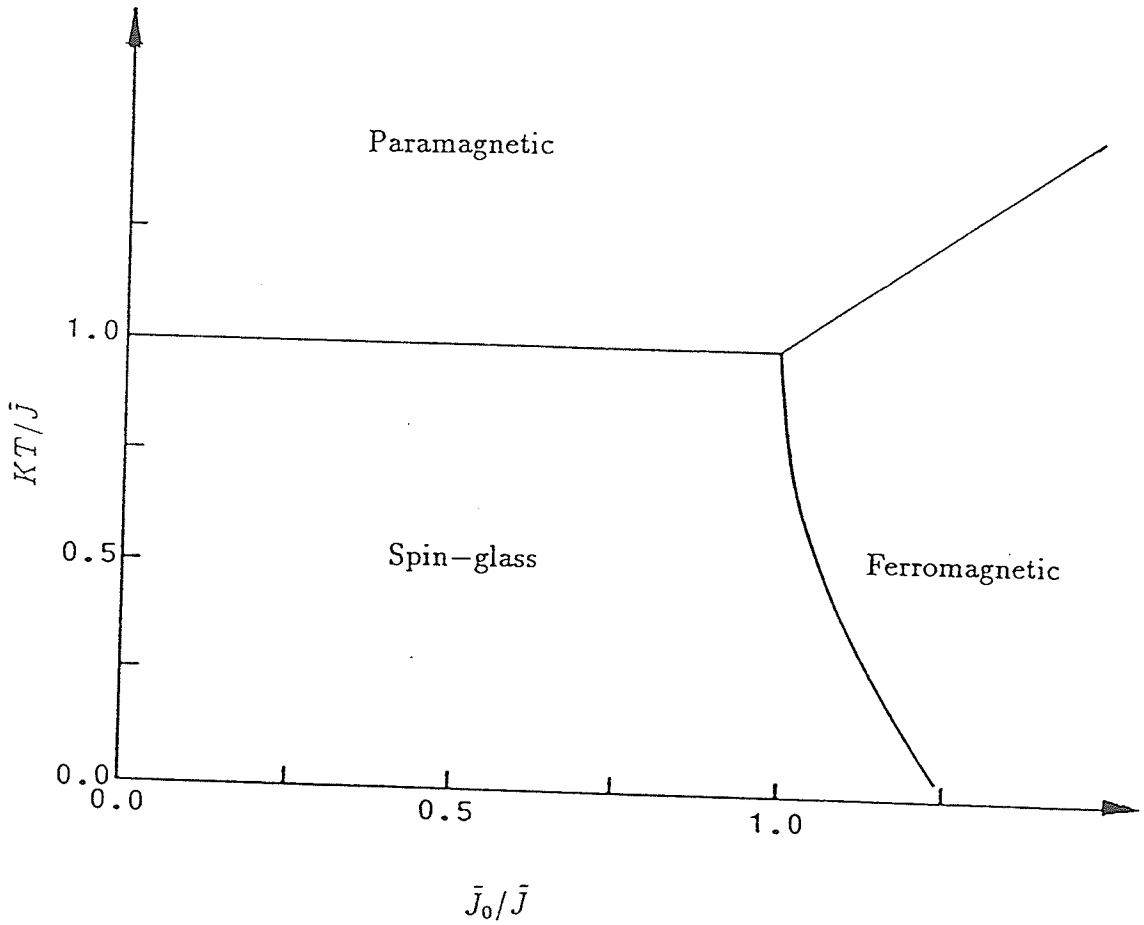

Figure 1.1: Phase diagram of SK-model[12]

indicate that in the ferromagnetic ground state ($1.25 < j < +\infty$) with decreasing j (i.e. with increasing width of the exchange distribution), the width of the true critical region decrease, thus explaining earlier experiment results[14][27][28].

1.1.3 Static Scaling Hypothesis

The static scaling hypothesis asserts[10] that the Gibbs potential $G(t, H)$ is a generalized homogeneous function, which means there exists two parameters a, b , such that $G(\lambda^a t, \lambda^b H) = \lambda G(t, H)$ for any value of the number λ. Since

$$M = -\left(\frac{\partial G}{\partial H}\right)_t \tag{1.16}$$

we can easily obtain

$$M(t, H) = \lambda^{b-1} M(\lambda^a t, \lambda^b H) \tag{1.17}$$

Assuming that the critical fluctuations accompanying the ferromagnetic to paramagnetic transition obey the scaling-law, we can obtain from Eq.1.17 the critical exponents β, γ and δ expressed in terms of these two "scaling parameters" a, b as follows

$$\beta = \frac{1-b}{a} \tag{1.18}$$

$$\gamma = \frac{2b-1}{a} \tag{1.19}$$

$$\delta = \frac{b}{1-b} \tag{1.20}$$

The Widom equality follows as a corollary

$$\gamma = \beta(\delta - 1) \tag{1.21}$$

In addition to the prediction of the relationships between the critical point exponents, the scaling hypothesis makes a specific prediction concerning the form of the magnetic equation of state. By chosing $\lambda = |t|^{-1/a}$ in Eq.1.17 we obtain

$$m(h,t) \sim t^{\beta} F_{\pm}\left(\frac{h}{t^{\gamma+\beta}}\right) \tag{1.22}$$

where m is the reduced magnetization and h is the internal field. Subscripts $+(-)$ refers to temperatures above (below) T_c.

From the experimental point of view the A.C. susceptibility $\chi(h,t)$ is often a more desirable quantity than the magnetisation. Eq.1.22 predicts [14] (for $T > T_c$)

$$\begin{aligned} \chi(h,t) &= (\partial m/\partial h)_t \\ &\sim t^{-\gamma} F'\left(h/t^{\gamma+\beta}\right) \\ &= h^{-\gamma/\gamma+\beta}\left(h/t^{\gamma+\beta}\right)^{\gamma/\gamma+\beta} F'\left(h/t^{\gamma+\beta}\right) \\ &= h^{-\gamma/\gamma+\beta} G\left(h/t^{\gamma+\beta}\right) \end{aligned} \tag{1.23}$$

where the prime indicates the derivative of the function with respect to its argument and $G(x) = xF(x)$.

In the zero field case ($h = 0$), Eq.1.23 leads to

$$\chi(0,t) \propto t^{-\gamma} \tag{1.24}$$

Theoretically at the critical point $\chi(0,t)$ must diverge, though physically the divergence is limited and manifests itself as a critical peak. This peak is suppressed and shifted in an applied magnetic field. The peak position at any field H can be obtained from Eq.1.23 by requiring that

$$\left(\frac{\partial \chi}{\partial t}\right)_{t_m} = 0 \tag{1.25}$$

i.e.

$$G'\left(\frac{h}{t_m^{\gamma+\beta}}\right) = 0, \tag{1.26}$$

which means the argument of the function must be a constant. This gives

$$t_m \propto h^{1/\gamma+\beta} \tag{1.27}$$

Substituting Eq.1.27 into Eq.1.23 and using the Widom equality, we obtain

$$\chi(h,t_m) \propto h^{1/\delta-1} \tag{1.28}$$

Eq.1.23$-$1.28 are extremely useful in the experimental analysis because from a simple log $\sim$ log plot we can easily obtain the exponents β, γ and δ.

It follows from Eq.1.27 and Eq.1.28 that the field-dependent peaks in A.C. susceptibility are suppressed and also shifted to a higher temperature with increasing field. These properties though directly obtained from the unproven scaling hypothesis are confirmed by experiments as well as by the numerical calculations conducted by Roshko and Williams[13], in which they showed that the susceptibility given by the SK-like model does indeed behave in a manner similar to that predicted by the scaling-theory in the region of small m, h, and t.

1.2 Spontaneous Magnetoresistance Anisotropy

1.2.1 Physical Mechanism of Resistivity

The resistivity, ρ, of a sample is defined by

$$\mathbf{j} = \sigma \mathbf{E} \qquad\qquad \rho = \frac{1}{\sigma} \tag{1.29}$$

where $\mathbf{E}$ is the electric field, $\mathbf{j}$ is the current density, and σ is the conductivity. An expression for ρ can be obtained using a semiclassical model. In this model we treat the electrons in band n with energy $E_n(\mathbf{k})$ as a Bloch wave-packet with the velocity:

$$\mathbf{v}_n(\mathbf{k}) = \frac{1}{\hbar} \nabla_{\mathbf{k}} E_n(\mathbf{k}). \tag{1.30}$$

The electrons respond to the external field according to

$$\dot{\mathbf{k}} = -\frac{e}{\hbar}[\mathbf{E}(\mathbf{r}, t) + \frac{1}{c}\mathbf{v}_n(\mathbf{k}) \times \mathbf{H}(\mathbf{r}, t)]. \tag{1.31}$$

The contribution to the total current density due to a given band can be written as:

$$\mathbf{j}_n = -\frac{e}{4\pi^3} \int F_n(\mathbf{k}) \mathbf{v}_n(\mathbf{k}) \mathbf{dk}, \tag{1.32}$$

where $F_n(\mathbf{k})$ is the electron distribution function in the dynamical steady state.

The behavior of $F_n(\mathbf{k})$ is determined by the Boltzman Equation:

$$\left.\frac{\partial F_n(\mathbf{r},\mathbf{k},t)}{\partial t}\right|_{diff.} + \left.\frac{\partial F_n(\mathbf{r},\mathbf{k},t)}{\partial t}\right|_{field} + \left.\frac{\partial F_n(\mathbf{r},\mathbf{k},t)}{\partial t}\right|_{scatt.} = 0 \qquad (1.33)$$

By introducing the relaxation time approximation:

$$\left.\frac{\partial F_n(\mathbf{k},t)}{\partial t}\right|_{scatt.} = -\frac{[F_n(\mathbf{k}) - f^0(\mathbf{k})]}{\tau_n(\mathbf{k})} \qquad (1.34)$$

(where $f^0(\mathbf{k})$ is the equilibrium electron distribution function and $\tau_n(\mathbf{k})$ is the relaxation time), and solving the equation under the condition that only a static electric field, $\mathbf{E}$, exists and the temperature is uniform, the conductivity can be expressed as:

$$\overleftrightarrow{\sigma}_n = \frac{e^2}{4\pi^3}\int_{B.Z.} \tau_n(\mathbf{k})\mathbf{v}_n(\mathbf{k})\mathbf{v}_n(\mathbf{k})\left(-\frac{\partial f^0}{\partial E}\right)_{E=E_n(\mathbf{k})} \mathbf{dk} \qquad (1.35)$$

From the above discussion it is apparent that ρ is determined by $F_n(\mathbf{k})$, the electron distribution function, and in particular the band structure near the Fermi surface; as well as the scattering contribution characterized by $\tau(\mathbf{k})$.

When a magnetic field $\mathbf{H}$ is applied, the electrical resistivity of a metal is usually altered. This can be understood by considering that the Lorentz force will change the direction of motion of the electrons and hence acts as an effective scattering mechanism. Using the relaxation time approximation to treat such an effect Kohler[17] showed that, for a given non-magnetic metal,

the change in resistivity ρ in a field $\mathbf{H}$, can be represented by the form

$$\frac{\triangle\rho}{\rho_0} = F\left(\frac{H}{\rho_0}\right), \tag{1.36}$$

where ρ_0 is the resistivity in zero field and F is a function depending on the geometrical configuration as well as on the specific metal considered. Eq.1.36 is referred to as Kohler's rule.

A subsequent modification by Smit[22] indicated that in Kohler's rule the effective field acting on the current carriers should be the induction $\mathbf{B}$ rather than the field $\mathbf{H}$.

1.2.2 Spontaneous Resistance Anisotropy

Electrical conduction in ferromagnetic metals is inherently different from that in non-magnetic metals. In addition to the normal magnetoresistance discussed above there also exists a spontaneous resistive anisotropy(SRA) associated with the magnetization in ferromagetic metals. For a fully magnetized ferromagnetic polycrystal the resistivity can be expressed phenomenogically as[18]:

$$\rho(B,\theta) = \rho_0 + (\cos^2\theta - \frac{1}{3})\triangle\rho_A(B) + \triangle\rho(B,\theta), \tag{1.37}$$

where θ is the angle between the magnetic field and the current and ρ_0 is the resistivity at zero field; $\triangle\rho(B,\theta)$ represents the ordinary Lorentz force magnetoresistance, while $\triangle\rho_A$ is the anisotropic term. The spontaneous

magnetoresistance anisotropy is usually defined as:

$$\begin{aligned} \triangle\rho &= \triangle\rho_A(B \to 0) \\ &\simeq \rho_{\|}(B \to 0) - \rho_{\perp}(B \to 0). \end{aligned} \tag{1.38}$$

A number of different mechanisms have been proposed to explain this spontaneous anisotropy. However, there are basically two different, but complementary, approaches to this problem, which are based on the itinerant or localised model respectively.

Itinerant Model

The itinerant model, proposed by Campbell, Fert and Jaoul[19][21], is based on (1) the parallel two-current model for conduction in ferromagnetic metals proposed by Mott[20] and (2) the spin-mixing mechanism proposed by Smit.

Campell *et al.* suggested in this two-current sd-scattering model that at low temperature, conduction due to both s and d electrons can be divided into up-spin(majority) or down-spin(minority) sub-bands. These two channels conduct current independently and in parallel with relaxation times $\tau_\uparrow, \tau_\downarrow$ as shown in Fig.1.2. The total resistivity $\rho(0)$ will be given by

$$\rho(0) = \frac{\rho_\uparrow(0)\rho_\downarrow(0)}{\rho_\uparrow(0) + \rho_\downarrow(0)} \tag{1.39}$$

As the temperature increases there are two effects that must be considered. First, a thermal resistance $\rho^P(T)$ must be added for each spin direction respectivly. This scattering arises from phonons and impurities and can be characterized by different relaxation times $\tau_\uparrow, \tau_\downarrow$, in each subband. Second, electrons can be flipped by spin waves from one spin direction to another, and electron-electron scattering can take place between different spin sub-bands. These spin flip and electron-electron collision processes are characterized by $\tau_{\uparrow\downarrow}$.

In dynamic equilibrium, for each sub-band the rate of creation of momentum by accelerating electrons with charge e and mass m in an electric field $\mathbf{E}$ is balanced by the destruction of momentum by scattering within the sub-band and between sub-bands, i.e.

$$e\mathbf{E} = \frac{1}{\tau_\uparrow} m\mathbf{v}_\uparrow + \frac{1}{\tau_{\uparrow\downarrow}} m(\mathbf{v}_\uparrow - \mathbf{v}_\downarrow) \tag{1.40}$$

$$e\mathbf{E} = \frac{1}{\tau_\downarrow} m\mathbf{v}_\downarrow + \frac{1}{\tau_{\uparrow\downarrow}} m(\mathbf{v}_\downarrow - \mathbf{v}_\uparrow) \tag{1.41}$$

Since the total current density is

$$\mathbf{j}_T = \mathbf{j}_\uparrow + \mathbf{j}_\downarrow = ne\mathbf{v}_\uparrow + ne\mathbf{v}_\downarrow \tag{1.42}$$

and

$$\mathbf{j}_T = \frac{1}{\rho}\mathbf{E} \tag{1.43}$$

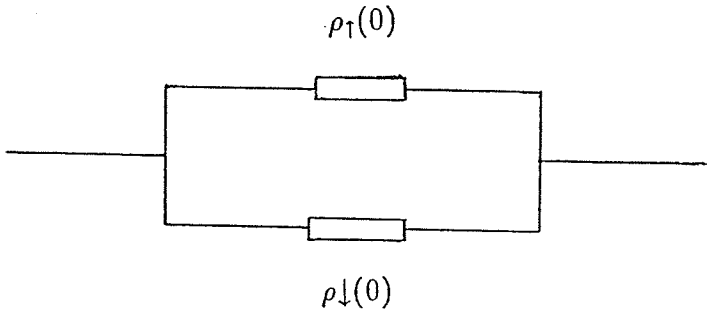

Figure 1.2: Schematical circuit for the two-current model.

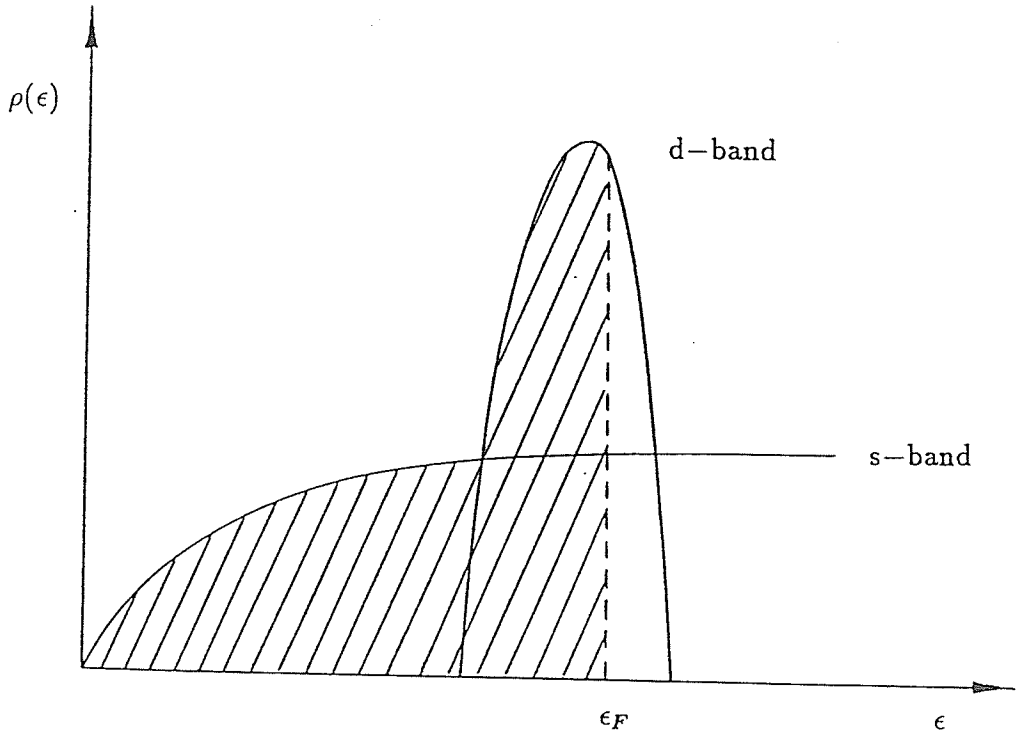

Figure 1.3: Schematic representation of the band structure of transition metals.

substituting Eq.1.40−1.42 into Eq.1.43 and using $\rho_\sigma = m/ne^2\tau_\sigma$ we obtain

$$\rho = \frac{\rho_\uparrow\rho_\downarrow + \rho_{\uparrow\downarrow}(\rho_\uparrow + \rho_\downarrow)}{\rho_\uparrow + \rho_\downarrow + 4\rho_{\uparrow\downarrow}}, \tag{1.44}$$

where $\rho_\uparrow, \rho_\downarrow$ refers to scattering within the appropriate sub-band and $\rho_{\uparrow\downarrow}$ represents the spin mixing (spin flip) contribution; the temperature dependence of each term is given by

$$\rho_\sigma = \rho_\sigma^0 + \rho_\sigma^P(T). \tag{1.45}$$

For the ferromagnetic transition metals the typical band structure is illustrated in Fig.1.3, characterized with a free-electron-like conduction s band and tight binding d band. In the absence of spin-orbit coupling the scattering is isotropic so there is no anisotropy.

Smit[22] proposed that the anisotropy can only be introduced by the interaction between the spin system and the lattice via the spin-orbit coupling. The spin-orbit interaction operator is of the form:

$$A(\mathbf{L}\cdot\mathbf{S}) = A\{L_zS_z + \frac{1}{2}(L_x - iL_y)(S_x + iS_y) + \frac{1}{2}(L_x + iL_y)(S_x - iS_y)\}$$

$$= A\{L_zS_z + \frac{1}{2}(L_+S_- + L_-S_+)\} \tag{1.46}$$

where $\hbar\mathbf{L}$ is the orbital momentum operator, S_x, S_y, S_z are the Pauli spin matrices and the magnetization is in the z-direction. The first term in this equation lifts the degeneracy of the d state of a given spin. The last term,

$\frac{1}{2}(L_+S_- + L_-S_+)$ introduces some mixing between parallel spin states and antiparallel states, which is particularly important at the Fermi surface as it permits the scattering between different spin states at that energy. The $d\uparrow - d\downarrow$ mixing is not isotropic because the magnetization direction provides a prefered axis for the spin-orbit perturbation, which is apparent from Eq.1.46 since $L_x + iL_y$ is not symetrical with respect to x, y and z. This provides a mechanism for the resistive anisotropy.

Taking the operator $A(\mathbf{L}\cdot\mathbf{S})$ as a weak perturbation, Campbell[23] *et al.* obtained

$$\rho_{sd}^{\uparrow}(k_z) = \frac{3}{2}\epsilon^2\rho' \tag{1.47}$$

$$\rho_{sd}^{\uparrow}(k_x) = \frac{3}{4}\epsilon^2\rho' \tag{1.48}$$

$$\rho_{sd}^{\downarrow}(k_z) = (1 - \frac{3}{2}\epsilon^2)\rho' \tag{1.49}$$

$$\rho_{sd}^{\downarrow}(k_x) = (1 - \frac{3}{4}\epsilon^2)\rho' \tag{1.50}$$

where ρ' is the s-d resistance for spin-up electrons in the absence of spin-orbit coupling, $\epsilon = A/H_{ex}$ where A is the spin-orbit coupling strength in the spin-down band and H_{ex} is the exchange energy which splits the $d\uparrow$ and $d\downarrow$ sub-bands.

Although the calculation is relatively simple, it predicts that the scattering for electrons travelling along the magnetization direction is stronger

than those perpendicular to it. At very low temperature

$$\frac{\triangle\rho}{\rho} = (\alpha - 1)\gamma \tag{1.51}$$

where

$$\alpha = \frac{\rho_{\uparrow}^{0}}{\rho_{\downarrow}^{0}} \qquad , \qquad \gamma = \frac{3}{4}\epsilon^{2} \tag{1.52}$$

For $T \ll T_c$, α is a constant for a given impurity.

Localized Model

The explanation for the SRA in a localized model was originally proposed by Kondo[24], who suggested that the orbital angular momentum of localized electrons is not necessarily quenched in either rare-earth metals or in iron group metals. Thus the interaction between conduction electrons and the orbital angular momenta of localized electrons must include both spin and orbital components. Consequently the scattering not only includes the usual potential V and exchange J_{ex} terms, but also the interaction between the conduction electrons and the electronic quadrupole moment(D). The total scattering term can be written as

$$V_{scatt.} = \sum_{\mathbf{k},\mathbf{k}'} \{V + J_{ex}\sigma \cdot \mathbf{J} - \frac{D}{k_F^2}[(\mathbf{J}\cdot\mathbf{k})(\mathbf{J}\cdot\mathbf{k}') - \frac{1}{3}J(J+1)\mathbf{k}\cdot\mathbf{k}']\} a_{\mathbf{k}'}^{+} a_{\mathbf{k}} \tag{1.53}$$

where $\mathbf{J}$ is the angular momentum of the magnetic (rare-earth or transition metal) ion and $a^{+}_{\mathbf{k}'}(a_{\mathbf{k}})$ is a creation(annihilation) operator of the conduction electron with wave number $\mathbf{k}$; σ is the conduction electron spin index.

The first term is the ordinary potential term, which is assumed to be isotropic (and would be in polycrystalline samples). The second term represents the exchange scattering which is temperature independent in the first Born approximation (but leads to the well known Kondo effect when the resistivity is calculated beyond the first Born approximation). In a magnetic field this term leads to a negative magnetic resistance which is isotropic if $\mathbf{J}_{ex}$ is isotropic or if a polycrystalline average is taken. The third term, however, represents the interaction with the quadrupole moment, which scatters currents parallel or perpendiculer to $\mathbf{J}$ differently. This can be seen from the Eq.1.53 since the average value of $(\mathbf{J}\cdot\mathbf{k})(\mathbf{J}\cdot\mathbf{k}')$ depends on the current direction. Using the first Born approximation and in the case of V much larger than J_{ex} or D, Friedrich and Fert[25] obtained an anisotropy of the form

$$\frac{\rho_{\parallel}(H)-\rho_{\perp}(H)}{\rho_0}=\frac{D}{V}\left[\langle J_z^2\rangle-\frac{J(J+1)}{3}\right] \tag{1.54}$$

where the magnetic field is along the z direction, ρ_0 is the resistivity at zero field and $\langle J_z^2\rangle$ is the thermal and powder average of the squared component of $\mathbf{J}$ in the field direction.

1.2.3 Discussion

The itinerant model and the localized model are two different but complementary approches used to explain the occurence of resistive anisotropy phenomena. The itinerant model naturally emphasizes the band aspects of electrons in a metal, and has been used successfully to explain the behavior of dilute transition metal based crystalline alloys. The localized model, on the other hand, places its emphasis on the contribution of the conduction electrons which interact with the fixed angular momentum **J** of localised electrons, and is most suitable for rare earth impurities in various hosts.

Reference

[1] H. Hiroyoshi and K. Fukamichi, Phys. Lett. **85A**, 242(1981).

[2] Hiroshi Yamauchi, J. Phys. Soc. Japan. **53**, 747(1984).

[3] S.N. Kaul *et al.*, J. Phys. F **16**, 365(1986).

[4] J.J. Rhyne and G.E. Fish, J. Appl. Phys. **57**, 3407(1985).

[5] D.H. Ryan *et al.*, J. Appl. Phys. **64**, 5787(1988).

[6] S. Senoussi *et al.*, J. Appl. Phys. **63**, 4086(1988).

[7] J.M.O. Coey *et al.*, Phys. Rev. B **35**, 8630(1987).

[8] D.A. Read, T. Moyo and G.C. Hallam, J. Magn. Magn. Mater. **44**, 279(1984).

[9] Yu Boliang *et al.*, J. Phys. F **13**, L127(1983).

[10] H.E. Stanley, Introduction to Phase Transitions and Critical Phenomena (Oxford 1971).

[11] S.F. Edwards and P.W. Anderson, J. Phys. F: Met. Phys. **5**, 965(1975).

[12] D. Sherrington and S.Kirkpatrick, Phys. Rew. Lett. **35**, 1793(1975).

[13] R.M. Roshko and G. Williams, J. Phys. F: Met. Phys. **14**, 703(1984).

[14] S.C. Ho, I. Maartense and G. Williams, J. Phys. F: Met. Phys. **11**, 699(1981).

[15] S.N. Kaul, J. Phys. F: Met. Phys. **18**, 2089(1988).

[16] G. Sobotta, J. Mag. Mag. Mat. **49**, 77(1985).

[17] J.M. Ziman, Electron and Phonons (Oxford 1960).

[18] O. Jaoul, I.A. Campbell and A. Fert, J. Magn. Magn. Mater. **5**, 23(1977).

[19] I.A. Campbell et al. , Phil. Mag. **15**, 977(1967).

[20] N.F. Mott, Proc. Roy. Soc.(London) Ser. A **153**, 699(1936).

[21] A. Fert and I.A. Campbell, Phys. Rev. Lett. **121**, 1190(1968).

[22] J. Smit, Physica **17**, 612(1951).

[23] I.A. Campbell et al. , J. Phys. C: Suppl.1, S95(1970).

[24] J. Kondo, Prog. Theor. Phys. **27**, 772(1962).

[26] A. Friederich, A. Fert, Phys. Rew. Lett. **33**, 1214(1974).

[27] S.C. Ho, I Maartense and G. Williams, J. Phys. F: Met. Phys. **11**, 1107(1981). [28] P. Gaunt, S.C. Ho, G. Williams and R.W. Cochrane, Phys. Rev. B **23**, 489(1981)

Chapter 2

Experimental Methods

2.1 Measurement of A.C. Susceptibility

The A.C. susceptibility was measured using a system which consists of two essential parts:

1. The cryostat and sample insert system.
2. The phase-locked magnetometer.

2.1.1 The Cryostat and Insert System

This system is designed to enable temperatures in the range $1.4K$ to $320K$ to be obtained. As shown in Fig.2.1 the cryostat system consists of two concentric glass dewars, an outer liquid nitrogen dewar and an inner dewar. The outer nitrogen dewar serves two purposes; (1) It allows the biasing coils and the sensing coils of the susceptometer to be immersed in liquid N_2, thus cooling them (reducing their resistance and thus improving the Q-factor of the detection circuit) while also maintaining them at a stable temperature. (2) It provides additional thermal isolation for the liquid helium contained in the inner dewar. The degree of thermal contact between the inside of the helium dewar and the outer liquid N_2 jacket can be controlled by varying the pressure in the vacuum space of the inner dewar.

The sample, as well as the thermocouple and germanium resistance thermometer used for temperature measurement, are embedded in a long bundle of thin copper wires (33 gauge), which is anchored to the bottom of the copper block with soft solder ensuring good thermal contact. About 10 turns of nichrome wire (30 gauge, 13.2 Ω/ft, with total resistance of 50Ω at

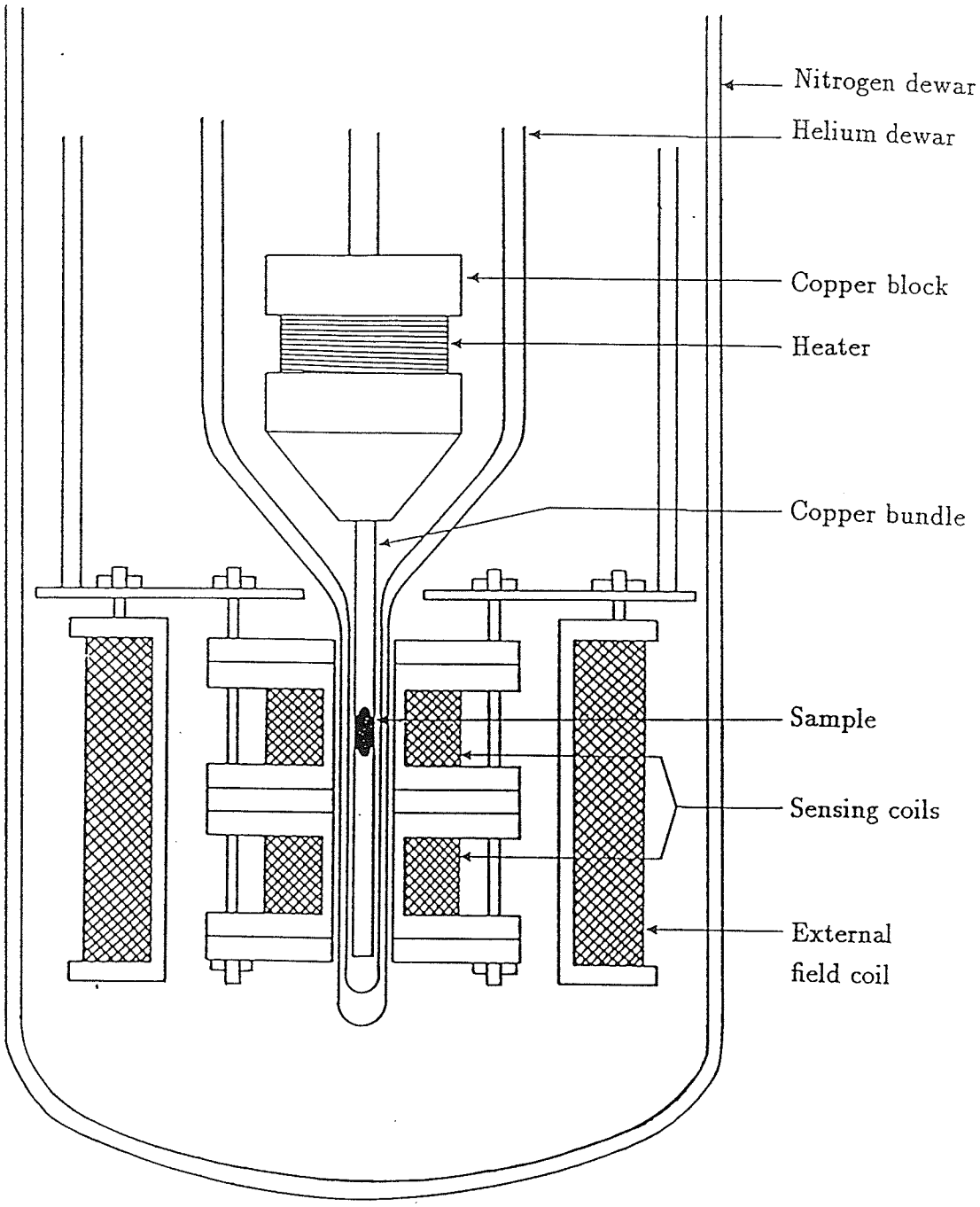

Figure 2.1: Arrangement of the sensing coils, D.C. biasing-field coils and the sample probe in the A.C. susceptibility cryostat system.

room temperature) wound around the copper block was used as a heater. The bundle of copper wires provide the necessary thermal contact between the heater and the sample, and also allows the A.C. field of the sensing coil to penetrate.

When measurements below $4.2K$ are necessary, the temperature is accurately controlled by adjusting the helium vapour pressure inside the inner dewar using a high capacity mechanical pump connected through a parallel combination of large and small valves; while for measurements above $4.2K$, which is usually the situation in our experiments, the temperature is controlled by a balance of the heat provided by the heater and the radiation to or from the liquid N_2 in the outer dewar.

2.1.2 Phase - Locked Magnetometer

The A.C. susceptibility of the sample was measured using a phase-locked magnetometer[1], which basically compares the resonant frequencies of two LC circuits. A block diagram is shown in Fig.2.2. Two sensing coils, $L1$ and $L2$, are arranged in two different resonant LC circuits, which are initially tuned to have the same natural resonant frequency, so that

$$\omega_1 = \frac{1}{\sqrt{L_1 C_1}} \qquad \omega_2 = \frac{1}{\sqrt{L_2 C_2}}$$

with $\omega_1 = \omega_2$.

Initially both resonant circuits are driven at frequency ω_1, also referred to as the driving field frequency. When a magnetic sample is inserted into the

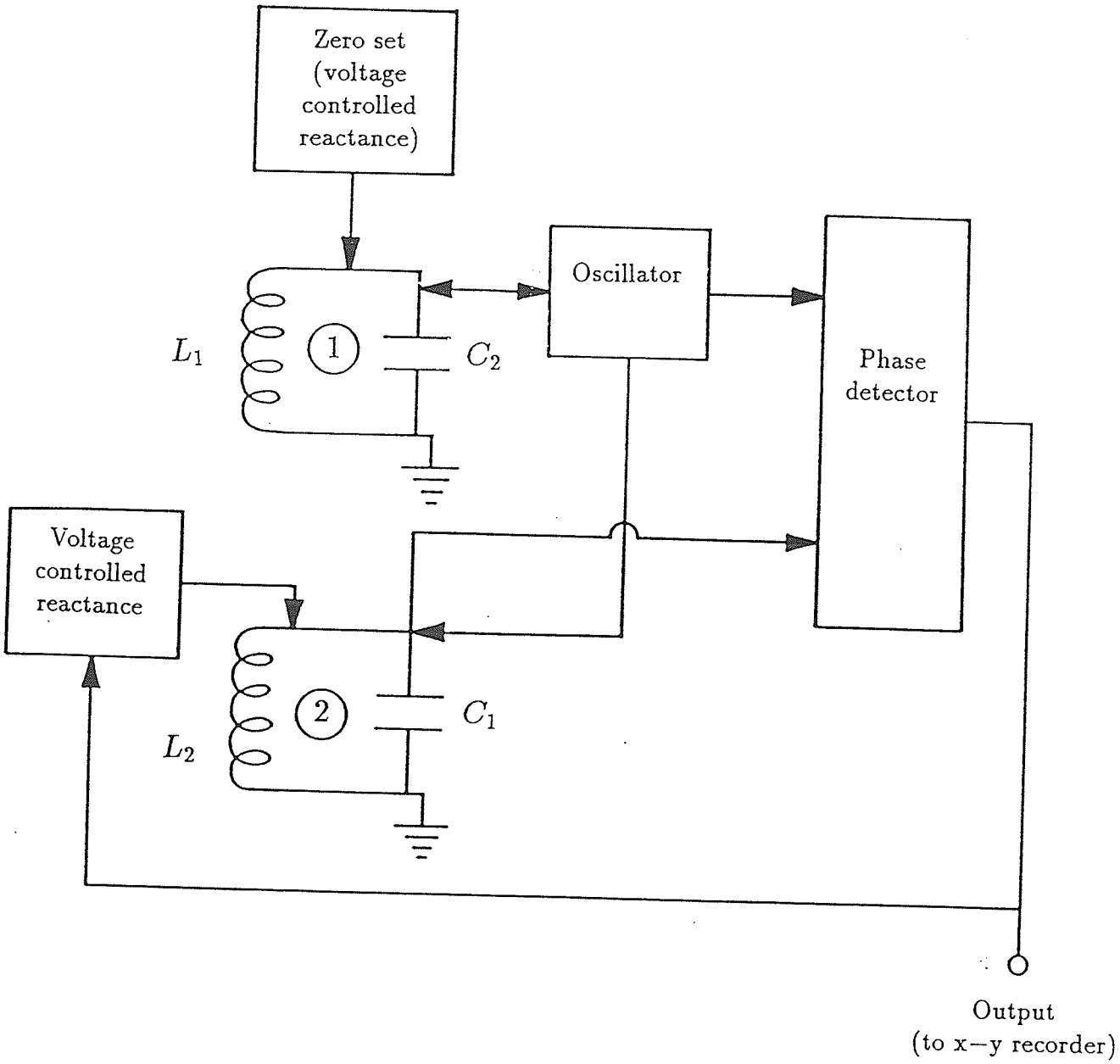

Figure 2.2: Block diagram of phase-locked magnetometer

second coil, the inductance L_2, and hence ω_2 changes. These two different frequencies are compared in a phase detector which generates a correction voltage to restore the frequency ω_2 to its initial value through a voltage-controlled reactance in that circuit[1]. This correction voltage is proportional to the change in L_2 and hence proportional to the A.C. susceptibility of the sample. The susceptometer output, in volts, is then converted to true susceptibility using a calibration factor determined by measuring the signal produced by a Gd_2O_3 calibration sample, as described below.

2.1.3 Calibration

The measured susceptibility, χ, is related to the change in the inductance, $\triangle L$, of the sensing coil by the equation[1]

$$\chi = \frac{\triangle L}{4\pi L \eta}, \tag{2.1}$$

where η is the filling factor of the sample in the coil. Since η is not easily determined, the magnetometer is usually calibrated by measuring the signal produced by Gd_2O_3 powder at $77K$.

Gd_2O_3 is a paramagnet at $77K$, with a susceptibility described by the Curie law:

$$\chi = \frac{dM}{dH_i} = \frac{Ng^2\mu_B^2 J(J+1)}{3K_B T}, \tag{2.2}$$

where H_i is the internal field. For Gd_2O_3

$$g = 2$$

$$J_{Gd} = S_{Gd} = 3.5$$

Substituting these parameters into Eq.2.2 , we obtain

$$\chi = 5.613 \times 10^{-4} emu/O_e - g \tag{2.3}$$

By measuring the output signal of the Gd_2O_3 sample in volts (χ_v) and its mass(m), the calibration factor can be obtained from the following equation:

$$\chi_m m = c\chi_v \tag{2.4}$$

where χ_m is the measured susceptibility in emu/O_e−g, and c is the calibration factor. It was found that

$$c = (8.85 \pm 0.15) \times 10^{-4} emu/O_e - V$$

2.2 Measurement of Magnetoresistance

The system consists of the following components:

(1) The cryostat assembly, which is similar to that of the A.C. susceptibility apparatus described previously.

(2) The A.C. resistivity measurement system.

(3) A rotatable electro-magnet, which provides a magnetic field in the range from $0\,G$ to $10KG$ parallel or perpendicular to the samples.

2.2.1 Sample Insert

The sample insert shown in Fig.2.3, consists of a high thermal conductivity copper block (of approximate dimensions $7.0 \times 3.5 \times 0.4$ cm) soldered to the end of a long thin-wall stainless steel tube which also contains the current and voltage leads for the six samples mounted on the block. The samples are mounted on copper knife-edge voltage contacts which are electrically insulated from but thermally connected to the copper block using paper insulators bonded with GE varnish.

The current and voltage lead connections are shown in Fig.2.4. The leads are routed to a "switch-board" box from which the appropriate leads can be connected to the external measuring circuits.

2.2.2 A.C. Resistivity Measurement Circuit

The accurate measurement of the resistance is achieved with a Princeton Applied Research (PAR) HR8 precision lock-in amplifier used as a null-detector

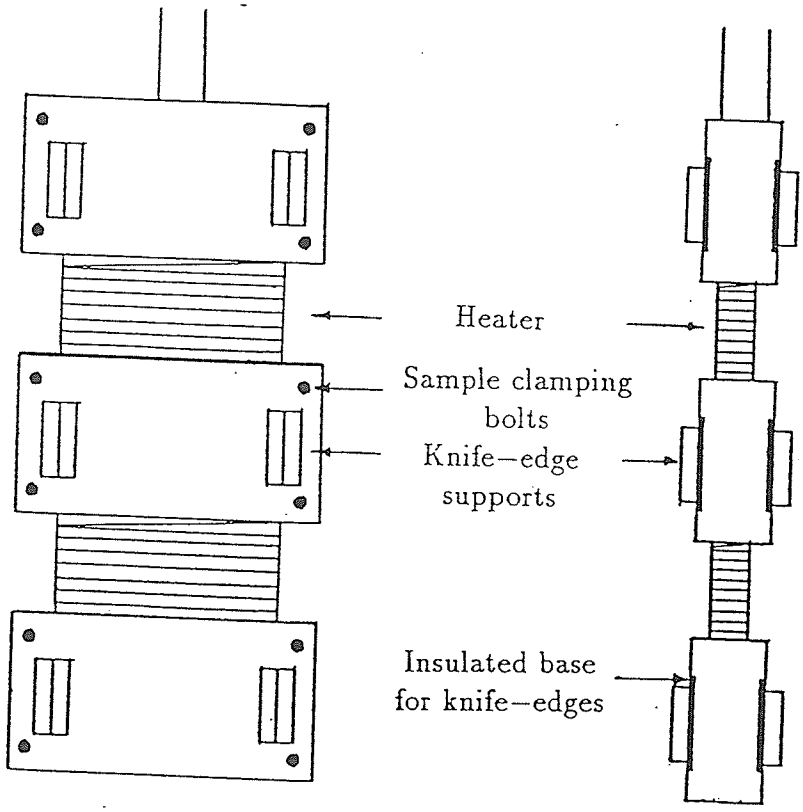

Figure 2.3: (a) Front-view of the sample block. (b) Edge-view of the sample block.

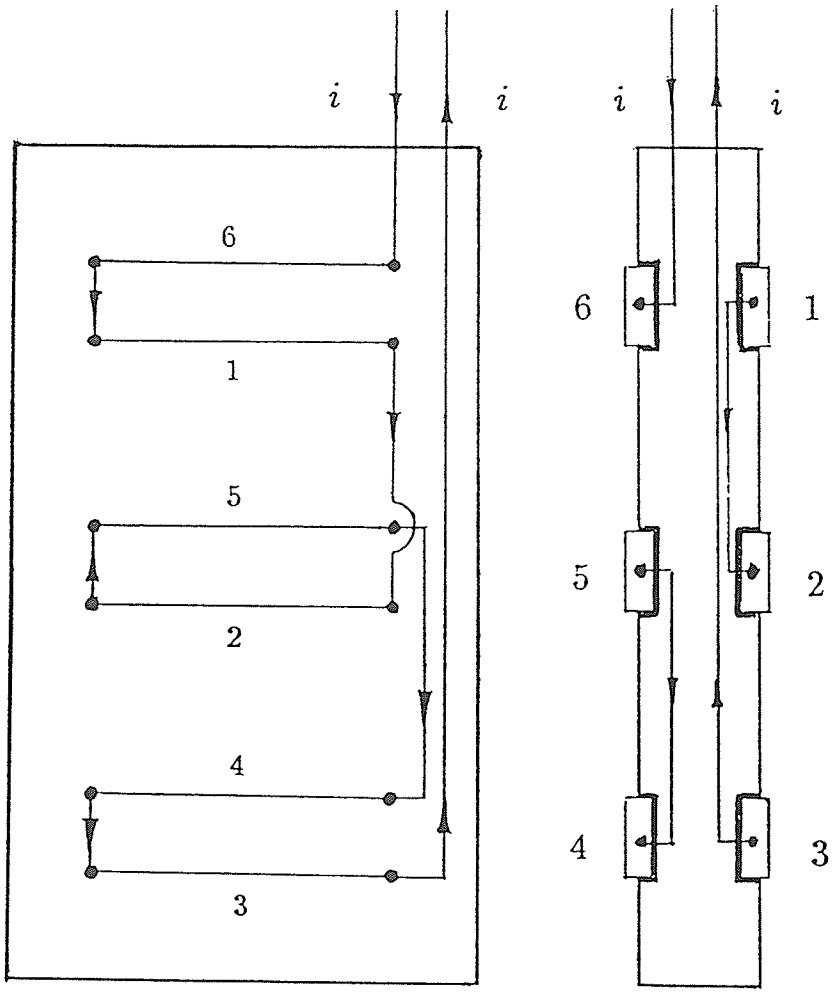

Figure 2.4: Current lead connections

in an A.C. back-off circuit. The principal advantage of an A.C. technique incorporating phase-sensitive detection is that it is not sensitive to the effects of spurious thermal emf's, thus making the observation of small signal changes possible.

The circuit used is shown in Fig.2.5 and Fig.2.6. Fig.2.5 illustrates the basic principle of the back-off system originally used by Muir and Ström-Olsen[2]. The voltage across the Kelvin-Varley DP1211 potentiometer, R_0, in the back-off system can be initially adjusted to null the sample voltage. During the measurement the resistance of the sample will change with the applied magnetic field and/or temperature. This signal i.e. the voltage difference between the sample and R_0 will then be sent to the lock-in amplifer. Since the current through the sample and back-off system is the same, the effects of fluctuations in the current are cancelled to first order at the input of the lock-in amplifer.

The PAR HR8 lock-in amplifer is essentially a detector which achieves a large signal-to-noise ratio by using a narrow band pass filter tuned to the operating frequency. In the measurement we chose an operating frequency of 37Hz in order to avoid any interference from the line as well as to minimize the high frequency skin-depth effects. The output signal from the lock-in amplifer can then be sent to either an X-Y recorder for a permanent record of the variation of the sample resistance with field or temperature, or to a DVM for data collection.

The system is capable of detecting a resistance change on the order of

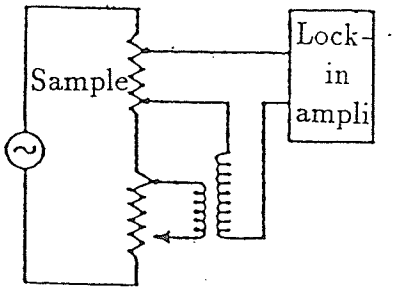

Figure 2.5: The basic circuit of the back-off system.

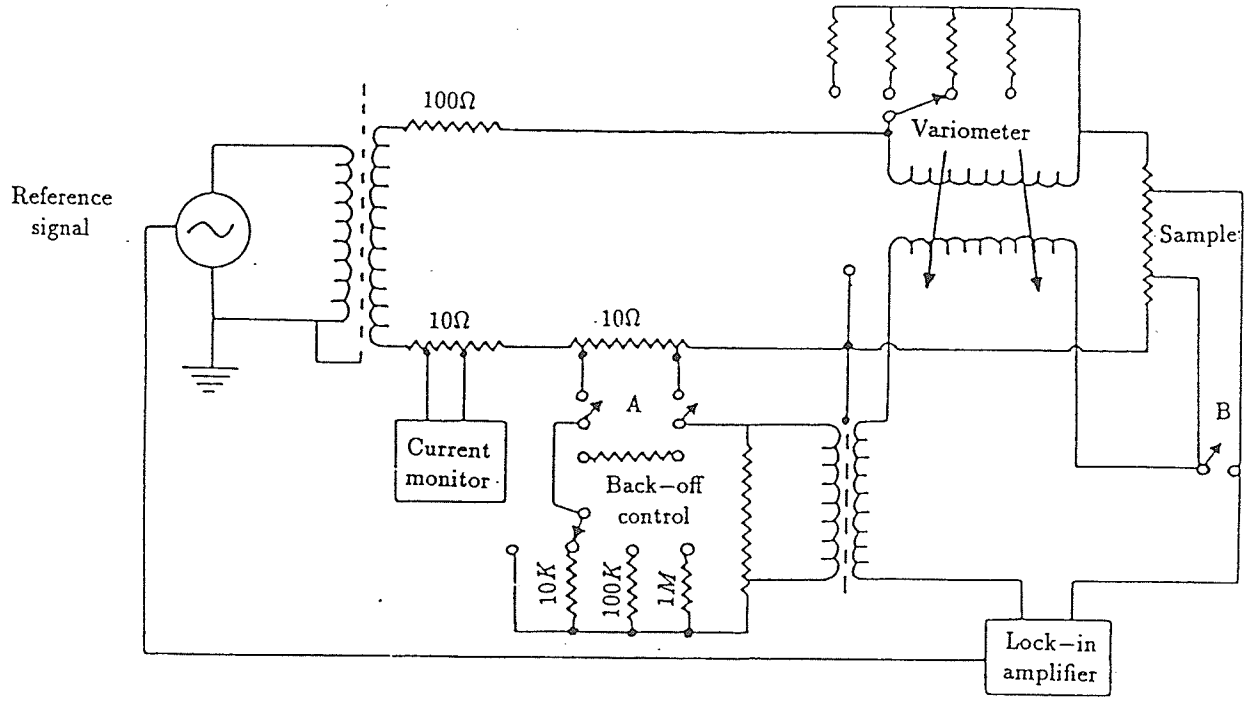

Figure 2.6: Detailed circuit diagram of the back-off system used for magnetoresistance measurements.

one part in 10^6; however, when the sample signal is very large, which is the case for the highly resistive FeZr amorphous samples we have studied, the A.C. back-off circuit proved to be inadequate and in this situation we found it was possible to achieve adequate resolution using the internal d.c. back-off circuit of the HR8 in conjunction with either an X-Y recorder operating with relatively high Y(vertical) sensitivity, or a DVM for data collection.

Reference

[1] I. Maartense, Rev. Sci. Inst. **41**, 657(1970).

[2]W.B. Muir and J.O. Ström-Olsen, J. of Phys. E: Sci. Inst. **9**, 163(1976).

Chapter 3

Data Analysis and Discussion

3.1 A.C. Susceptibility

3.1.1 Correction of the Data

There are two principal corrections that need to be applied to the measured A.C. susceptibility. The first of these is the background correction; the background signal should in fact be cancelled out because of the two counter-wound sensing coils comprising the phase-locked system; in practice, however, it is non-zero and negative (i.e. a diamagnetic signal). The main reason for this background signal are the small differences in the construction of the two sensing coils and non-uniformities in the bundle of copper wires used to suspend the sample. For the $FeZr$ susceptibility measurements this correction is most important at low temperatures $(4.2K - 70K)$, since here the background signal is comparable with that of the sample. The correction can be easily achieved by substracting the measured background signal obtained with the sample removed.

The second important correction is that for the internal field. The susceptibility determined by the susceptometer is

$$\chi_m = \frac{dM}{dH_a}, \tag{3.1}$$

where H_a is the externally applied driving field, while the true susceptibility is

$$\chi_t = \frac{dM}{dH_i}, \tag{3.2}$$

where H_i is the corresponding internal field. The relationship between H_a and H_i is usually written as

$$H_i = H_a - NM, \tag{3.3}$$

where M is the magnetization induced in the sample and N is the demagnetising factor. In the present analysis we assume that the sample is uniformly magnetized, which is a reasonable assumption since the sample is rounded into an ellipsoidal shape as discussed in the following section. Eqs.3.1–3.3 then lead to

$$\chi_i = \frac{\chi_m}{1 - N\chi_m}. \tag{3.4}$$

The demagnetising factor N is calculated by treating the sample as an ellipsoid with principal axes equal to the dimensions of the sample and evaluating the corresponding elliptic integral [1]. The above equation also suggests that the maximum value of the measured susceptibility (corrected for background) is limited by the requirement that

$$1 - N\chi_m = 0 \tag{3.5}$$

i.e.

$$\chi_m \leq \frac{1}{N} \tag{3.6}$$

In order to use Eq.3.3 to determine H_i (the internal field which is used in a variety of plots, such as Fig. 3.2–Fig. 3.16), it is necessary to estimate the

magnetization M; this is done at each temperature T_0 using the following expression:

$$M(T_0) = \int_0^{H_i} \chi_t(T_0) dH_i \tag{3.7}$$

where χ_t is the corrected susceptibility at T_0. The integal is estimated numerically using the trapezoidal rule in conjunction with the measured field-dependent susceptibility.

3.1.2 Sample Preparation

As pointed out above, the true susceptibility can only be obtained after we have taken the demagnetizing factor, hence the shape of the sample, into consideration. In order to minimize any error introduced in the estimation of N, we use a sample which is as long and narrow as possible (limited by the dimensions of the pick-up coils and their separation), cut so that the ratio of the length (l_i) to width (w_i) of each piece is a constant, i.e.

$$\frac{l_i}{w_i} = constant. \tag{3.8}$$

This means every piece has approximatly the same demagnetizing factor, since the elliptic integrals actually depend only on the ratio of the principal axes of the sample[1].

To increase the measured signal several pieces may be stacked together, as long as they are separated by an insulating layer. The typical dimensions of the samples used in the present study are about $(1.6 \times 0.1 \times 0.002)$ cm,

yielding a demagnetizing factor $N \simeq 0.003$, when the field is applied along the longest dimension.

3.1.3 Results

As we have discussed in Chapter One, the critical point exponents can be obtained from the following scaling equations:

$$\chi(h, t_m) \propto h^{1/\delta - 1}, \tag{3.9}$$

$$\chi(0, t) \propto t^{-\gamma}. \tag{3.10}$$

$$t_m \propto h^{1/(\gamma+\beta)}, \tag{3.11}$$

This last equation can also be written as:

$$T_m - T_c \propto H_i^{1/\gamma+\beta}, \tag{3.12}$$

in which T_m is the corresponding temperature of the susceptibility maximum in field H_i. In each of these equations an important parameter is T_c, which needs to be chosen carefully. The method we used is as follows.

According to Eq.3.12, the plot of T_m against $H_i^{1/(\gamma+\beta)}$ should extrapolate to T_c at $H_i = 0$. With a typical value of $1/(\gamma + \beta) \cong 0.5$, T_c can be obtained from a plot of T_m against $H_i^{0.5}$. This initial estimate for T_c can then be used in conjunction with Eq. 3.11 to produce a $\log(t_m)$ vs. $\log(H_i)$ plot, the slope of which determines $\gamma + \beta$. If this value is consistent with

what was initially assumed, i.e. $1/(\gamma+\beta) \cong 0.5$, we will accept this T_c as a correct value, along with the $\gamma+\beta$; if not, the process must be repeated with a small adjustment in T_c (typically within one percent of T_c). This technique is outlined in Fig. 3.1 to Fig. 3.8. The δ value is more easily obtained using Eq. 3.9, and shown in Fig. 3.9−Fig. 3.12, since it is independent of the choice of T_c.

Values deduced in this way for T_c, δ and $\gamma+\beta$ are shown in table 3.1 for a series of alloys in the $FeZr$ system.

With a value for T_c, it is usual to attempt to find γ by plotting the zero-field susceptibility against the reduced temperature on a double logarithmic scale (shown in Fig. 3.13−3.16), the slope of which is γ. For amorphous materials, the Kouvel−Fisher exponent is usually used as an effective exponent $\gamma^*(T)$, which is defined as

$$\gamma^*(T) = (T - T_c)\chi d\chi^{-1}/dT. \tag{3.13}$$

We found that $\gamma^*(T)$ initially increases with increasing temperatures just above T_c, then decreases at higher temperatures, as shown in Fig. 3.17. An explanation and discussion for this phenomenon will be presented in the final section of this chapter.

Table 3.1: Experimental values for $Fe_{100-x}Zr_x$ samples.

	T_c	δ	$1/(\gamma+\beta)$
$Fe_{92}Zr_8$	181.0	4.59	0.488
$Fe_{91}Zr_9$	199.4	4.56	0.498
$Fe_{90}Zr_{10}$	236.8	4.14	0.505
$Fe_{89}Zr_{11}$	246.2	4.14	0.497

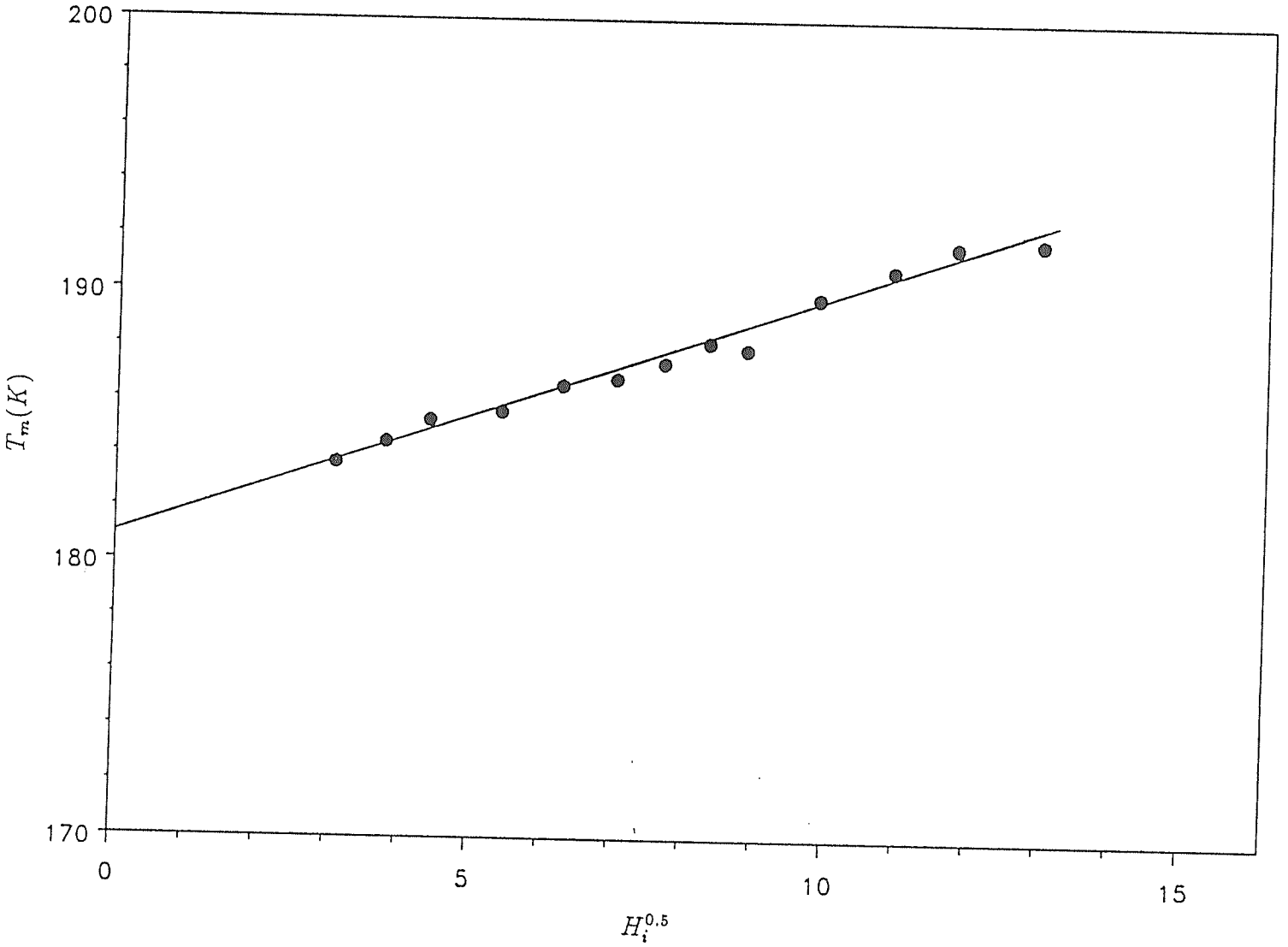

Figure 3.1: T_m vs. $H_i^{0.5}$ for $Fe_{92}Zr_8$.

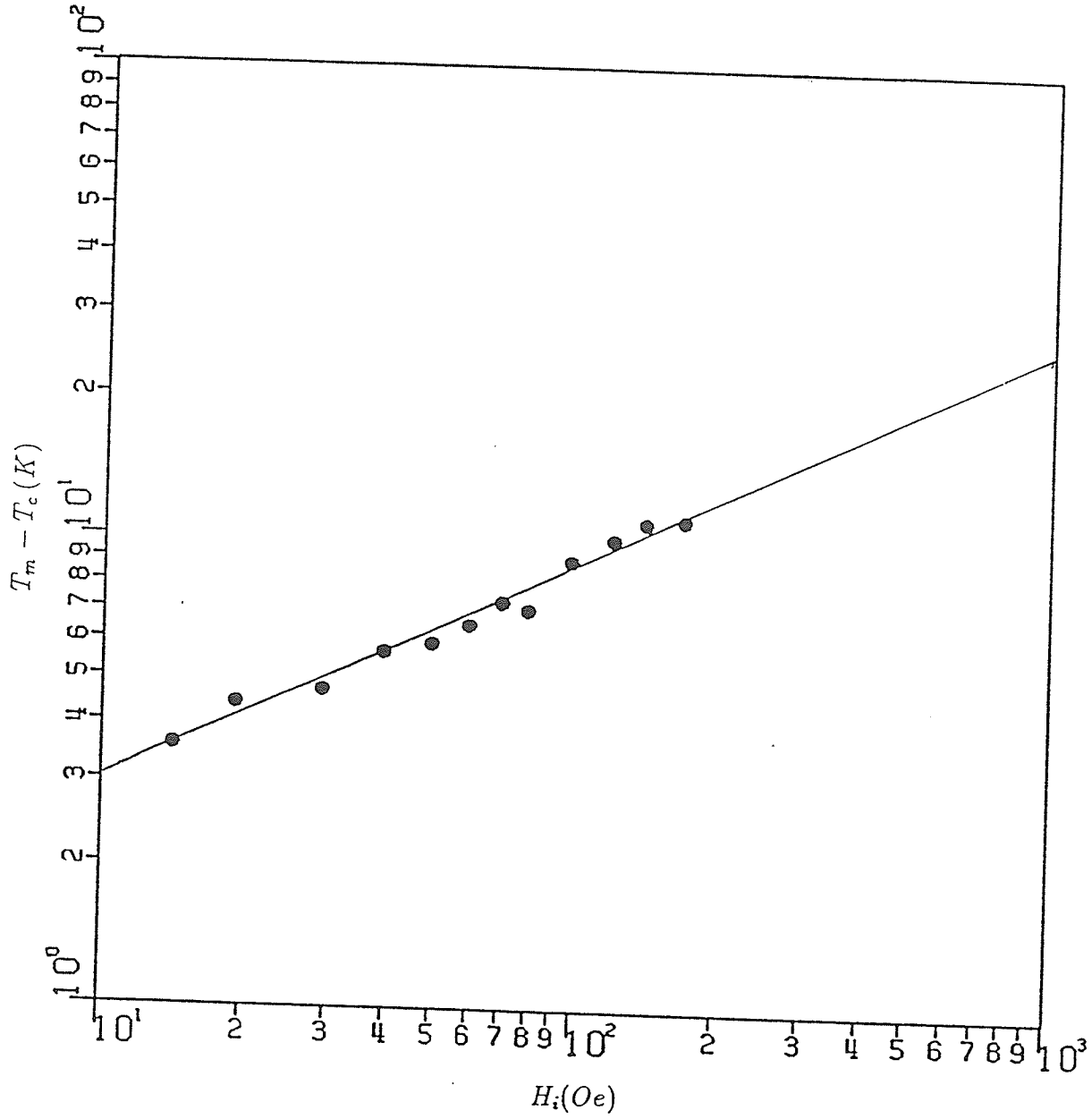

Figure 3.2: $T_m - T_c$ vs. H_i for $Fe_{92}Zr_8$ ($\gamma + \beta$ plot).

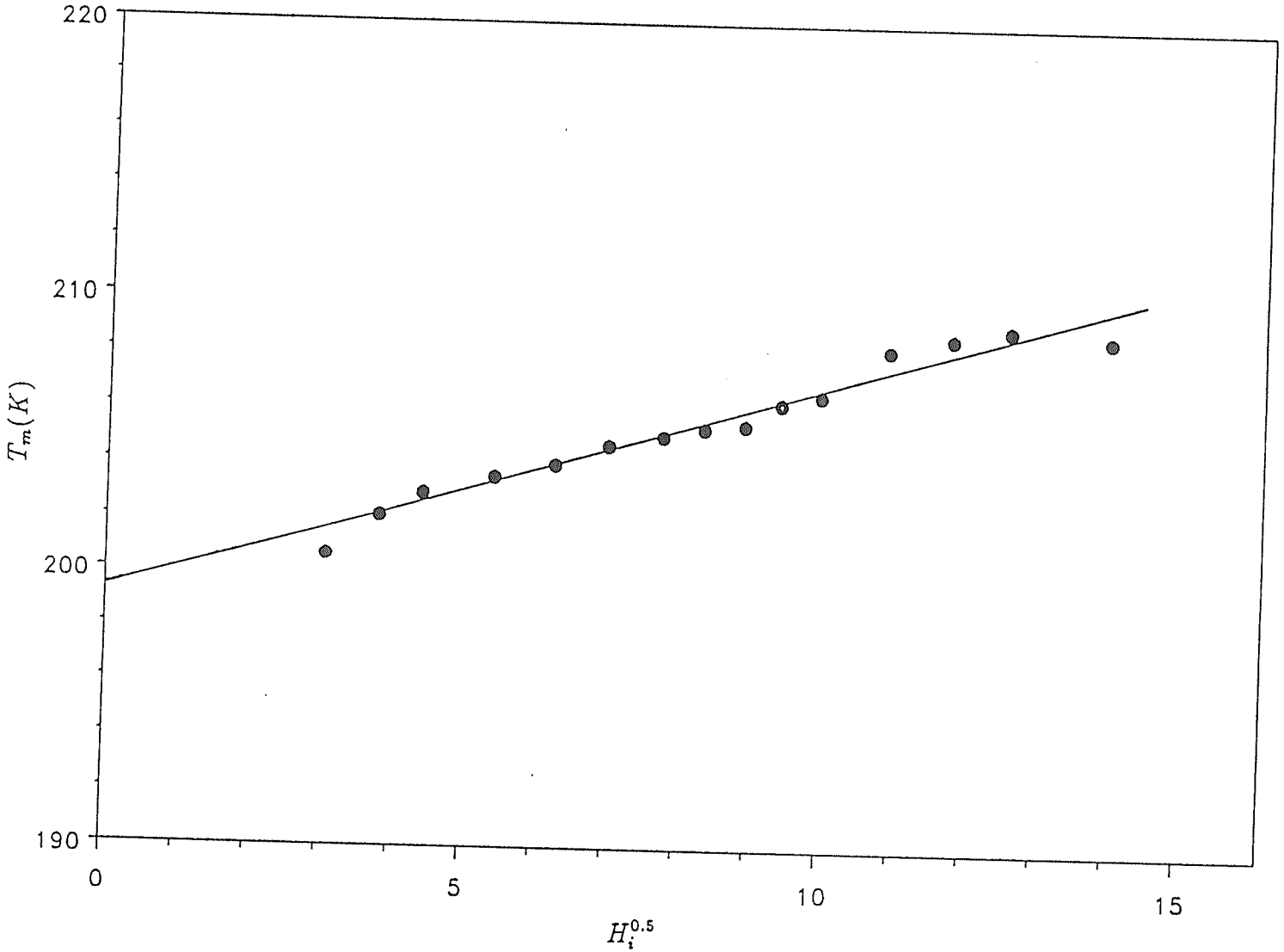

Figure 3.3: T_m vs. $H_i^{0.5}$ for $Fe_{91}Zr_9$.

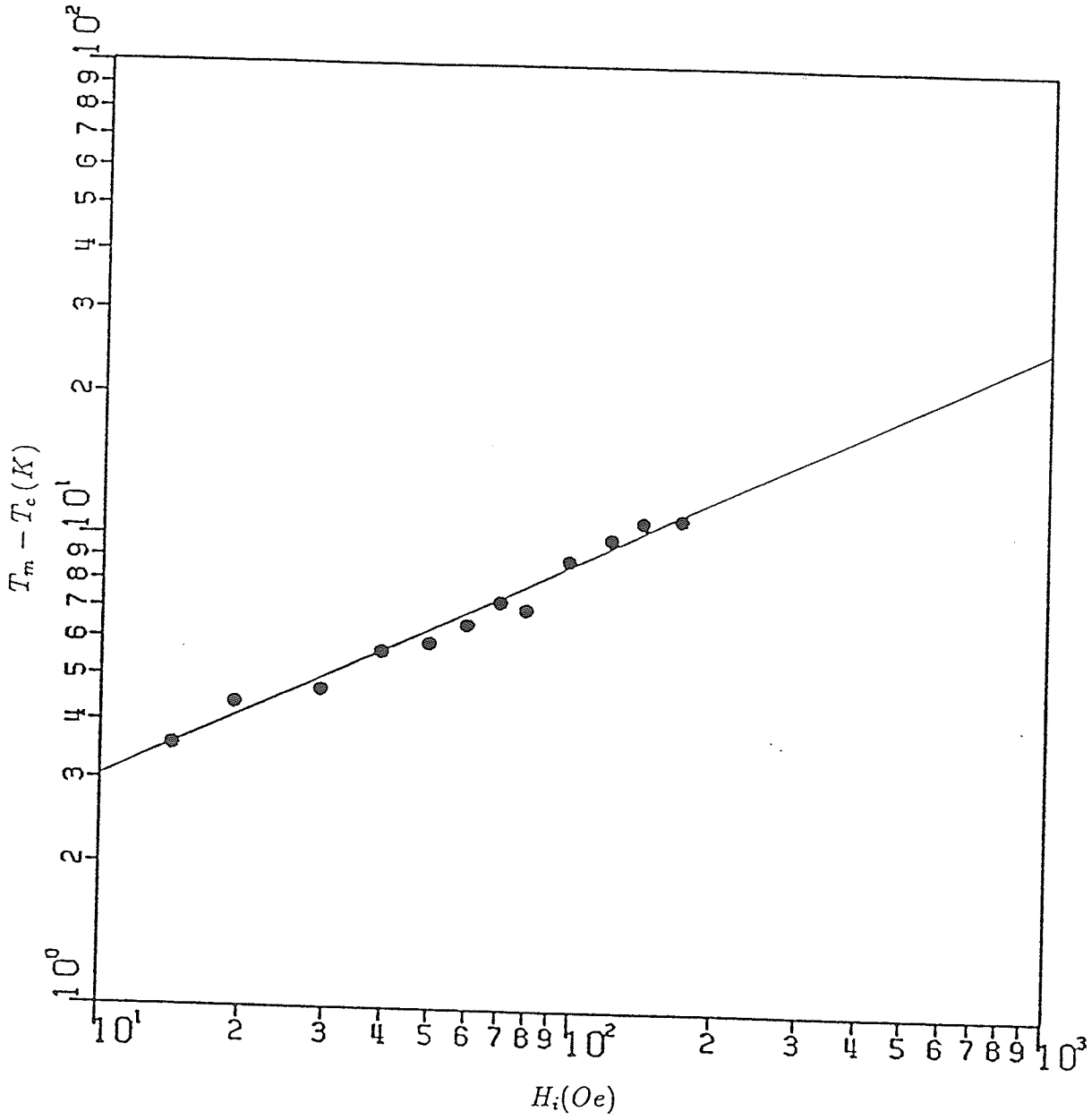

Figure 3.4: $T_m - T_c$ vs. H_i for $Fe_{91}Zr_9$ ($\gamma + \beta$ plot).

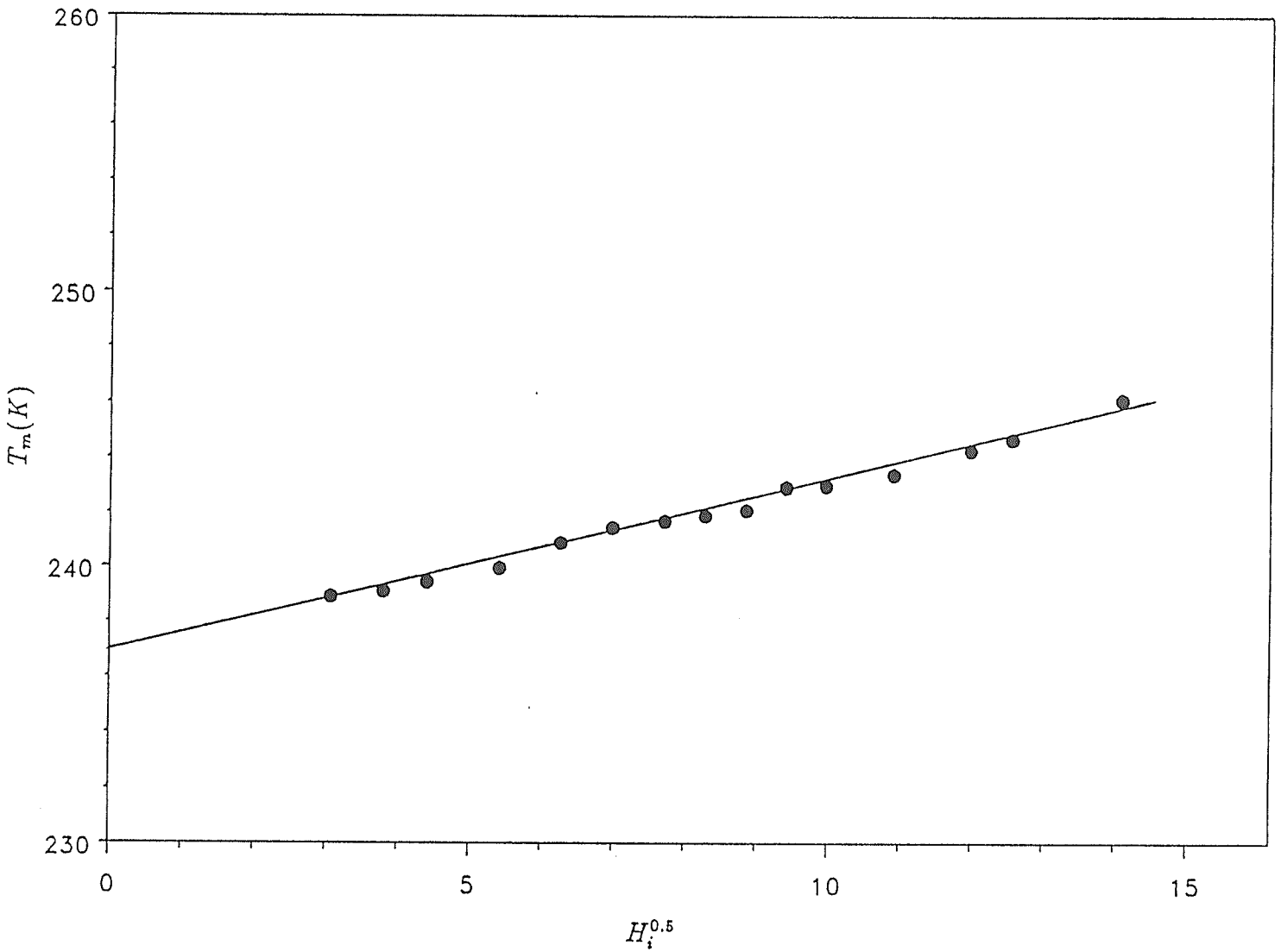

Figure 3.5: T_m vs. $H_i^{0.5}$ for $Fe_{90}Zr_{10}$.

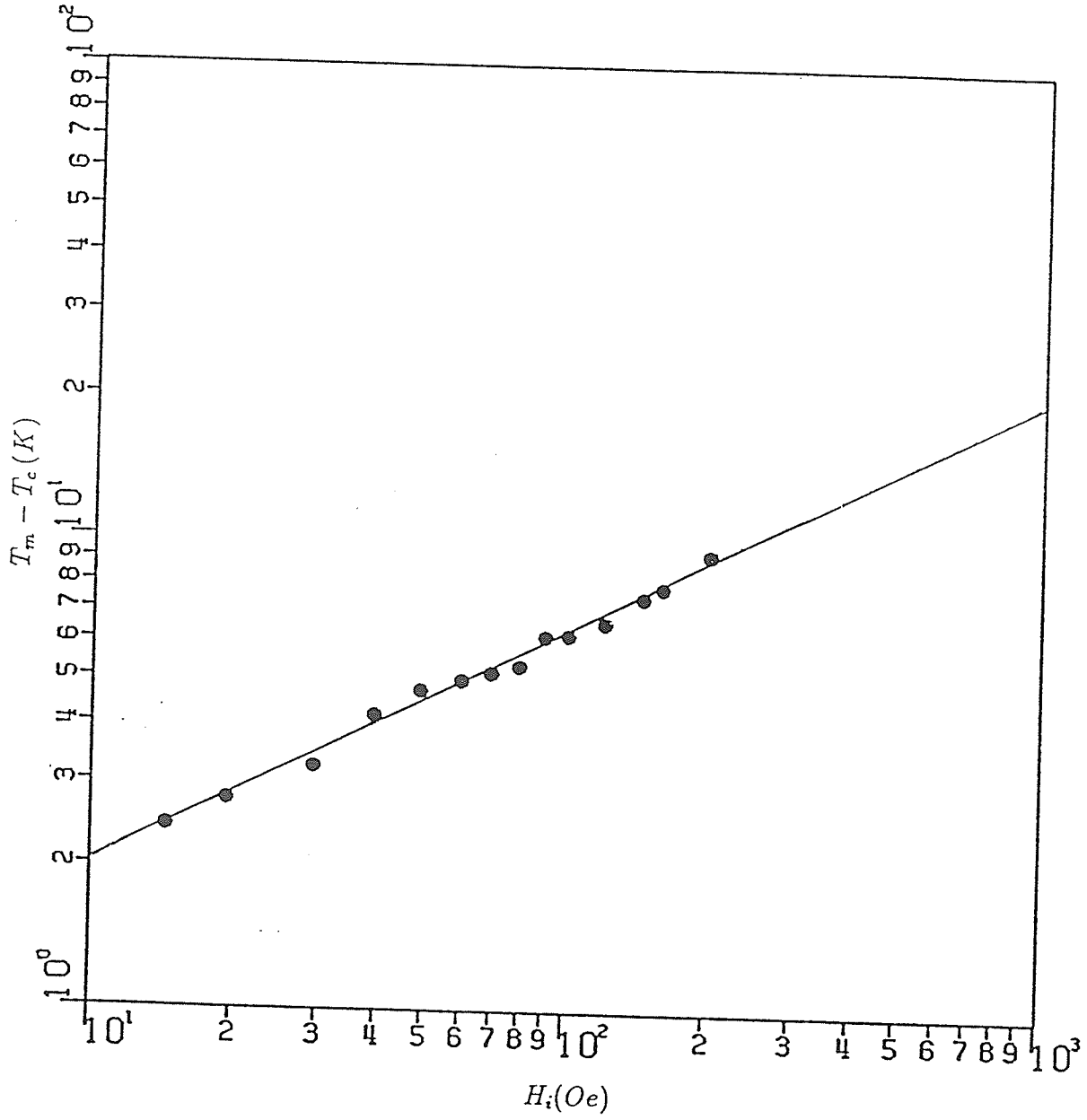

Figure 3.6: $T_m - T_c$ vs. H_i for $Fe_{90}Zr_{10}$ ($\gamma + \beta$ plot).

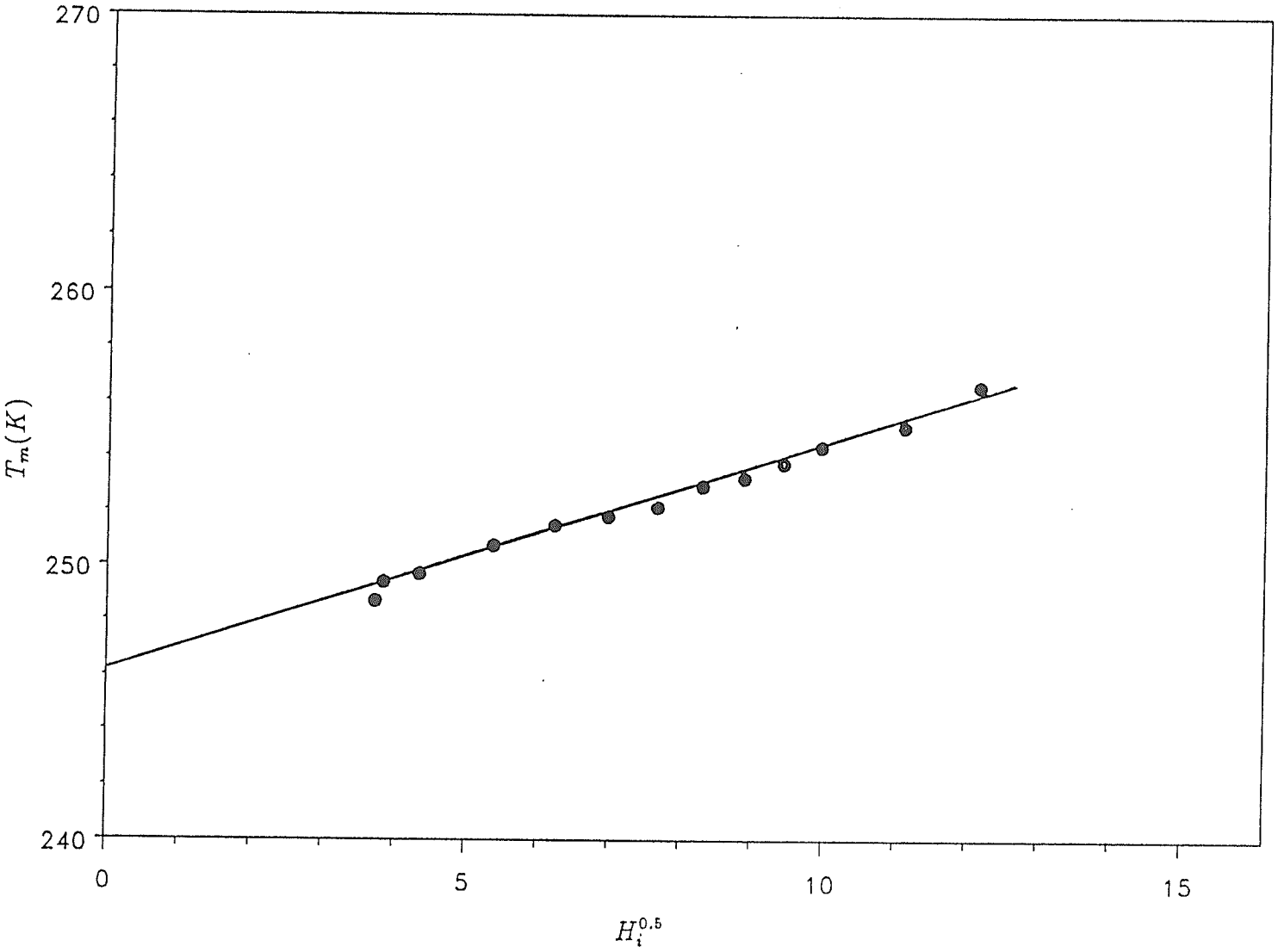

Figure 3.7: T_m vs. $H_i^{0.5}$ for $Fe_{89}Zr_{11}$.

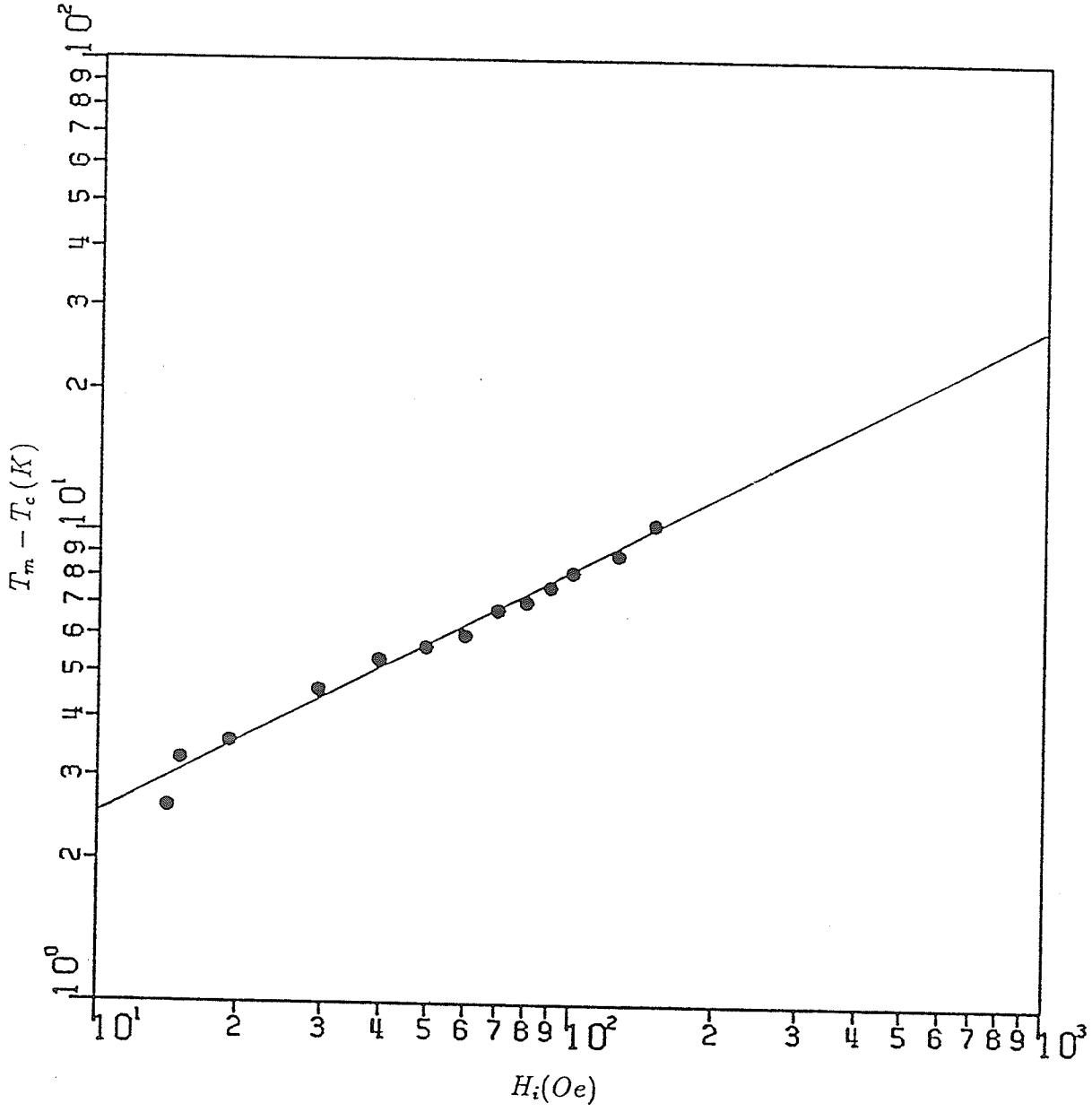

Figure 3.8: $T_m - T_c$ vs. H_i for $Fe_{89}Zr_{11}$ ($\gamma + \beta$ plot).

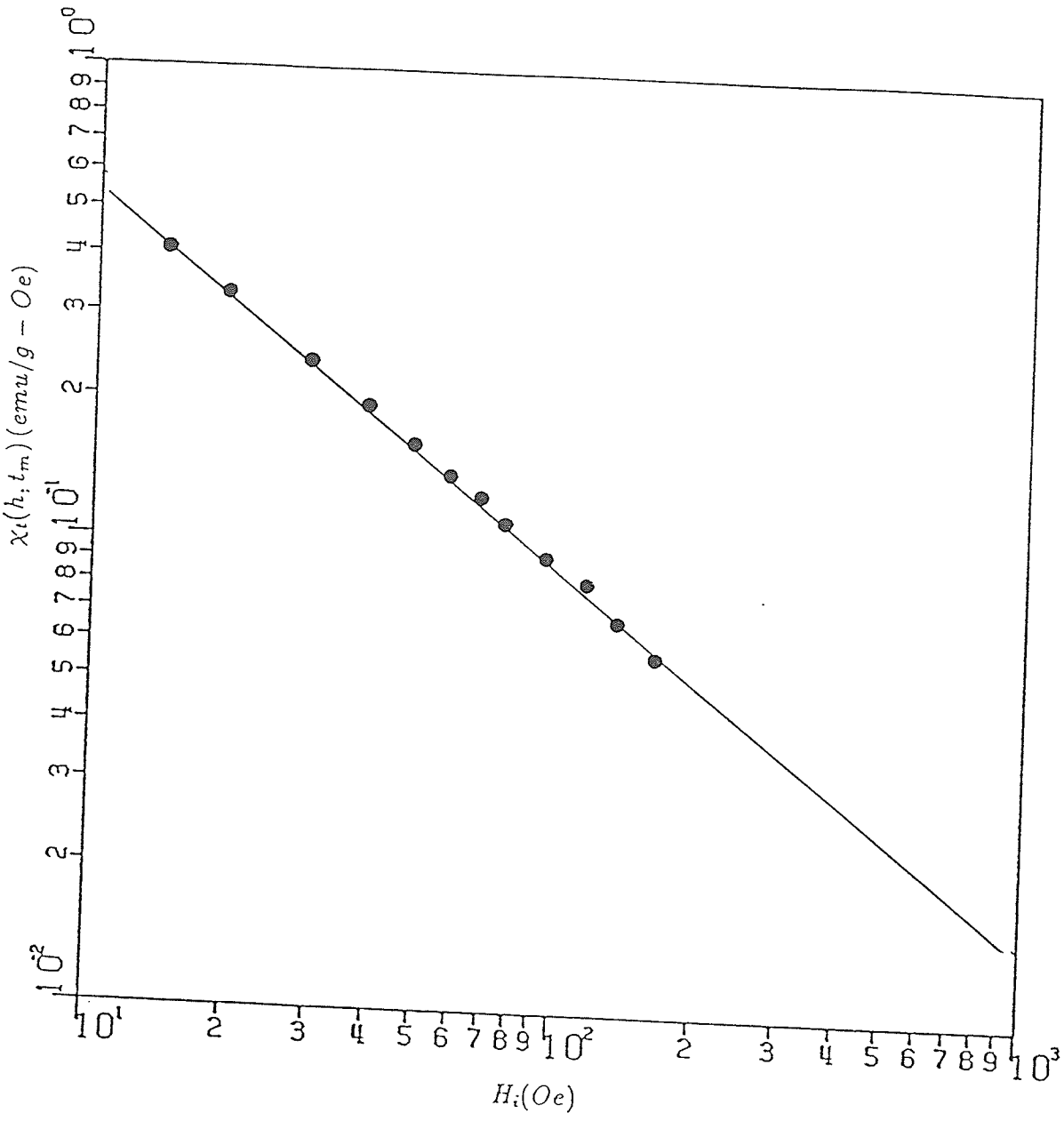

Figure 3.9: $\chi_t(h, t_m)$ vs. H_i for $Fe_{92}Zr_8$ (δ plot).

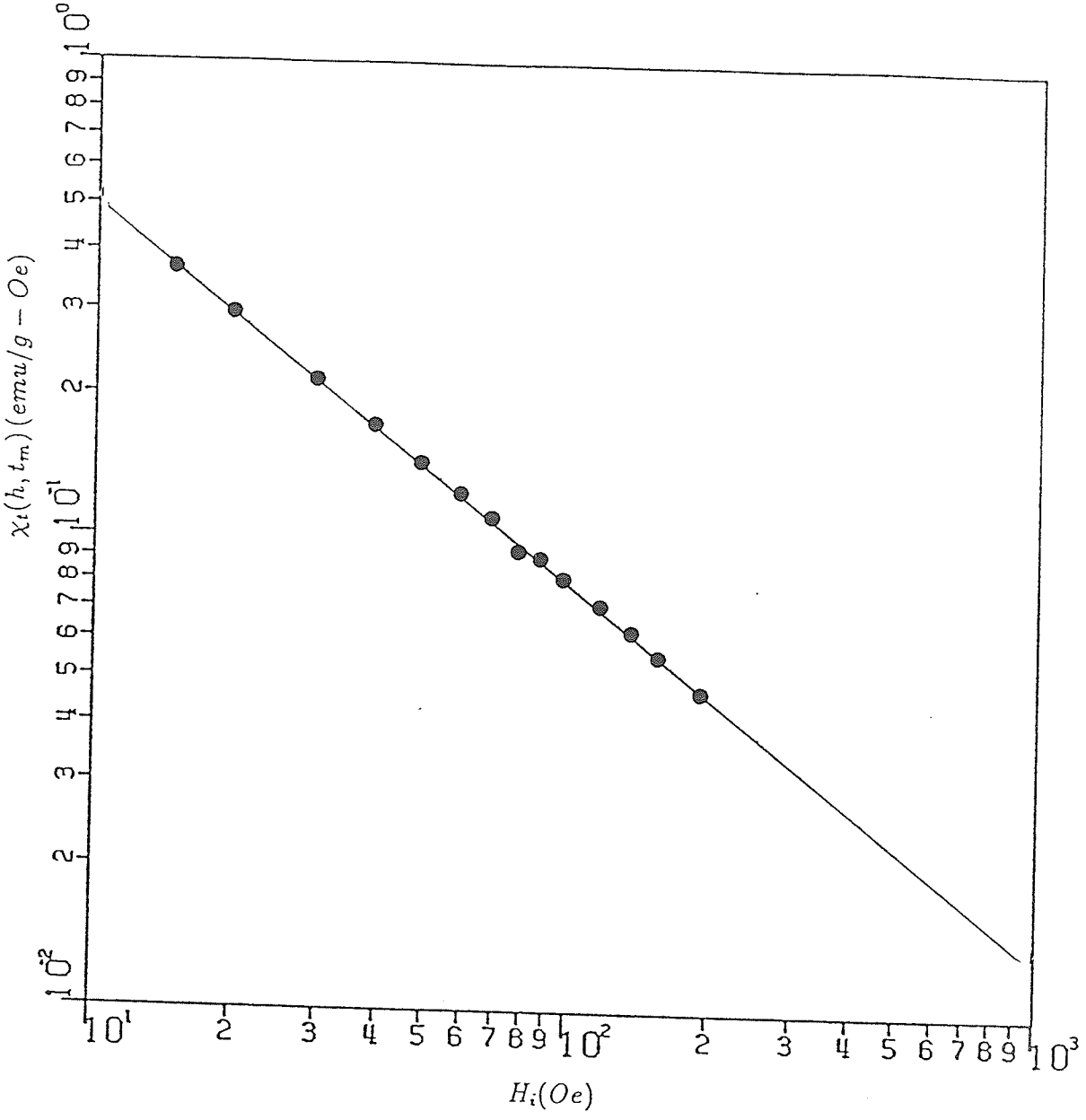

Figure 3.10: $\chi_t(h, t_m)$ vs. H_i for $Fe_{91}Zr_9$ (δ plot).

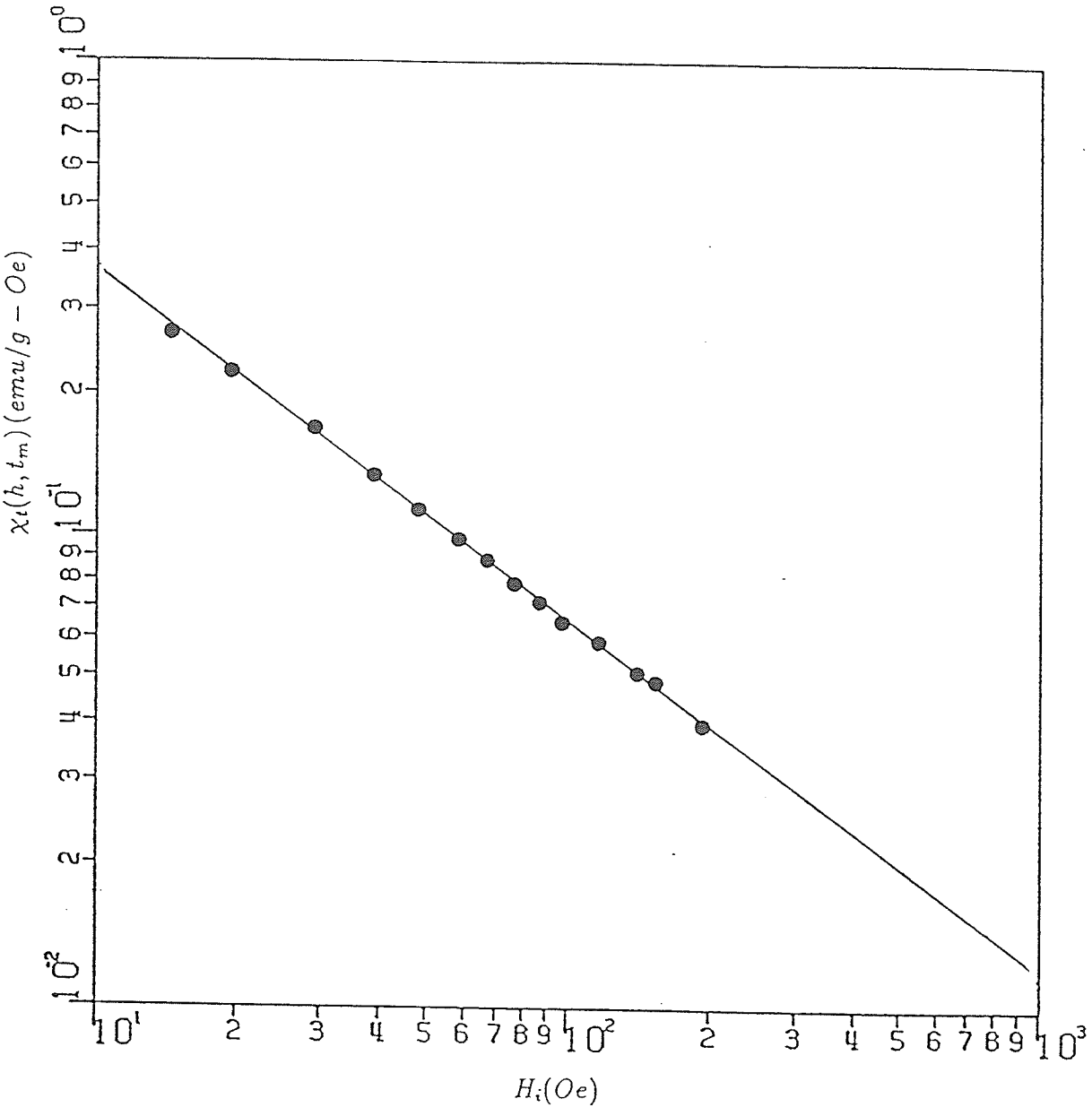

Figure 3.11: $\chi_t(h,t_m)$ vs. H_i for $Fe_{90}Zr_{10}$ (δ plot).

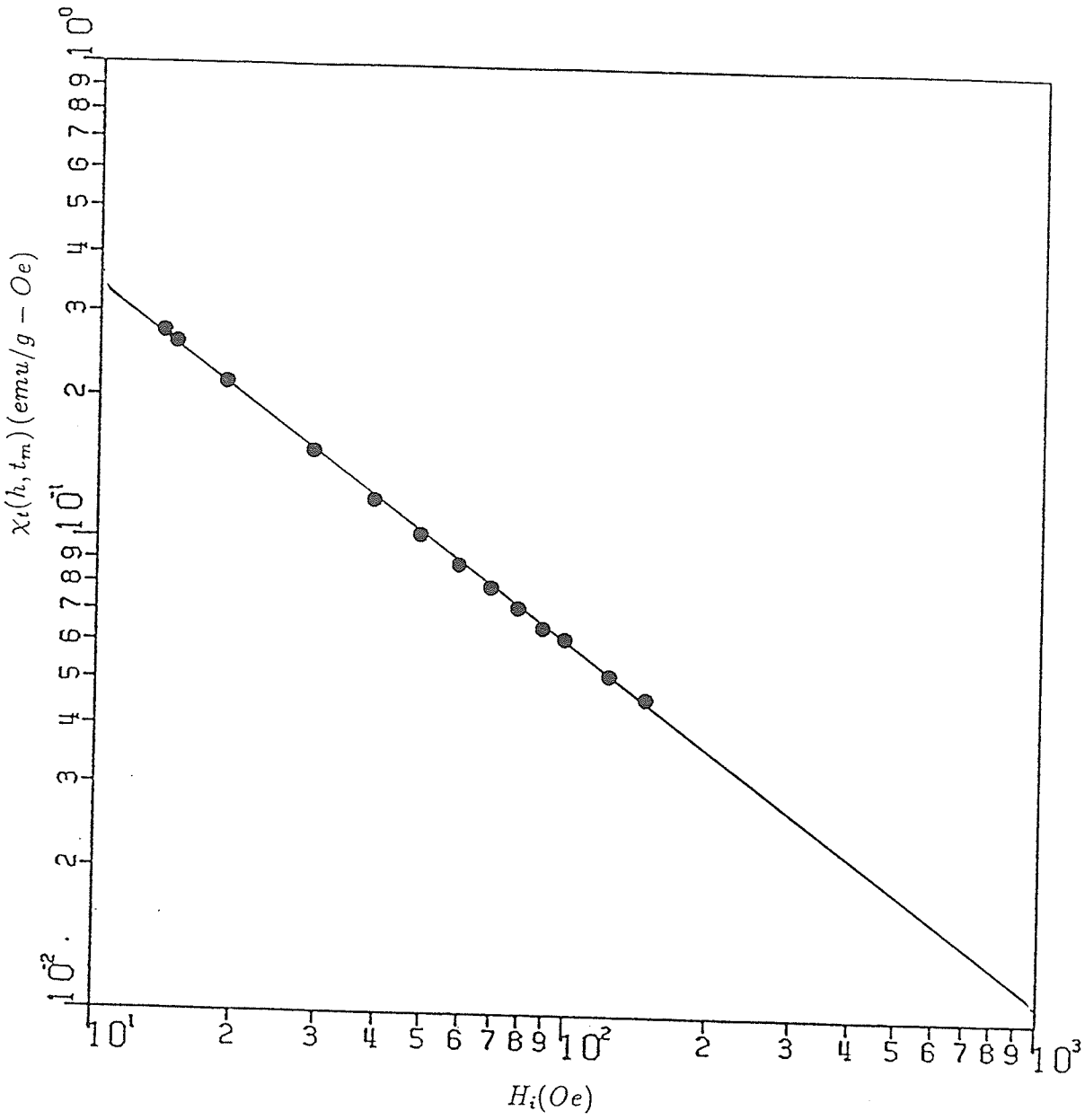

Figure 3.12: $\chi_t(h,t_m)$ vs. H_i for $Fe_{89}Zr_{11}$ (δ plot).

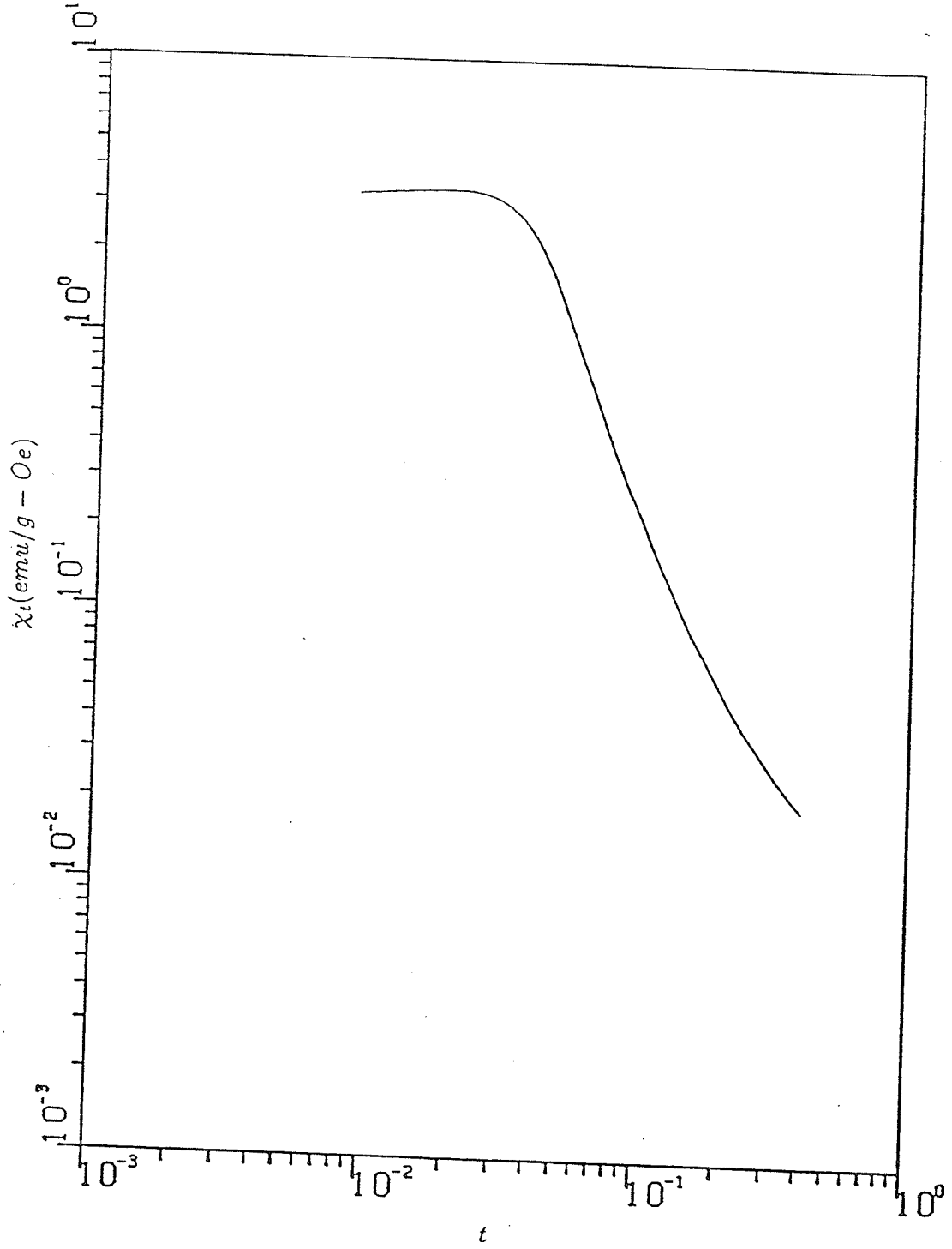

Figure 3.13: $\chi_t(0,t)$ vs. t for $Fe_{92}Zr_8$.

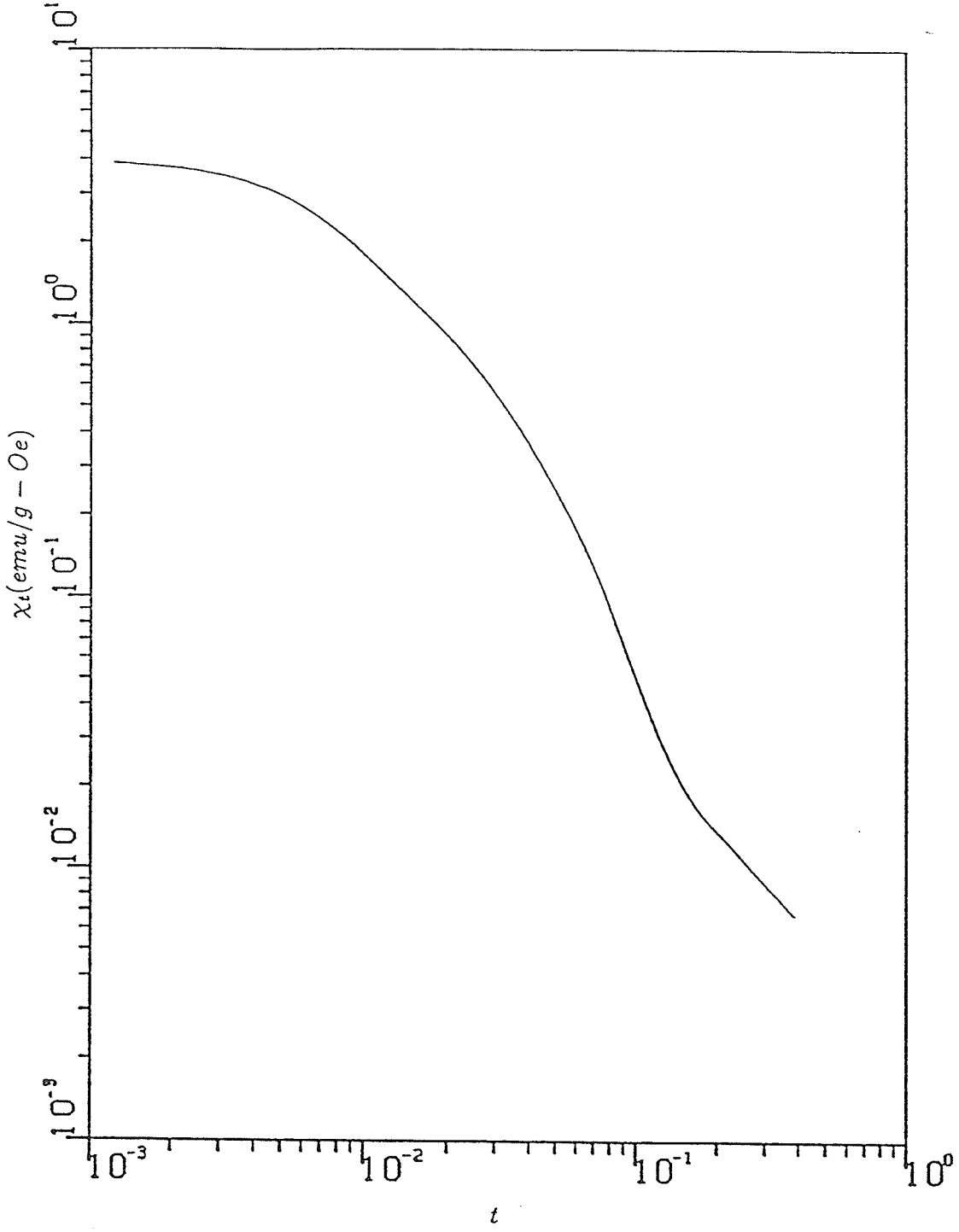

Figure 3.14: $\chi_t(0,t)$ vs. t for $Fe_{91}Zr_9$.

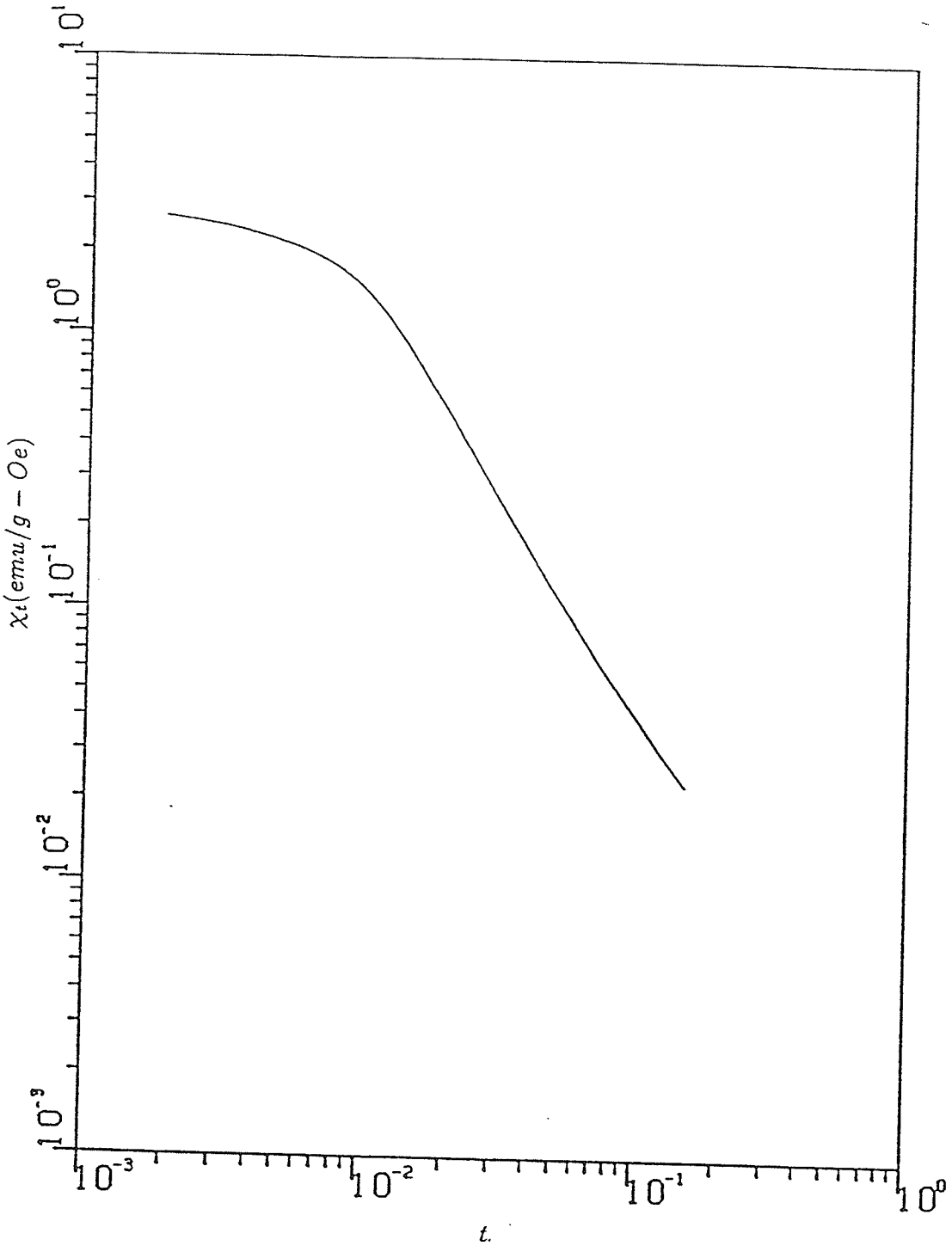

Figure 3.15: $\chi_t(0,t)$ vs. t for $Fe_{90}Zr_{10}$.

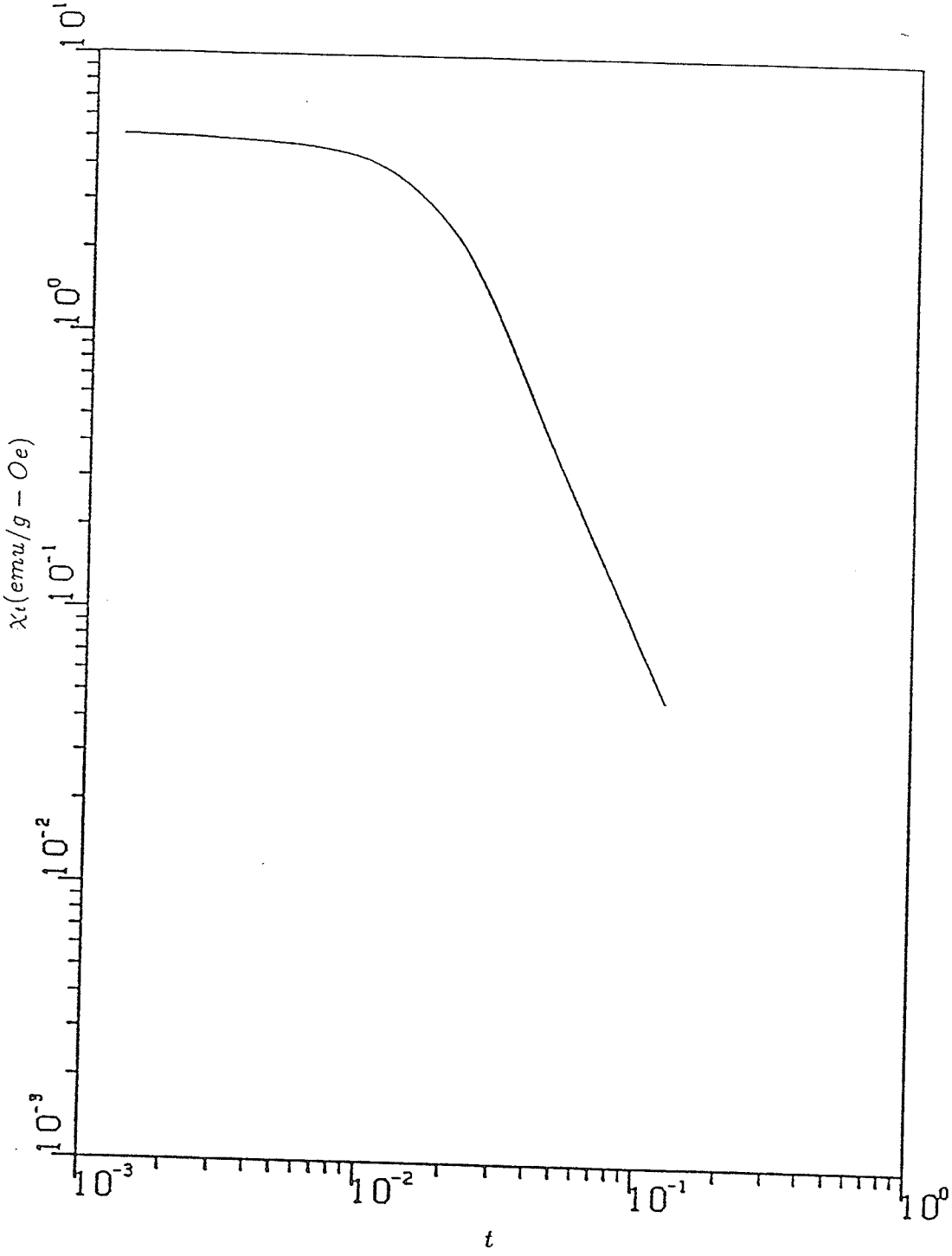

Figure 3.16: $\chi_t(0,t)$ vs. t for $Fe_{89}Zr_{11}$.

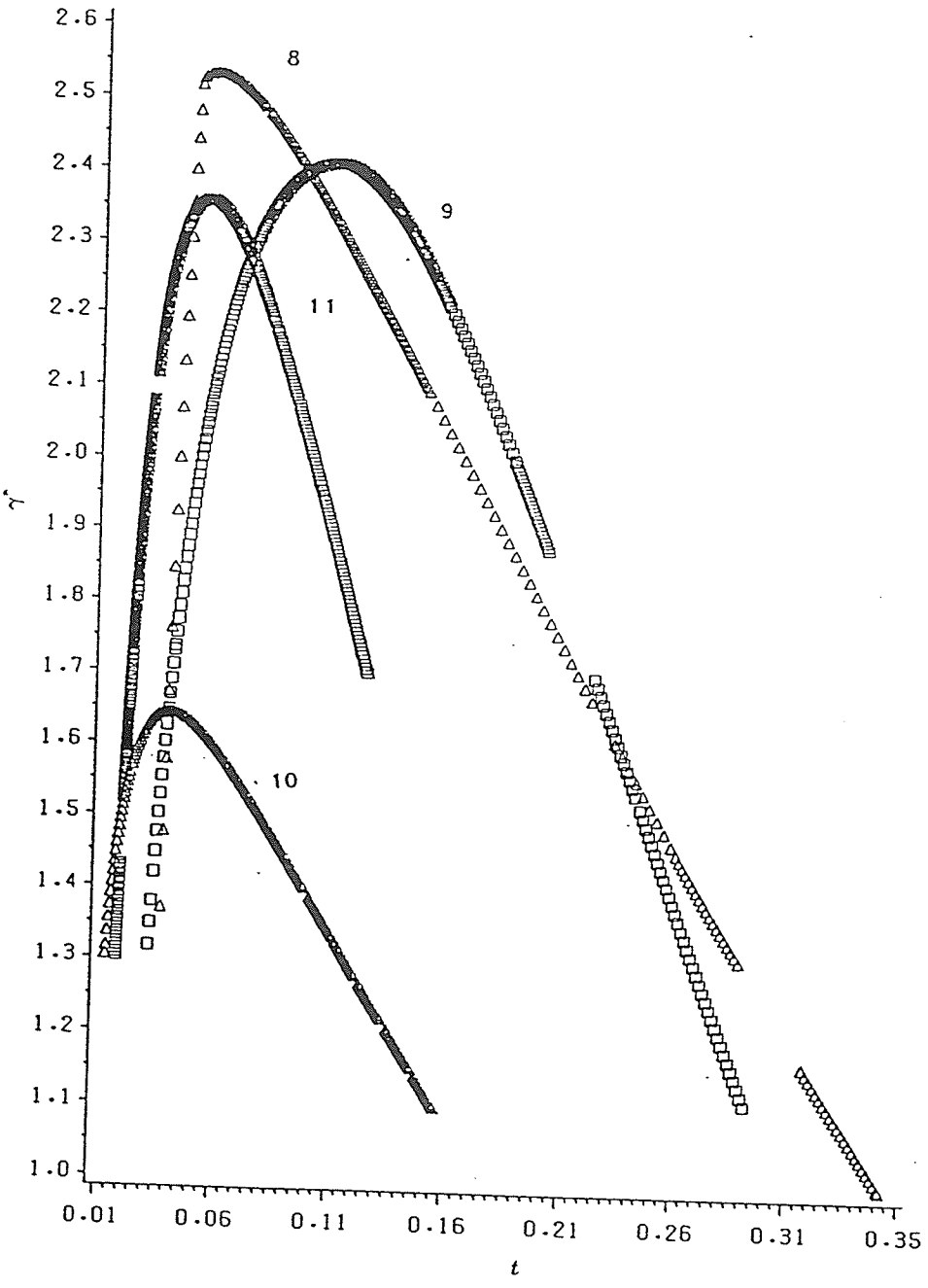

Figure 3.17: γ^* vs. t (reduced temperature) for $Fe_{100-x}Zr_x$ system with $x = 8, 9, 10, 11$.

3.2 Magnetoresistance

3.2.1 Correction of the Data

The typical dimensions of a sample used in the measurement of the SRA are approximately $(3.2 \times 0.1 \times 0.002)$ cm, with a corresponding demagnetizing factor of approximately (0.0008, 0.2, 12.2) along these three directions. As discussed previously an internal field correction is also necessary for the SRA data, particularly when the magnetic field is applied along the transverse direction of the sample, since N is large in this direction. Since

$$H_i = H_a - NM, \tag{3.14}$$

the internal field can be obtained from

$$H_i = H_a - N \int_0^{H_i} \chi_t dH_i \tag{3.15}$$

or equivalently

$$H_i = H_a - N \int_0^{H_a} \chi_m dH_a. \tag{3.16}$$

The integration is performed numerically using the trapezoidal rule. For the longitudinal resistivity data, N is extremely small; hence the internal field is not significantly different from the external field H_a, which can then be used

in place of H_i on the right side of Eq. 3.15. Thus

$$H_i = H_a - N \int_0^{H_a} \chi_t dH_a. \tag{3.17}$$

The χ_t versus H_a data are obtained from field sweep measurements, as shown in Fig.3.18.

For transverse resistance measurements, however, the demagnetizing factor is very large, so that the internal field cannot be replaced by the external field H_a. In this case Eq. 3.16 must be used. Since the transverse susceptibility cannot be measured in the present cryostat, it was estimated using the following procedure: the measured susceptibility $\chi_{m\perp}(0)$ (in zero field) along the transverse direction cannot exceed the demagnetizing limit $1/N_\perp$; thus as an approximation, we take

$$\chi_{m\perp}(h) = \frac{1}{N_\perp} \left(\frac{\chi_{m\|}(h)}{\chi_{m\|}(0)} \right). \tag{3.18}$$

In this way, $\chi_{m\perp}(h)$ vs. H_a along the transverse direction can be estimated from the data measured along the longitudinal direction.

3.2.2 Results

As mentioned in Chapter One, the spontaneous magnetoresistance anisotropy ratio is defined as

$$\frac{\triangle\rho}{\rho_0} = \frac{\rho_\|(B \to 0) - \rho_\perp(B \to 0)}{\rho_0}, \tag{3.19}$$

where ρ_0 is the resistivity in zero field. As shown in Fig. 3.19–Fig. 3.21. a non-zero SRA develops at the ferromagnetic ordering temperature T_c, with $\rho_{\|} > \rho_{\perp}$, and the SRA increases with decreasing Fe concentration (Ref Fig.3.22–Fig.3.25). Table 3.2 lists the SRA for several $FeZr$ samples of different composition measured at several different temperatures.

Table 3.2: SRA, $(\rho_{\|} - \rho_{\perp})/\rho_0$ ($\times 10^{-4}$, error: $\pm 1.5 \times 10^{-4}$) for the $Fe_{100-x}Zr_x$ system at several different temperatures.

	$1.5K$	$4.2K$	$60K$	$77K$	$295K$
$Fe_{92}Zr_8$	21	19	24	22	0
$Fe_{91}Zr_9$	29	27	28	24	0
$Fe_{90}Zr_{10}$	41	38	30	29	0
$Fe_{89}Zr_{11}$	39	45	34	30	0

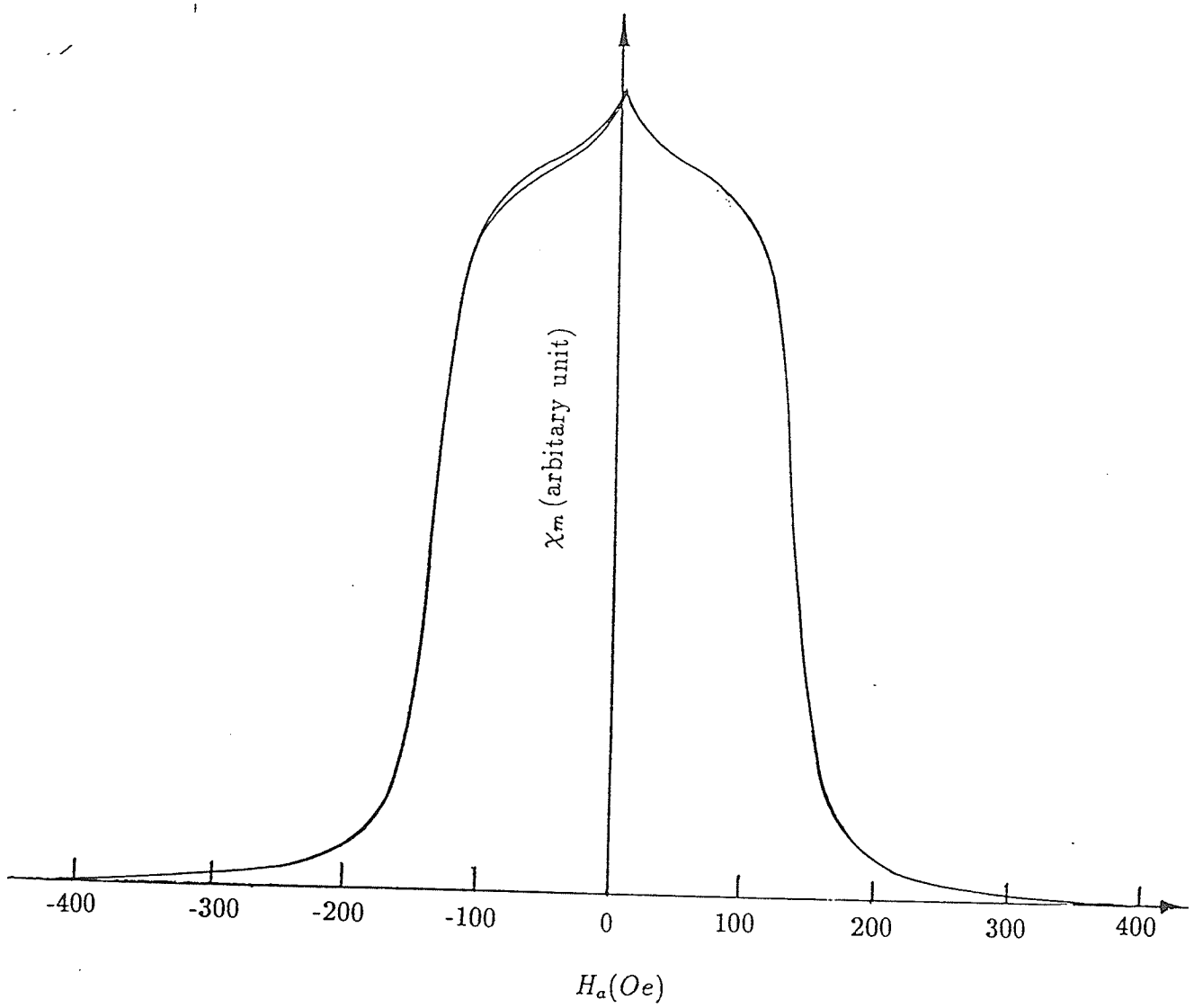

Figure 3.18: $\chi_m(h)$ vs. H_a for $Fe_{91}Zr_9$ at $77K$.

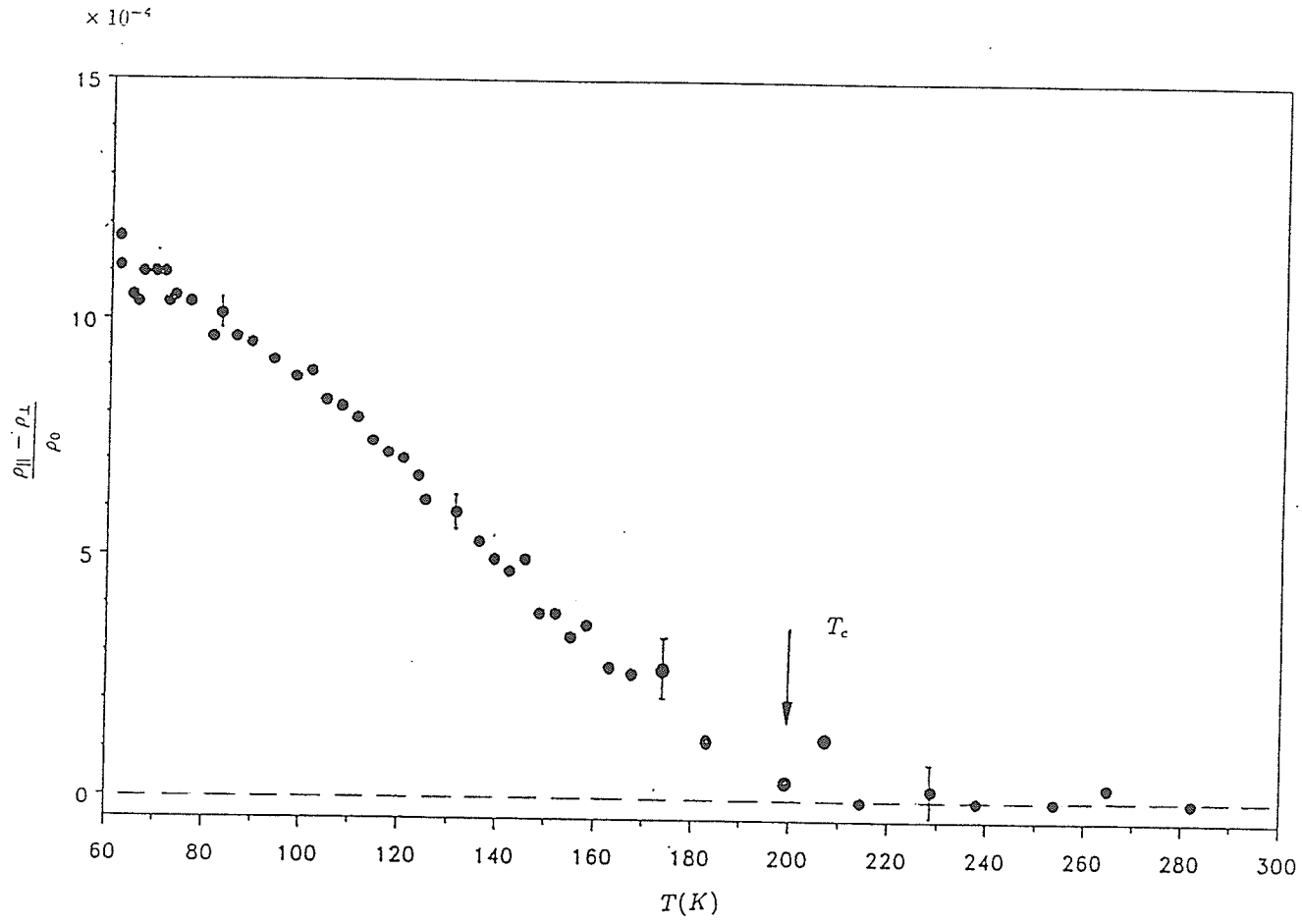

Figure 3.19: SRA vs. temperature for $Fe_{91}Zr_9$.

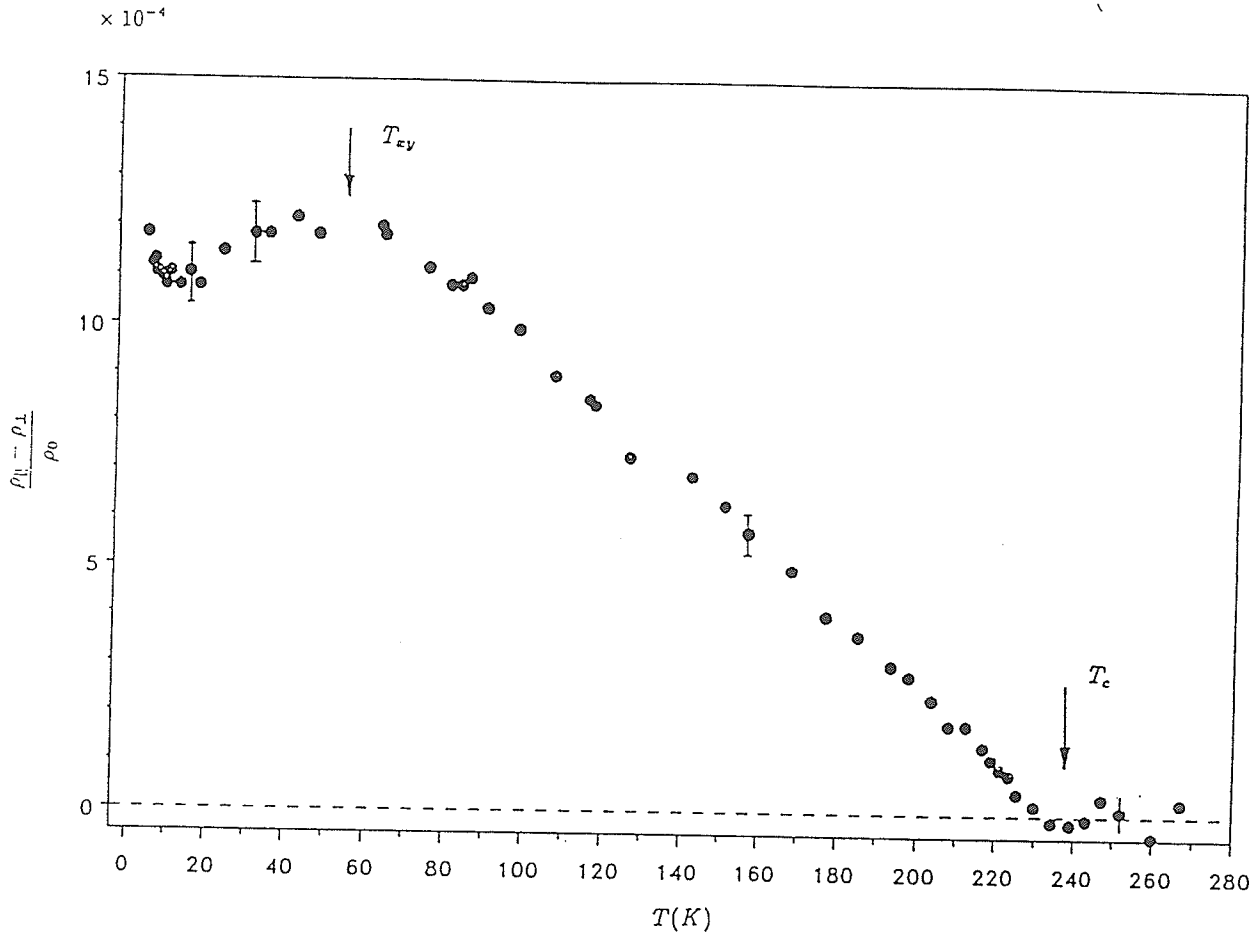

Figure 3.20: SRA vs. temperature for $Fe_{90}Zr_{10}$.

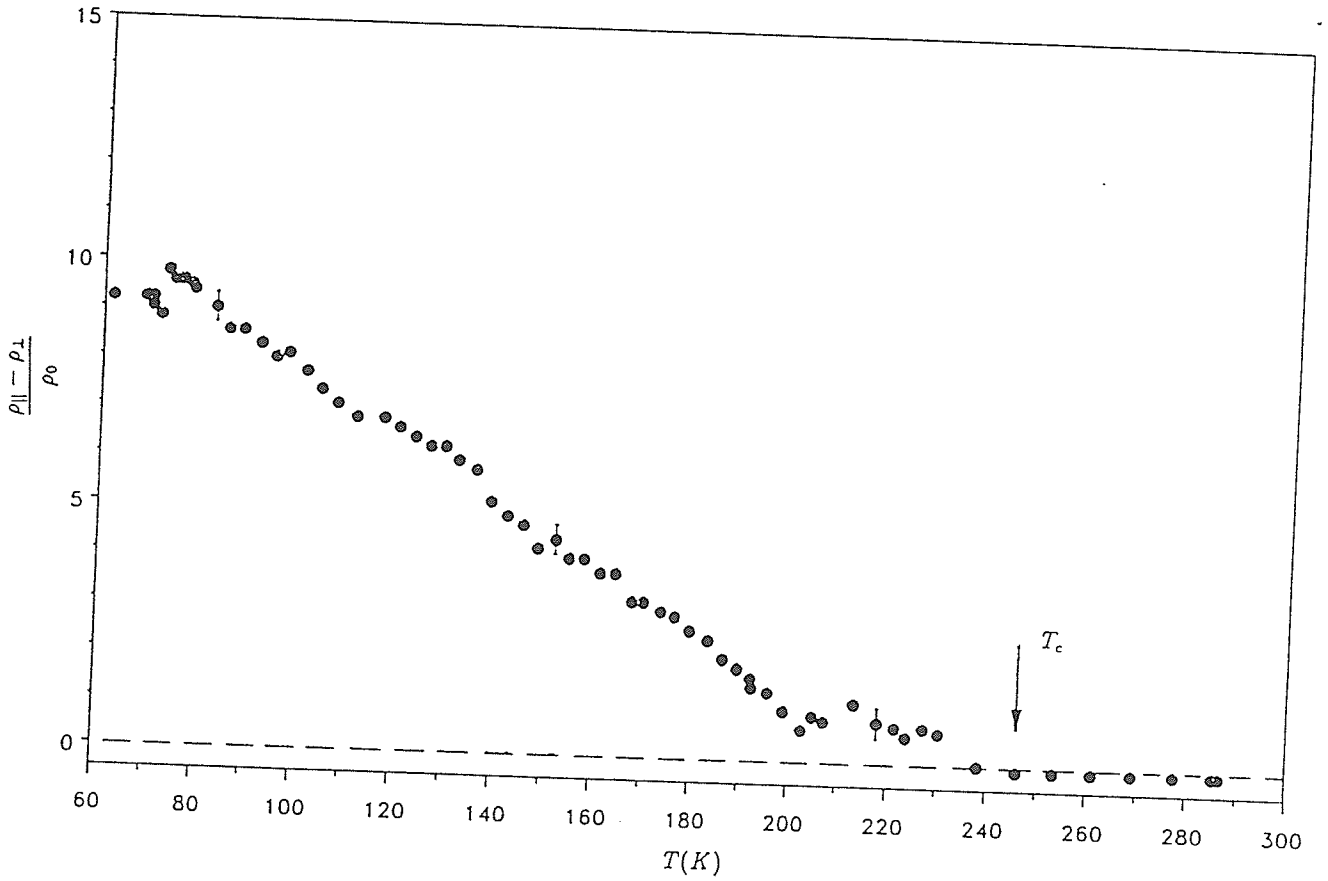

Figure 3.21: SRA vs. temperature for $Fe_{89}Zr_{11}$.

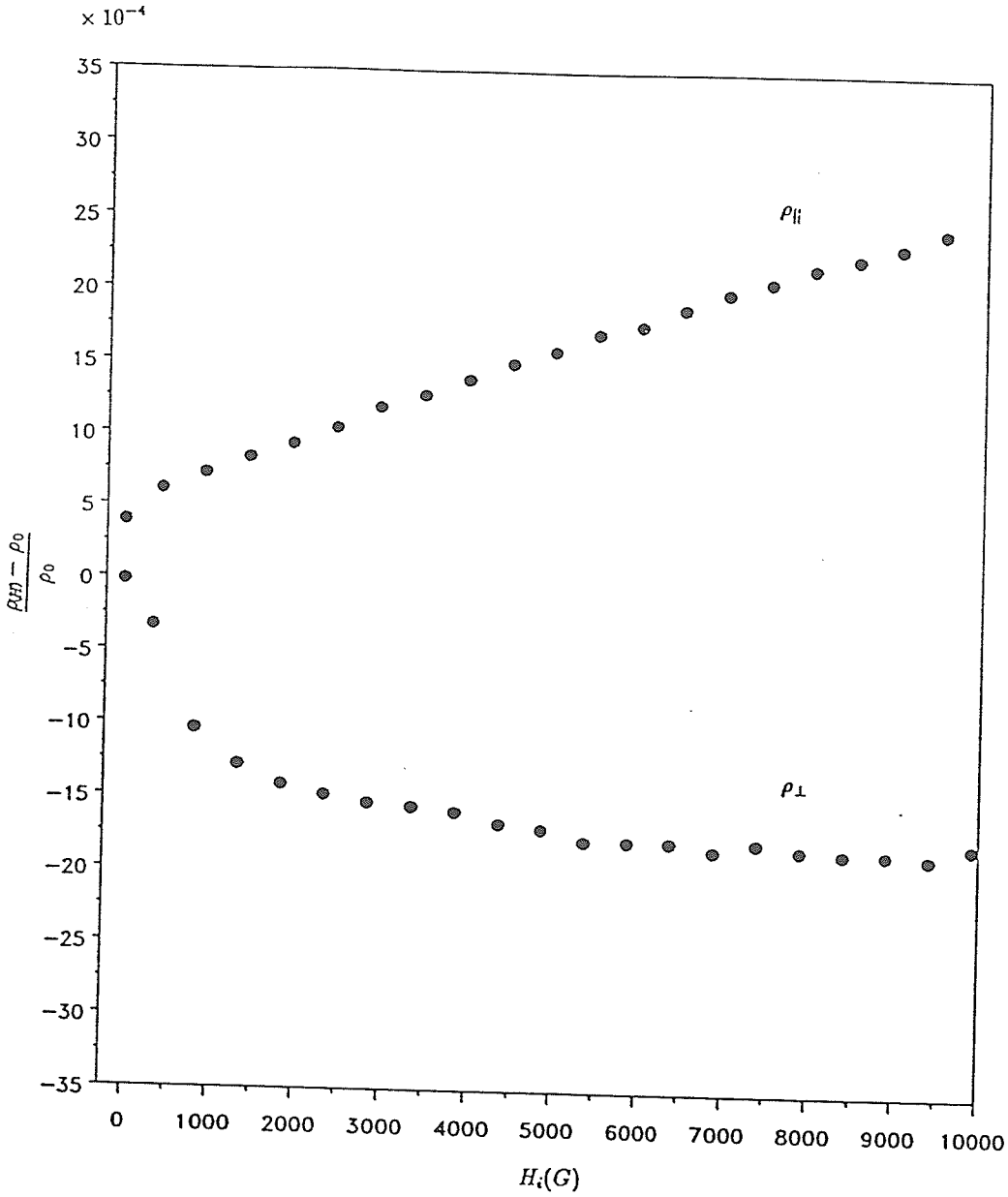

Figure 3.22: Magnetoresistivity vs. internal field for $Fe_{92}Zr_8$ at $77K$.

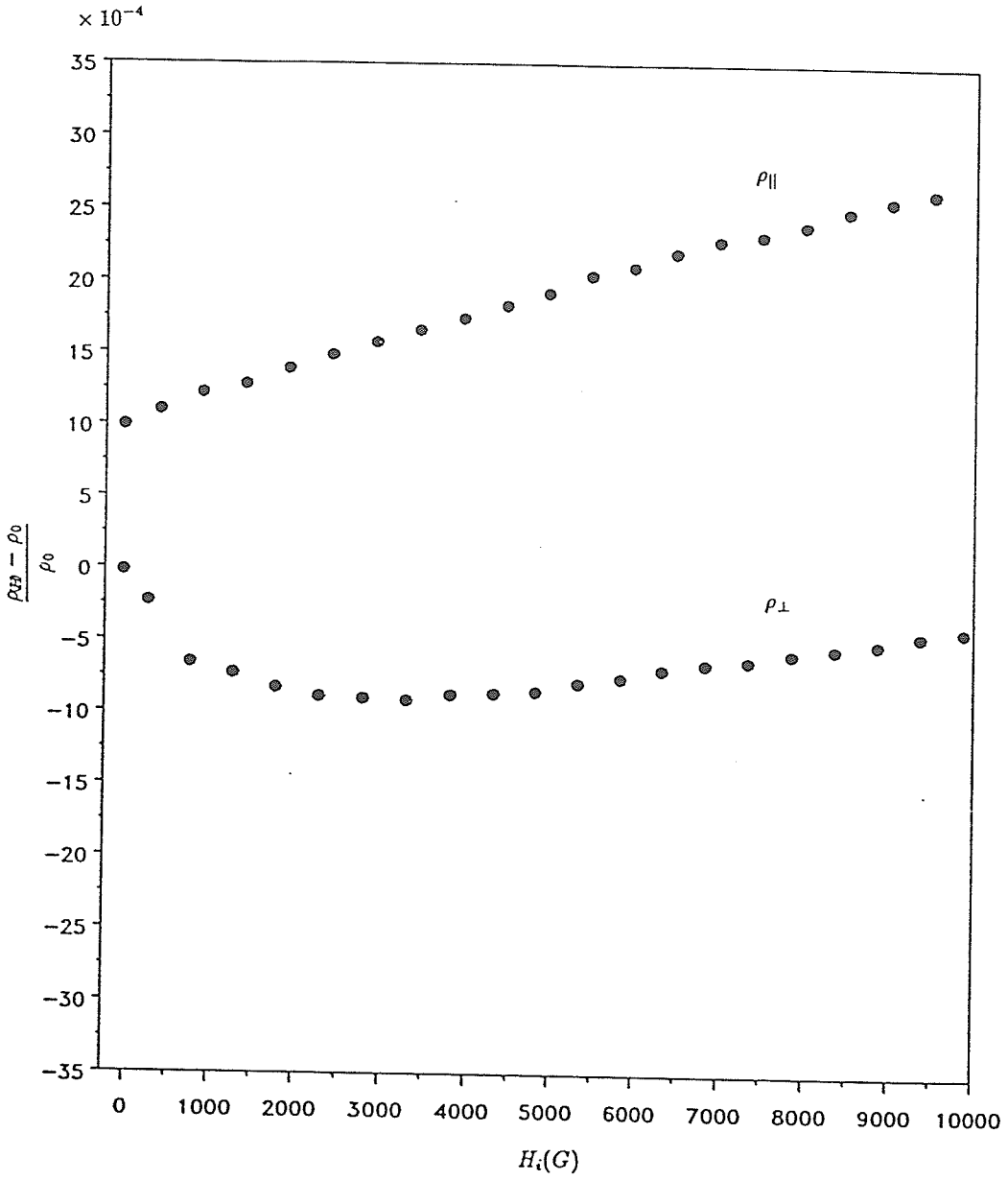

Figure 3.23: Magnetoresistivity vs. internal field for $Fe_{91}Zr_9$ at $77K$.

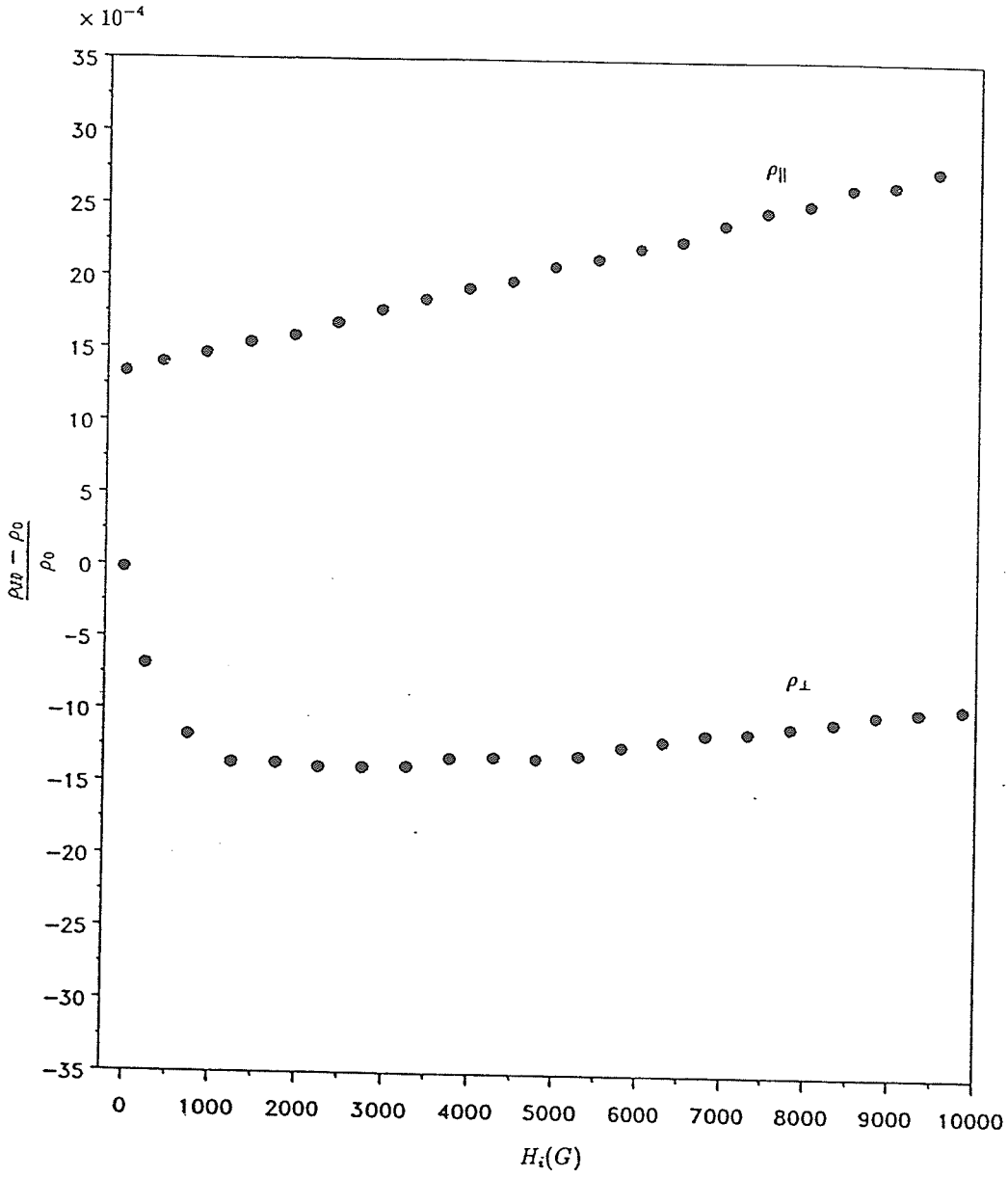

Figure 3.24: Magnetoresistivity vs. internal field for $Fe_{90}Zr_{10}$ at $77K$.

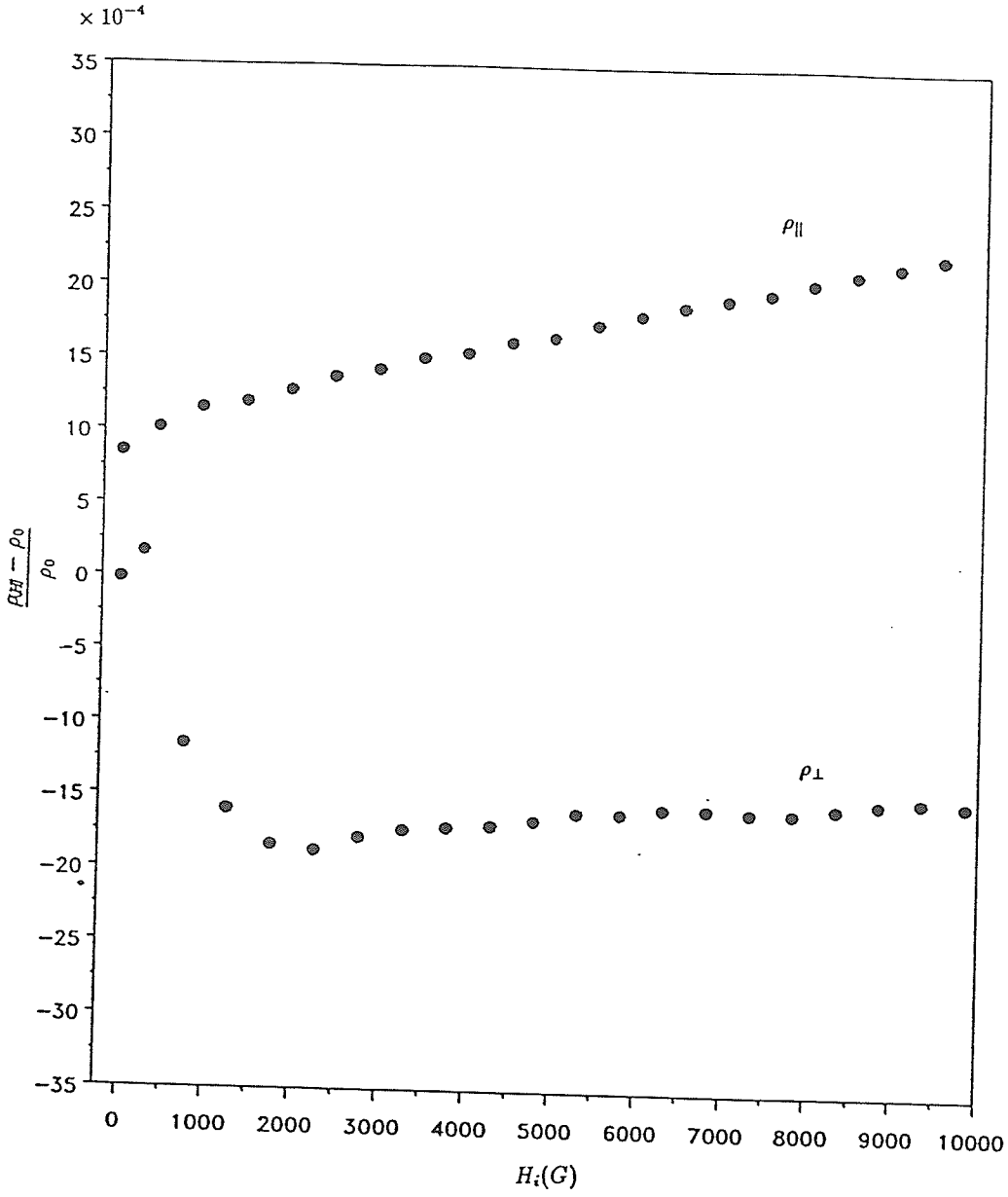

Figure 3.25: Magnetoresistivity vs. internal field for $Fe_{89}Zr_{11}$ at $77K$.

3.3 Discussion

3.3.1 Upper Transition

Recent investigations of magnetic phase transitions in amorphous and disorded ferromagnets have shown[2] that there is no influence of structural disorder on the value of the asymptotic critical exponents, in accordance with the Harris criterion[3]. The Harris criterion predicts that for systems with annealed (mobile) disorder (a) a renomalization of the static exponents takes place when the specific heat critical exponent of the pure (orderd) system, $\alpha_p > 0$, (b) the static exponents remain unaltered when $\alpha_p < 0$, and (c) logarithmic corrections become important for $\alpha_p = 0$. For temperatures outside the asymptotic region ($|t| \geq 10^{-2}$), the Kouvel-Fisher exponent $\gamma^*(T)$ behaves quite differently for ordered and disordered materials. Thus the critical exponents are the important parameters describing the magnetic state that a system enters at the ordering temperature.

For the $Fe_{100-x}Zr_x$ system with $8 \leq x \leq 11$, the nature of the magnetic structure this system possesses in the different temperature ranges are still controversial. Kaul *et al.*[4] obtained asymptotic critical exponents consistent with the 3-D classical Heisenberg model, which led them to the conclusion that the system enters a true ferromagnetic state at T_c. By contrast some authors[5] reported γ exponent values averaged over a wide temperature range, and thus obtained larger values than those predicted by the Heisenberg model for reasons outlined earlier.

In the present investigation we obtained the temperature dependence of the effective exponent, $\gamma^*(T)$, from our A.C. susceptibility measurement by first fitting a polynomial through the $\log\chi(0,t)$ vs. $\log t$ data, and then estimating the slope (and then $\gamma^*(T)$) at every point from the computed fit. As indicated previously each $\gamma^*(T)$ plot exhibits a non-monotonic temperature dependence, with a maximum value at a temperature $t_0(t_0 > 0)$. The value of $\gamma^*(T)$ value starts at about 1.3 at a reduced temperature, t, of approximately 2×10^{-2}, increases with temperature up to a maximum and then decreases to the mean field value $\gamma = 1$ at higher temperatures. This behaviour is in contrast with that of ordered magnetic materials for which the value of $\gamma^*(T)$ decreasing monotonically to 1 with increasing temperature. We believe this non-monotonic $\gamma^*(T)$ behavior of the $FeZr$ system is the consequence of its disorderd structure, as predicted by both theory and found experimentally[6][7].

Although we do observe that $\gamma^*(T)$ decreases towards 1.38 (i.e. the isotropic 3−D Heisenberg value) when the system approaches the asymptotic region below t_0, we cannot be certain that this is the asymptotic value, since these data do not extend below $t = 10^{-2}$; however, a value for γ of 1.38 is obtained at about the upper limit of the temperature range that Kaul used for fitting their data.

Another view of the phase transition at T_c has been proposed by Ryan and Coey[8], who suggest that the system enters a "wandering-axis" ferromagnetic state at T_c with a finite correlation length as shown in Fig.3.26. If

this were indeed the case then it would have the following consequence as far as the zero-field susceptibility is concerned.

Bearing in mind that for true ferromagnetic materials the susceptibility $\chi(0,t)$ and correlation length $\xi(t)$ in zero field both diverge with the exponents γ and ν respectivly in the critical region $(T \geq T_c)$, i.e.

$$\chi(0,t) \propto t^{-\gamma}, \tag{3.20}$$

$$\xi(t) \propto t^{-\nu}, \tag{3.21}$$

then it follows that

$$\chi(0,t) \propto (t^{-\nu})^{\gamma/\nu} \propto \xi^{\gamma/\nu}. \tag{3.22}$$

This means that if the system enters a long range ferromagnetic state, it will show a linear double logarithmic plot of susceptibility against reduced temperature over a wide range. By contrast, if the correlation length $\xi(t)$ does not diverge, the $\log \chi(0,t)$ vs. $\log t$ plot will break away from the straight line at a certain reduced temperature t_w as shown in Fig.3.27, with a "saturated" correlation length λ_c given by

$$\lambda_c = \xi(t_w). \tag{3.23}$$

The above equation also tells us that t_w can be chosen as a parameter describing the correlation length, if the exponent ν is universal for all materials. So if the $FeZr$ system enters a "wandering-axis" state with a saturated cor-

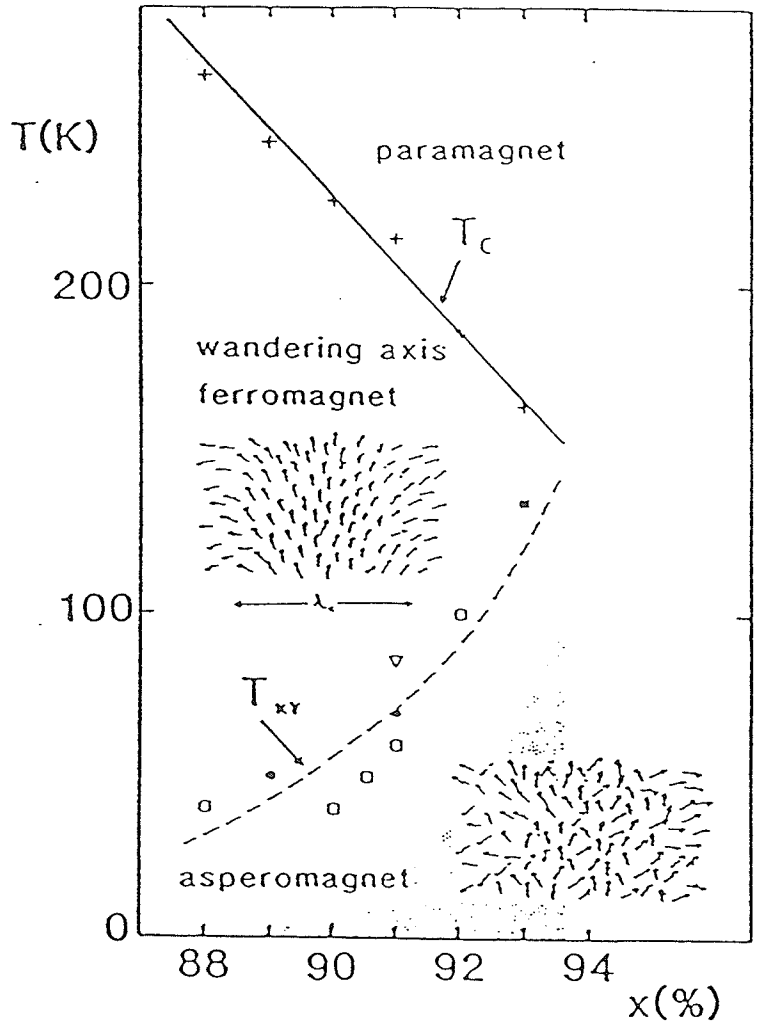

Figure 3.26: Phase diagram for Fe_xZr_{100-x} system[8].

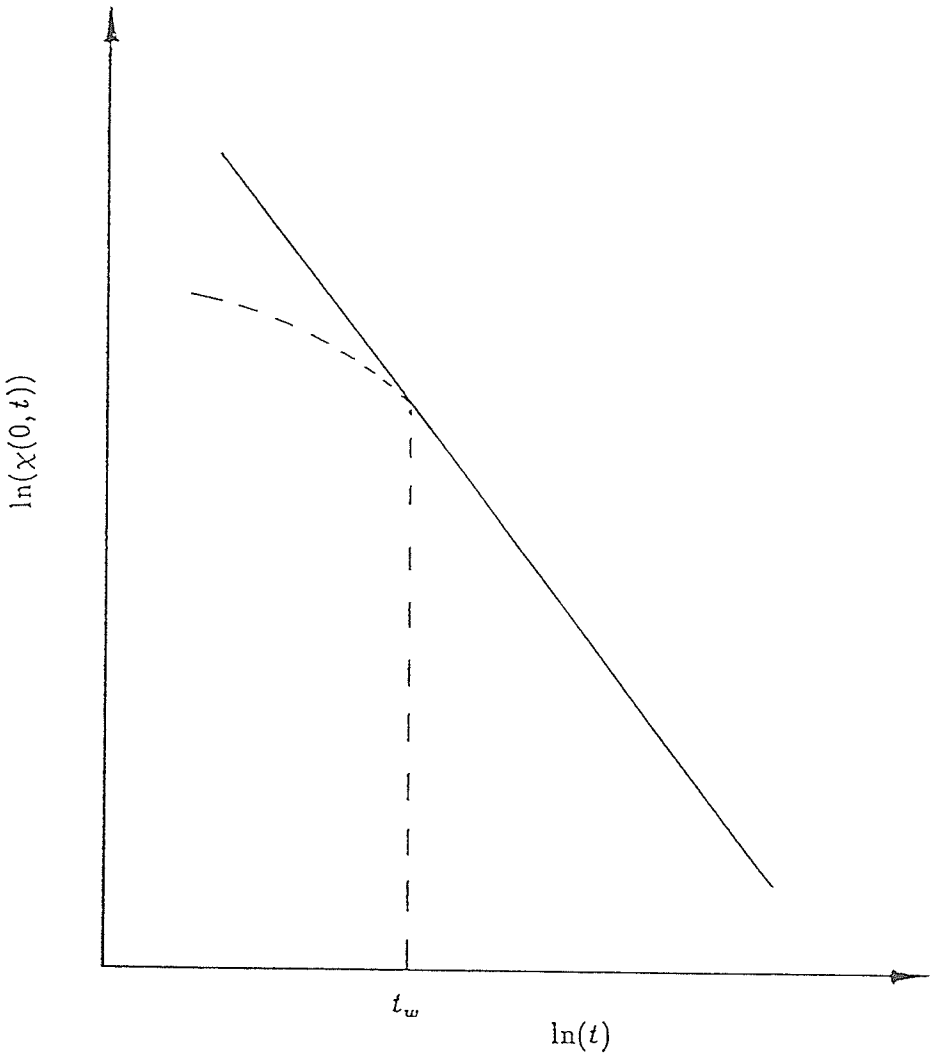

Figure 3.27: Diagram illustrating method for obtaining λ_c from the A.C. susceptibility measurement.

relation length λ_c, we would expect that t_w should increase (i.e. the λ_c should decrease) when the $Fe_{100-x}Zr_x$ system approaches the tri-critical point (i.e. when x approaches 8); our A.C. susceptibility data did not show any clear indication of such a tendency.

On the other hand, as indicated previously, the magnetoresistivity vs. temperature data for $Fe_{100-x}Zr_x$ with $x = 8, 9, 10, 11$, clearly show that a non-zero SRA develops at the ordering temperature T_c, with the result within 2% of the value for T_c obtained from the A.C. susceptibility measurements. The onset of a non-zero SRA is a clear indication[9] that ferromagnetic-like order is established at least for distances comparable with the electronic mean free path, since $\triangle\rho$ relies principally on the existance of two factors, a polarizing field and spin-orbit coupling at the scattering site as discussed in Chapter One. Unfortunately the mean free path in this system is quite small ($\leq$10Å), and as a result a definite conclusion on the nature of the magnetic ordering on this system based on these results is not possible.

3.3.2 Lower Transition

In this investigation, A.C. susceptibility measurements were taken for the $Fe_{92}Zr_8$, from $4.2K$ to the upper transition temperature. Although we observed an abrupt increase of $\chi(0,t)$ at about $55K$, we did not observe any critical peak in this region (with an applied field $H_a = 20Oe, 40Oe, 60Oe$), in contrast to reports by N. Saito *et al.*[9]; furthermore no anomaly at temperatures around $100K$ was observed, the latter being the the suggested lower

transition temperature in Coey's phase diagram for the $FeZr$ system[8].

Another possible indication of a transition from a ferromagnetic state to spin-glass state is an anomaly in the coefficient of the non-linear term in the A.C. susceptibility[11]. The idea is obtained from consideration of the behavior of direct paramagnetic−spin−glass systems.

For direct paramagnetic-spin-glass systems, the A.C. susceptibility is an even function of the field, so $\chi(H,T)$ can be expanded as

$$\chi(H,T) = \chi_0(T) - a_2(T)H^2 + a_4(T)H^4 - \cdots \tag{3.24}$$

where $\chi_0(T)$ is the zero-field susceptibility, and $a_2(T)$, $a_4(T)$ are the coefficients of the higher order terms. In the low-field region, the H^2 term will dominate, and consequently a plot of the $\chi(H,T)$ vs. H^2 will initially be linear but will begin to curve at higher fields where the higher order terms $(H^4, \cdots)$ begin to show their effect. The coefficient a_2 can be obtained from the slope of this linear region.

Bearing in mind that the spin glass order parameter $q = \langle\langle S_z^2\rangle_T\rangle_J$ couples to the non-linear response at a direct paramagnetic−spin−glass transition leading to a divergence of $a_2(T)$, we might expect an anomaly to be present at the ferromagnetic−spin−glass transition; such an anomaly has been reported recently[10] for the $(PdFe)Mn$ system. We have attempted this type of analysis for samples of $Fe_{92}Zr_8$ and $Fe_{91}Zr_9$. As shown in Fig. 3.28 and Fig. 3.29, a plot of $a_2(T)$ does show an anomaly in the region where the $\chi(0,t)$ increase abruptly, i.e. near $62K$ and $35K$ respectivly. These

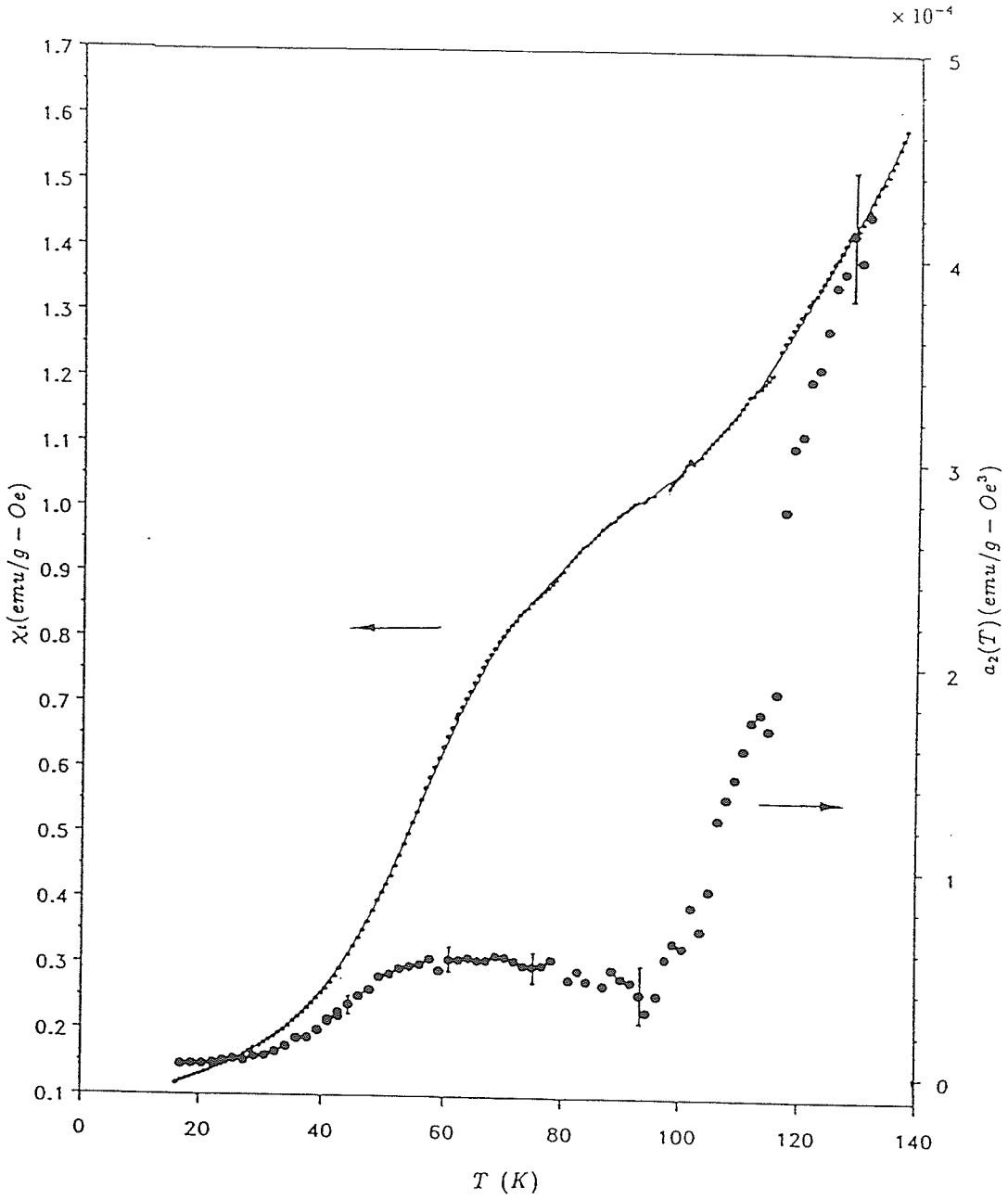

Figure 3.28: The temperature dependence of the coefficient $a_2(T)$ and the A.C. susceptibility for $Fe_{92}Zr_8$.

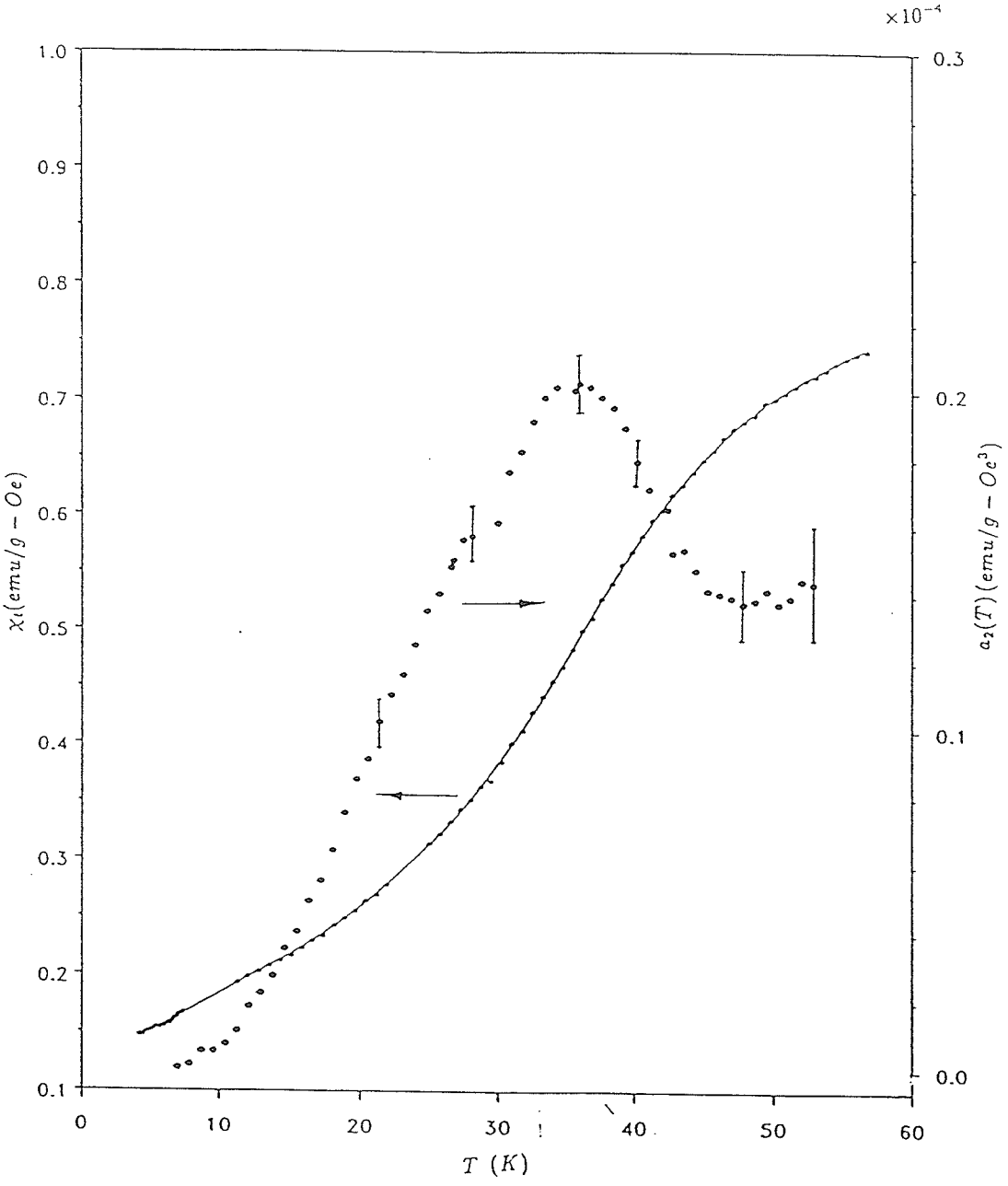

Figure 3.29: The temperature dependence of the coefficient $a_2(T)$ and the A.C. susceptibility for $Fe_{91}Zr_9$.

temperatures are about $30K$ lower than those suggested by Coey[8] ($95K$ and $70K$ for $Fe_{92}Zr_8$, $Fe_{91}Zr_9$ respectively). This may be due to differences in the frequency used in the two studies, since the response time of a spin to an applied magnetic field will be strongly temperature dependent near a phase transition, or possibly slight variations from the stoichimetric composition which certainly could produce significant shifts in the observed transition temperature.

The behavior of the non-linear term coefficient $a_2(T)$ in the $FeZr$ system does not show an actual divergence around T_{xy}, only an anomalous peak is observed. However, this would seem reasonable if we consider that this system enters a transverse spin-glass state, in which only the $x-y$ components of the spins are frozen, while the spin component along the z direction retains its ferromagnetic order. The presence of a non-zero spontaneous magnetisation means that there exists a large regular contribution which will affect the non-linear behaviour.

While $a_2(T)$ shows an anomaly around T_{xy}, the SRA measurements do not show any abrupt changes in this region, nor do the plots of magnetoresistivity vs. internal field show any noticeable change. Indeed, there is no theory at present, that we are aware of, which can predict the critical behaviour of the SRA, however, recent experiments[9] have shown that a critical behaviour in the SRA exists near a ferromagnetic percolation threshold. As it is known that the magnetoresistance of a magnetic alloy is very sensitive to changes in the degree of magnetic order on the scale of the electron mean

free path, the failure to observe the critical change in the $FeZr$ system is probably because the correlation length doesn't change when the system enters the transverse spin-glass state from the ferromagnetic state, as observed by Rhyne and Fish[12].

From our investigation of the $Fe_{100-x}Zr_x$ system with composition in the range $x = 8 \sim 11$ using A.C. susceptibility and SRA measurements, we conclude that this system is most probably a vector spin-glass, the transverse spin components of which freeze at the lower transition temperature. We expect that additional systematic studies will be performed to improve the understanding of the magnetic properties of this controversial system.

Reference

[1] J.A. Osborn, Phys. Rev. **67**, 351(1945).

[2] R. Reisser *et al.*, J. Magn. Magn. Mater. **75**, 45(1988).

[3] A.B. Harris, J. Phys. C **7**, 1671(1974).

[4] S.N. Kaul, J. Phys. F **18**, 2089(1988).

[5] H. Yamamoto *et al.*, J. Magn. Magn. Mater. **31-34**, 1579(1983).

[6] M. Fähnle *et al.*, J. Magn. Magn. Mater. **24**, 175(1981).

[7] M. Seeger and H. Kronmüller, J. Magn. Magn. Mater. **78**, 393(1989).

[8] D.H. Ryan and J.M.D. Coey *et al.*, Phys. Rev. B **35**, 8630(1987).

[9] H.P. Kunkel, Z. Wang and G. Williams, J. Phys. F **17**, L157(1987);
J. Phys.: Condens. Matter. **1**, 3381(1989).

[10] N. Saito *et al.* J. Phys. F **16**, 911(1986).

[11] H.P. Kunkel and G. Williams, J. Magn. Magn. Mater. **75**, 98(1988).

[12] J.J. Rhyne and G.E. Fish, J. Appl. Phys. **57**, 3407(1985).

Appendix A

Magnetoresistivity Data

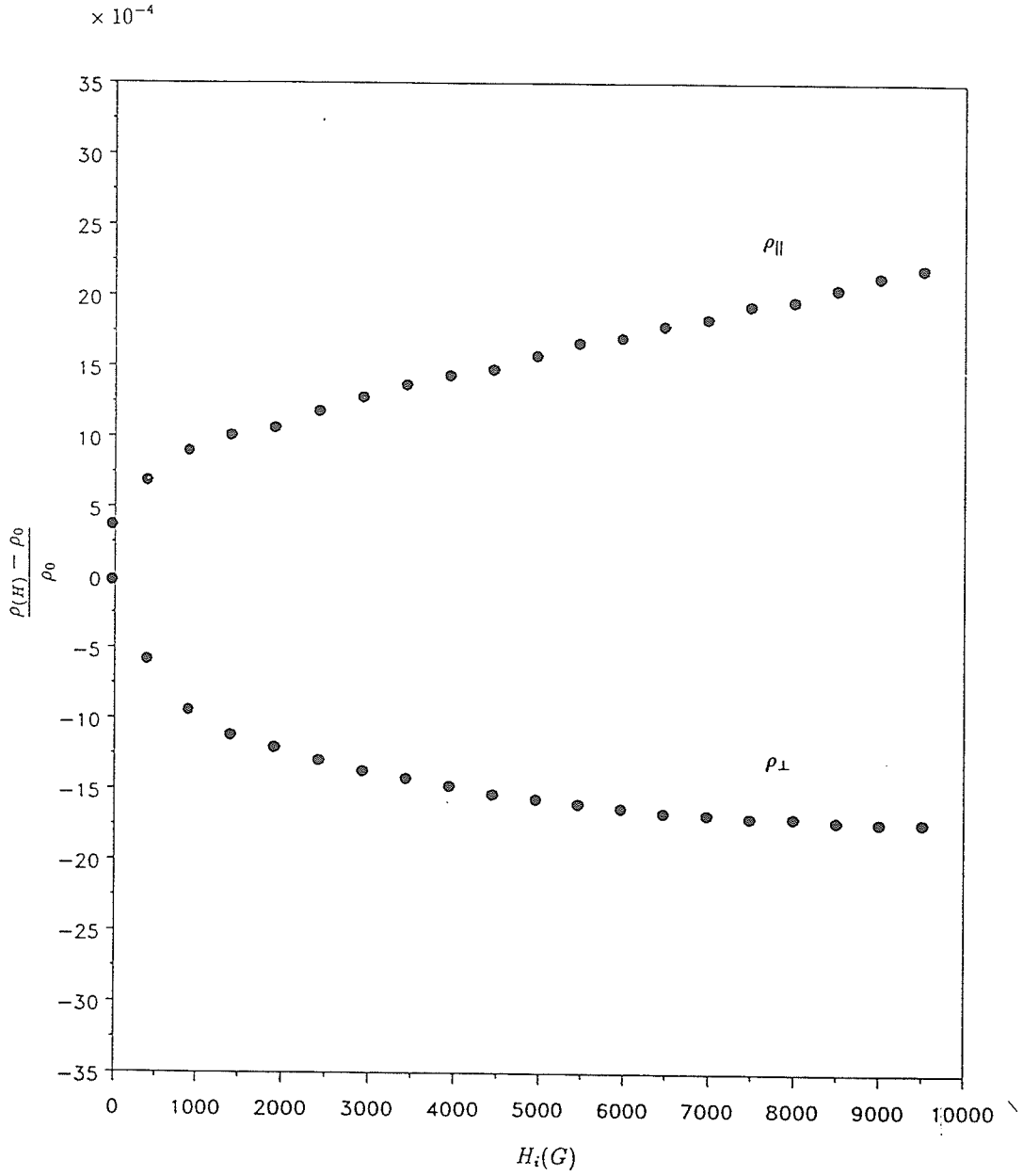

Figure A 1: Magnetoresistivity ratio vs. H_i for $Fe_{92}Zr_8$ at $1.5K$.

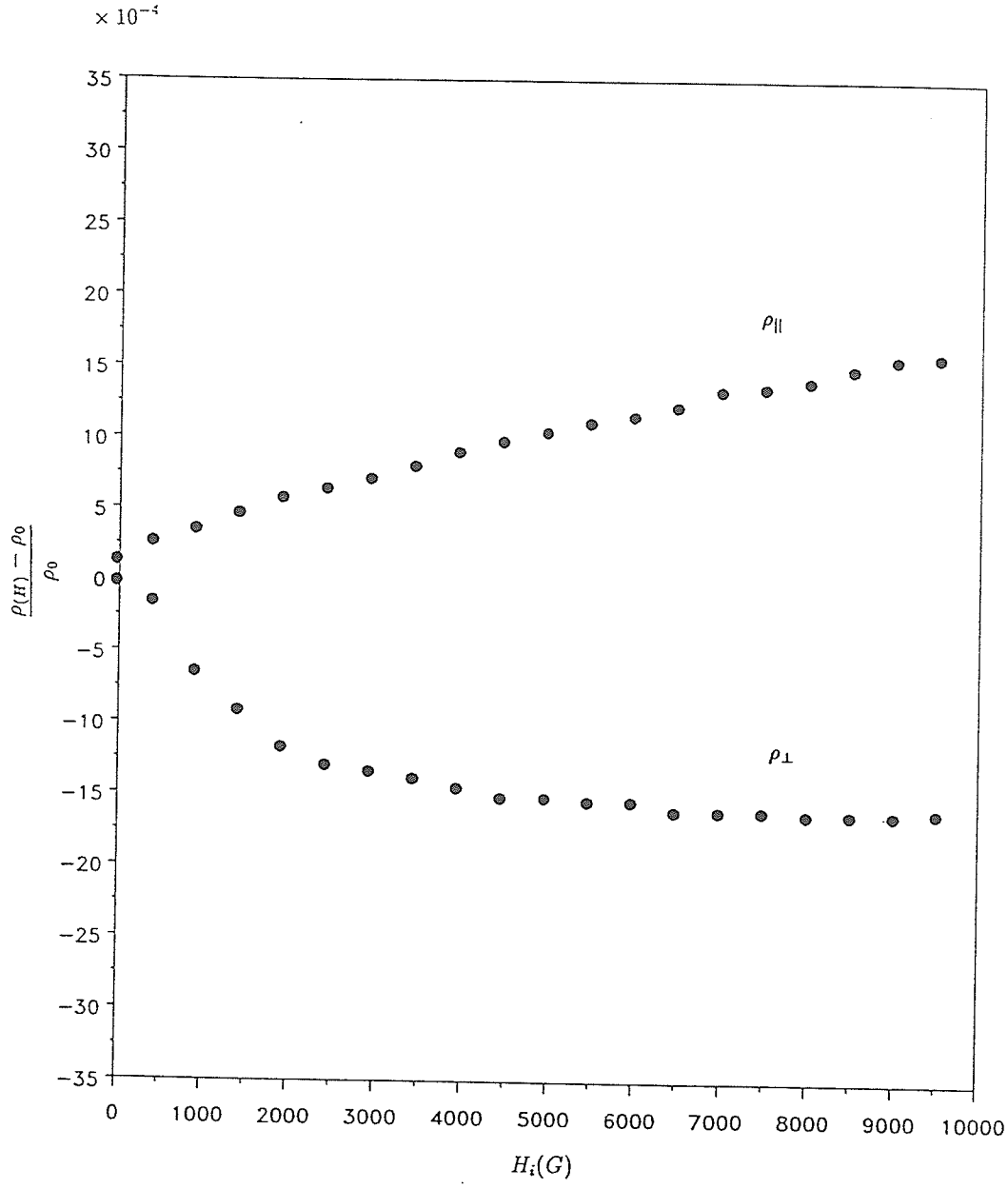

Figure A 2: Magnetoresistivity ratio vs. H_i for $Fe_{92}Zr_8$ at $4.2K$.

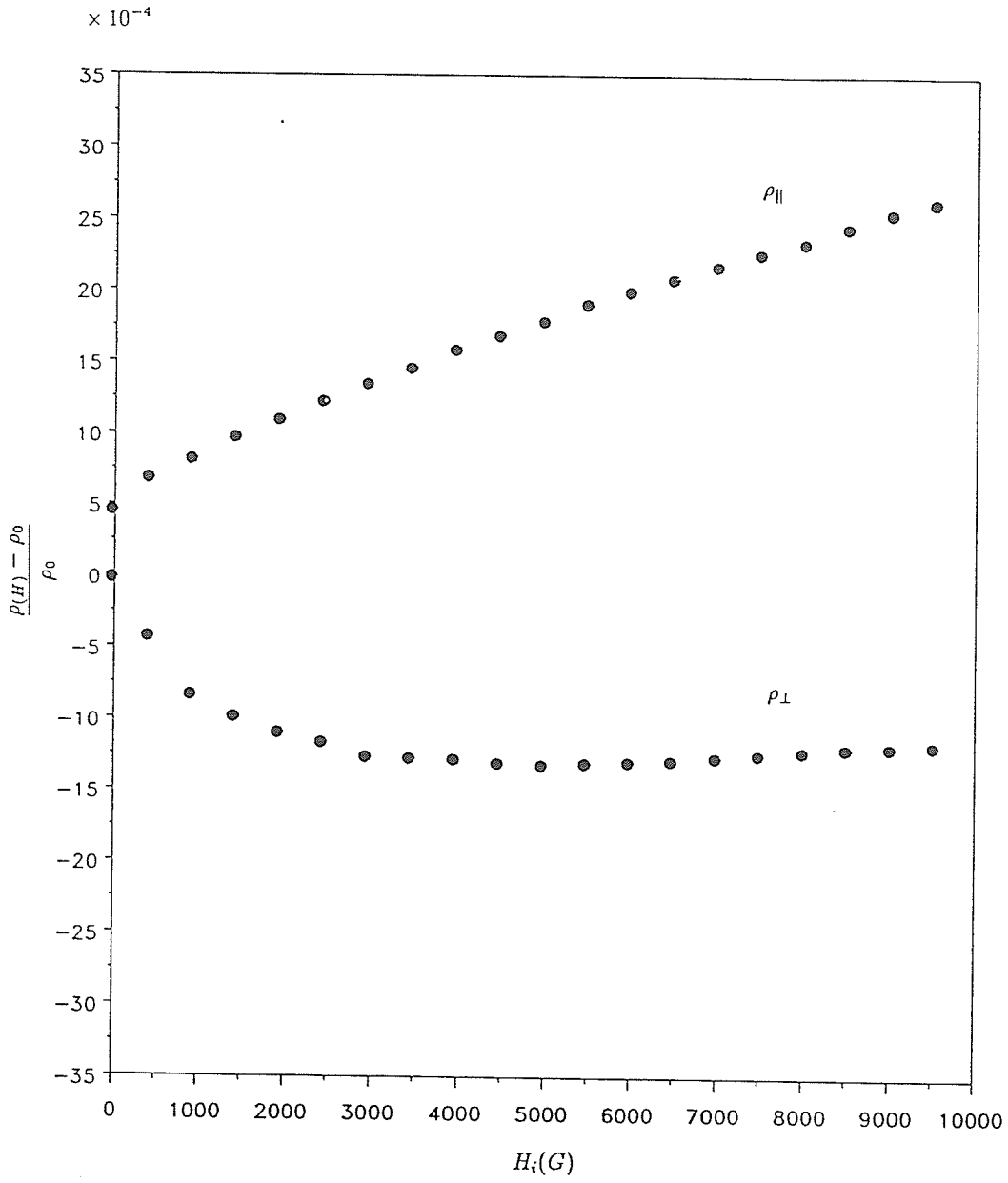

Figure A 3: Magnetoresistivity ratio vs. H_i for $Fe_{92}Zr_8$ at $60K$.

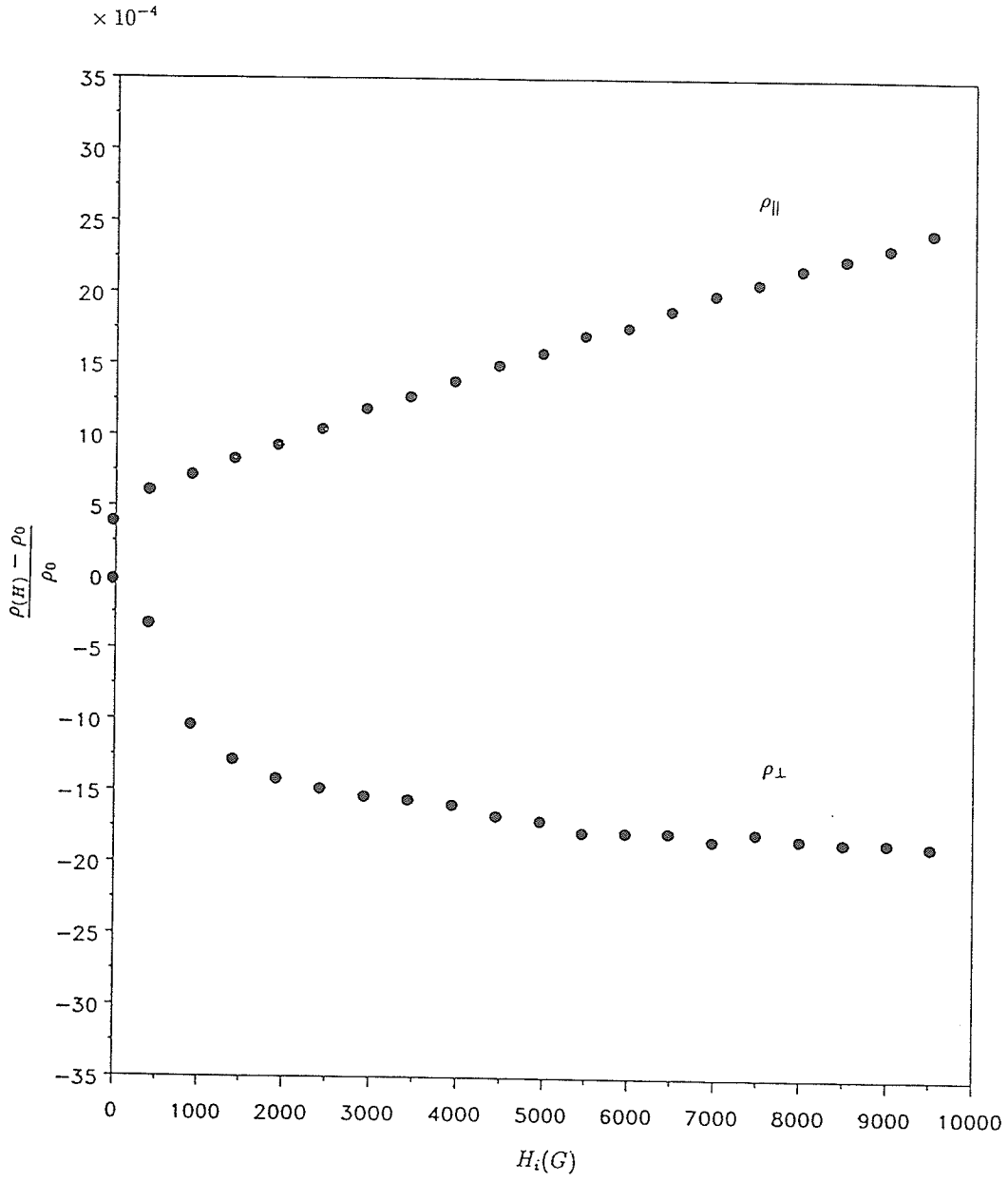

Figure A 4: Magnetoresistivity ratio vs. H_i for $Fe_{92}Zr_8$ at $77K$.

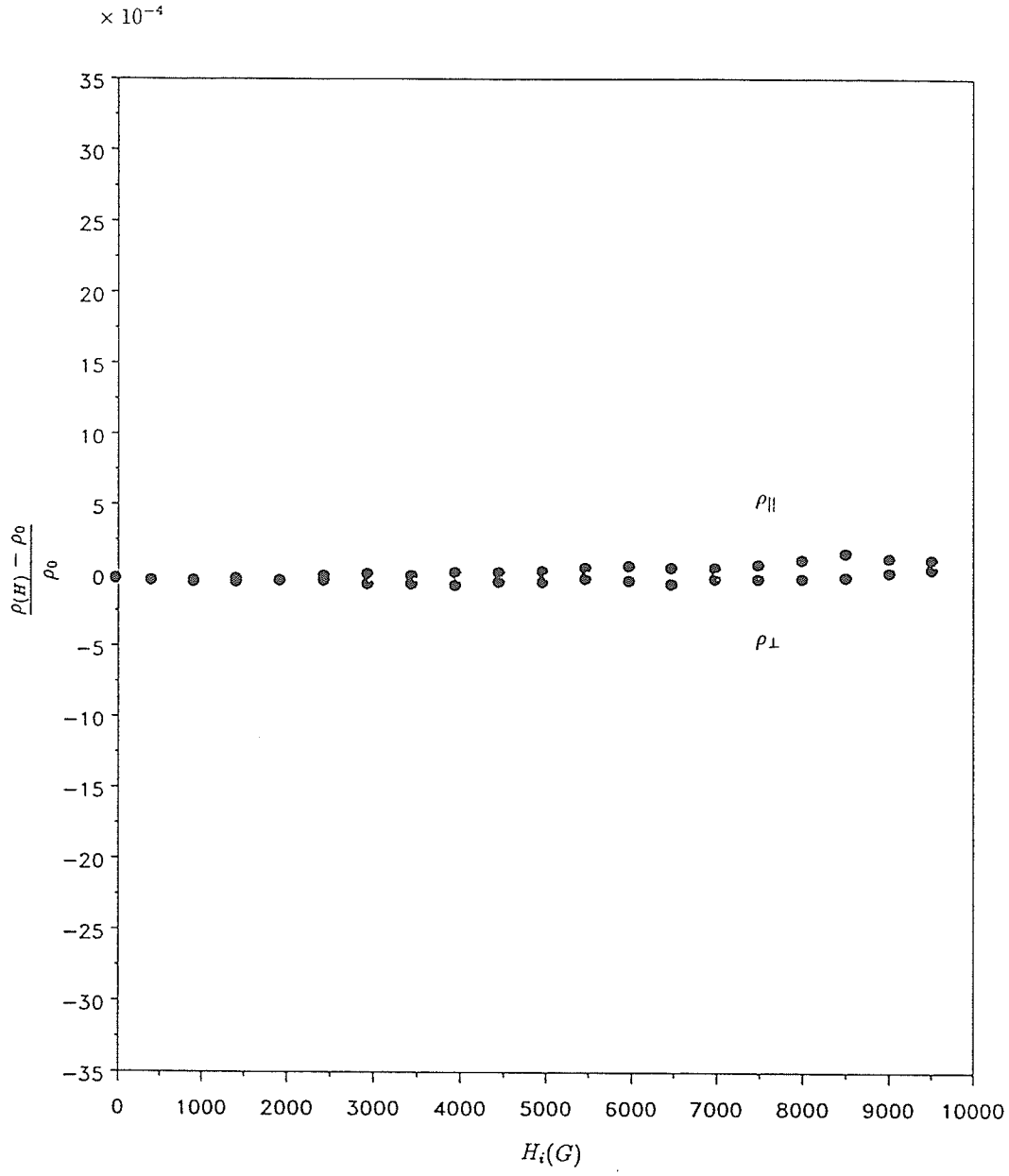

Figure A 5: Magnetoresistivity ratio vs. H_i for $Fe_{92}Zr_8$ at $295K$.

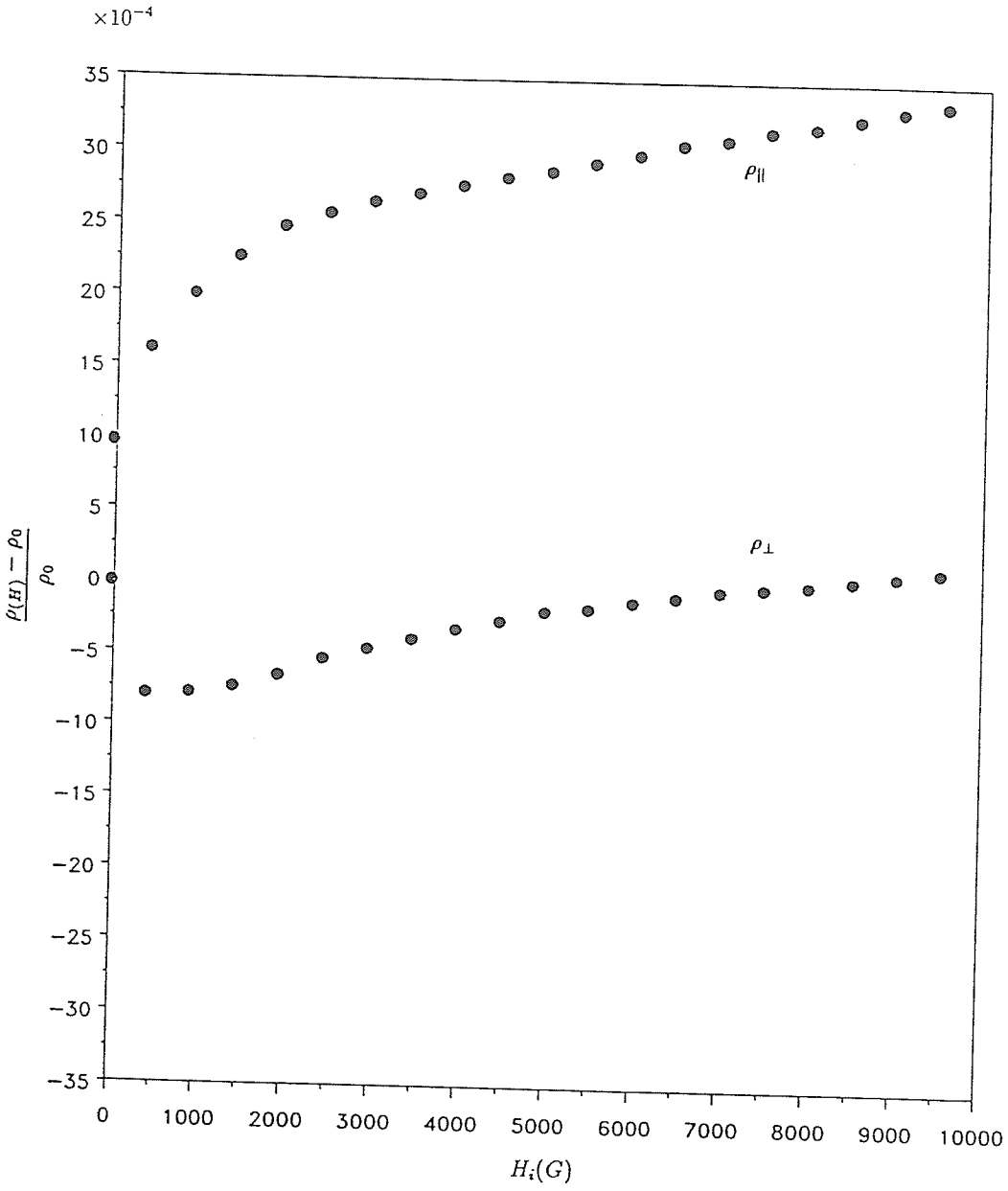

Figure A 6: Magnetoresistivity ratio vs. H_i for $Fe_{91}Zr_9$ at $1.5K$.

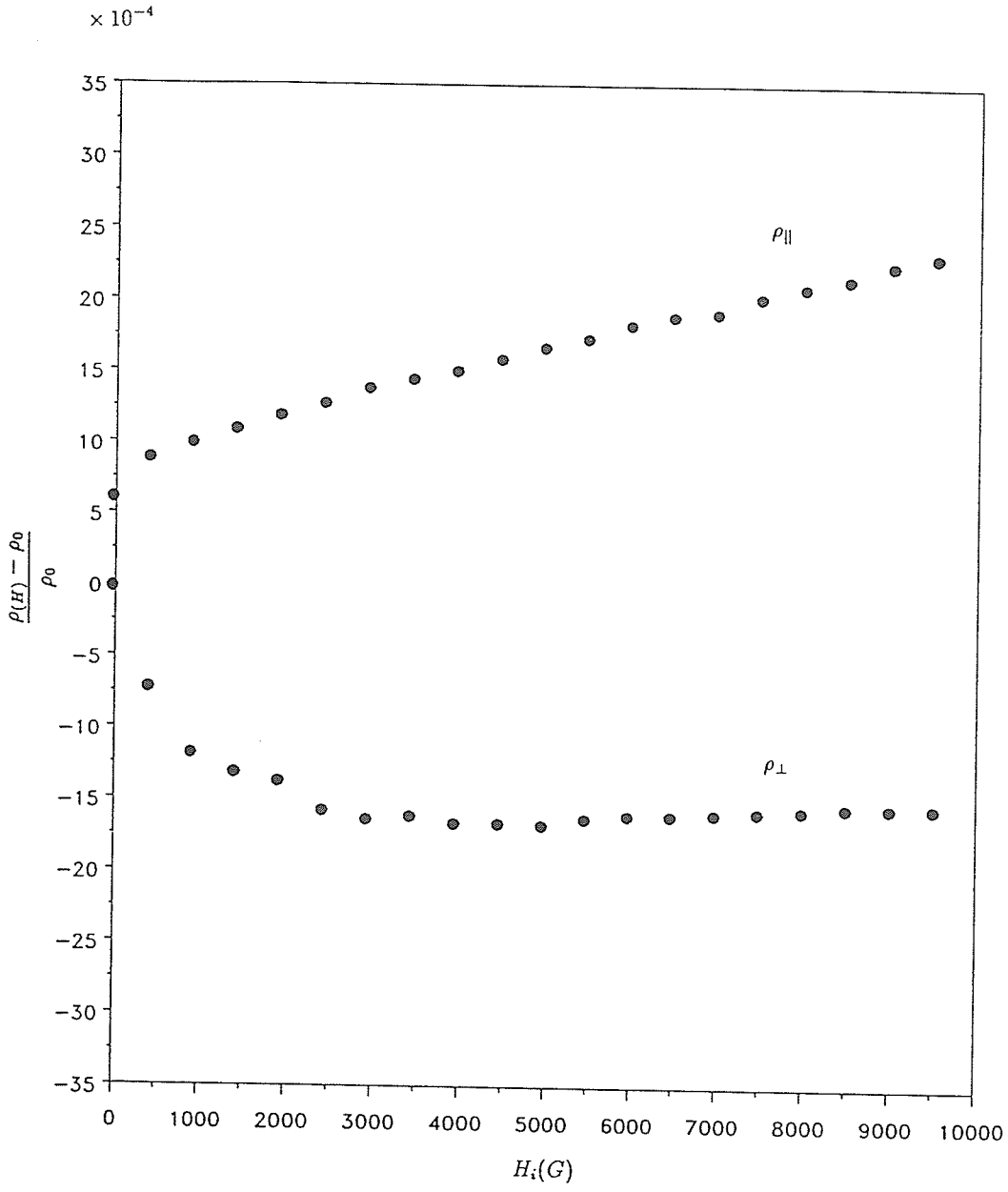

Figure A 7: Magnetoresistivity ratio vs. H_i for $Fe_{91}Zr_9$ at $4.2K$.

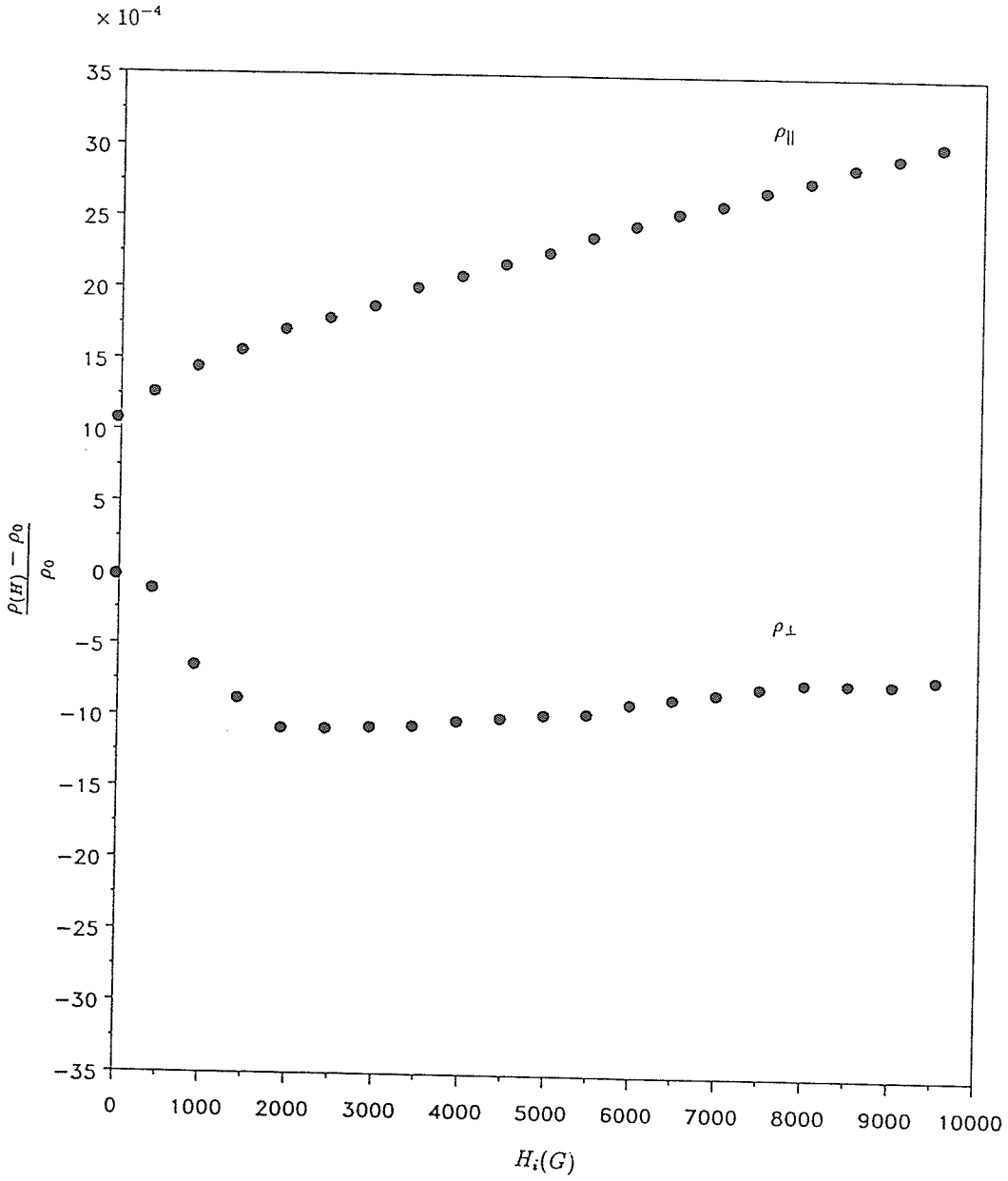

Figure A 8: Magnetoresistivity ratio vs. H_i for $Fe_{91}Zr_9$ at $60K$.

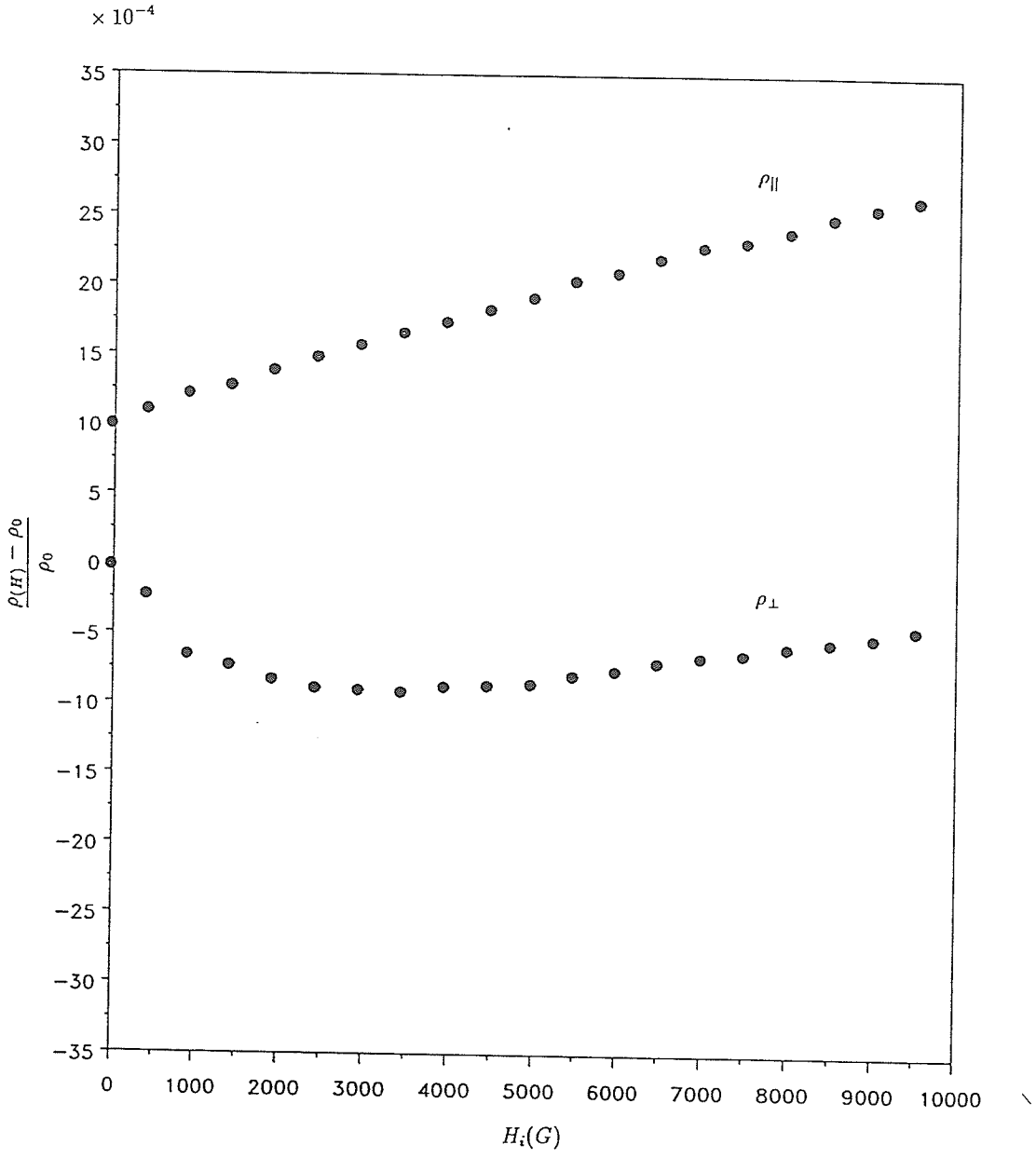

Figure A 9: Magnetoresistivity ratio vs. H_i for $Fe_{91}Zr_9$ at $77K$.

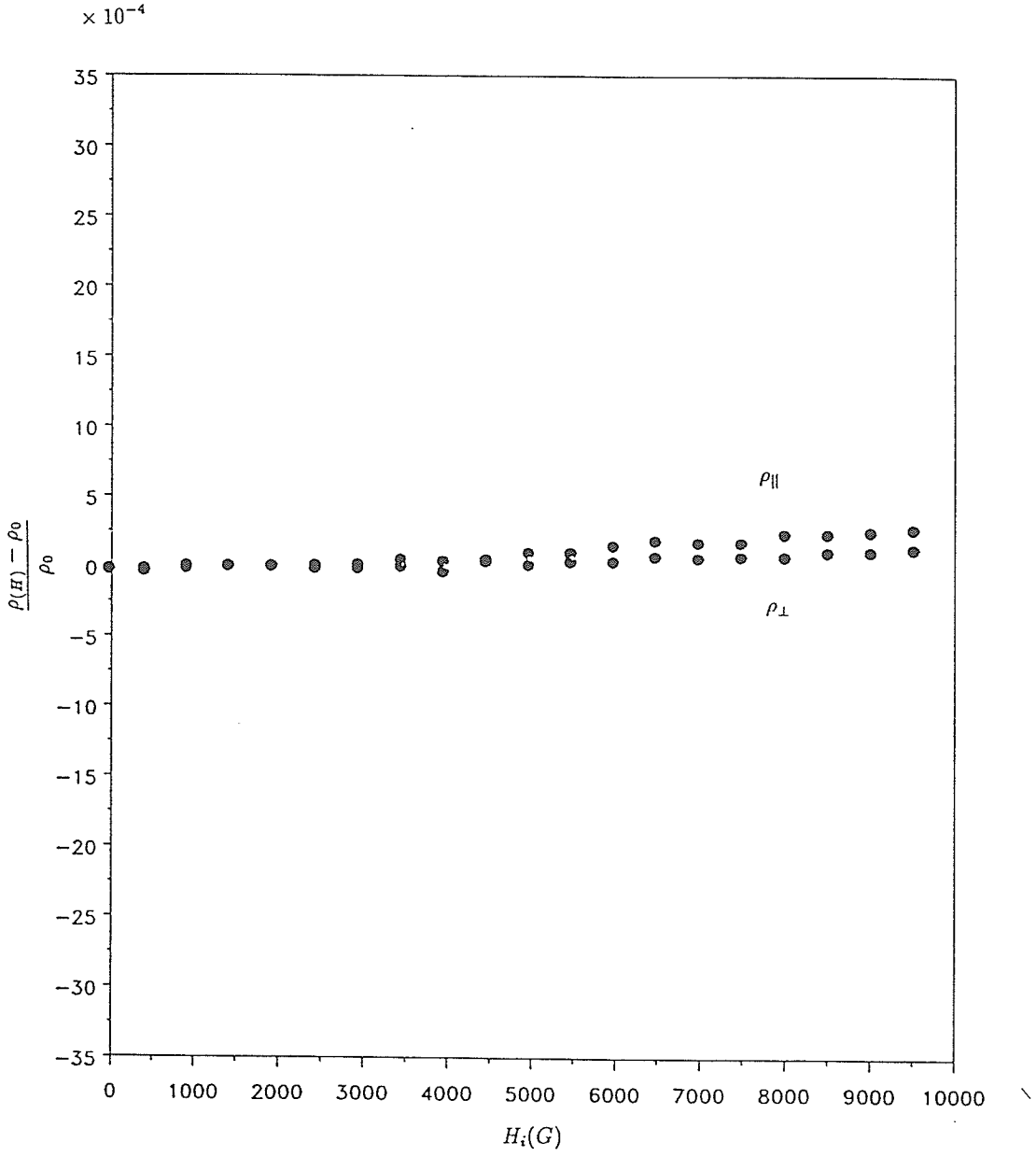

Figure A 10: Magnetoresistivity ratio vs. H_i for $Fe_{91}Zr_9$ at $295K$.

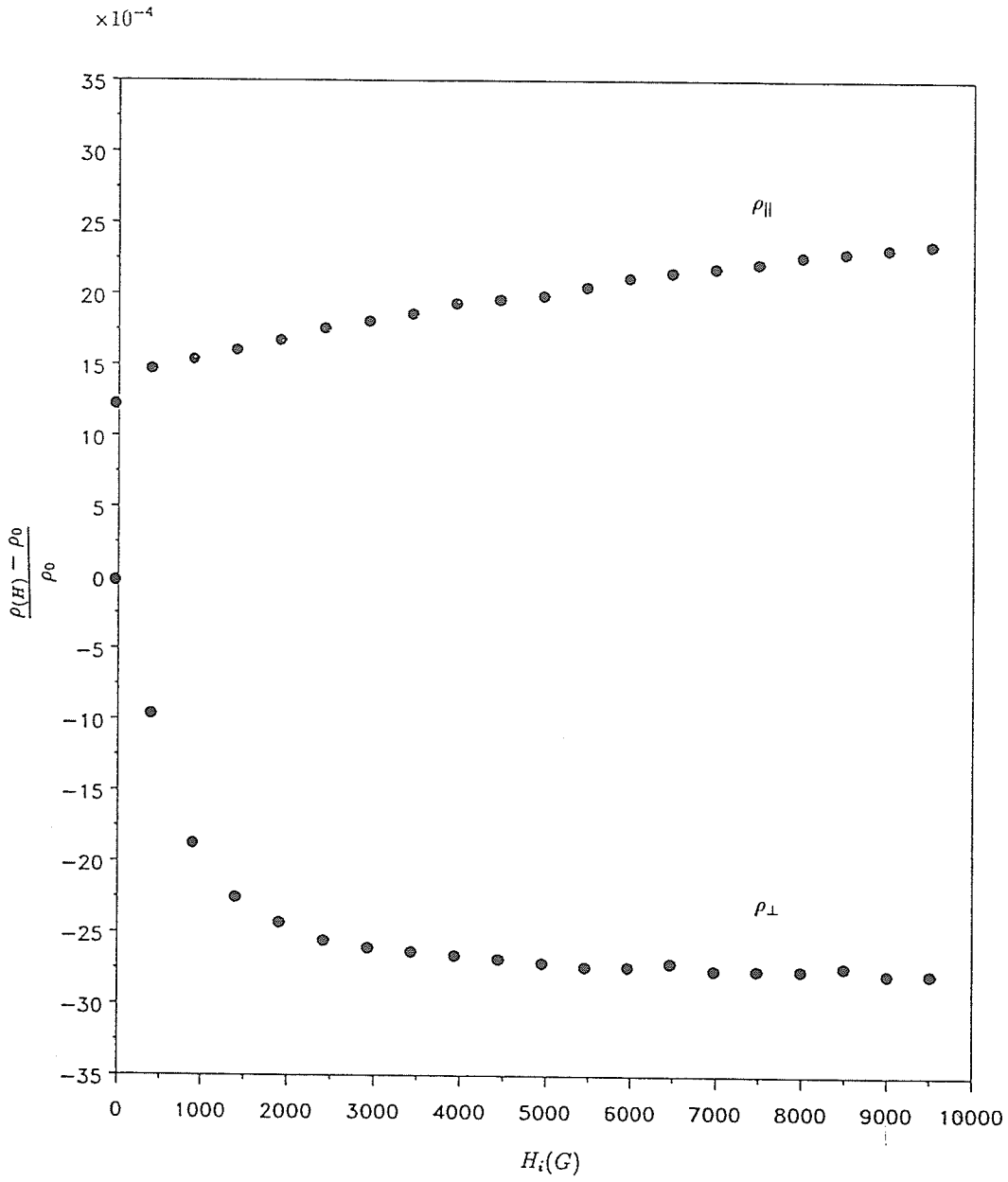

Figure A 11: Magnetoresistivity ratio vs. H_i for $Fe_{90}Zr_{10}$ at $1.5K$.

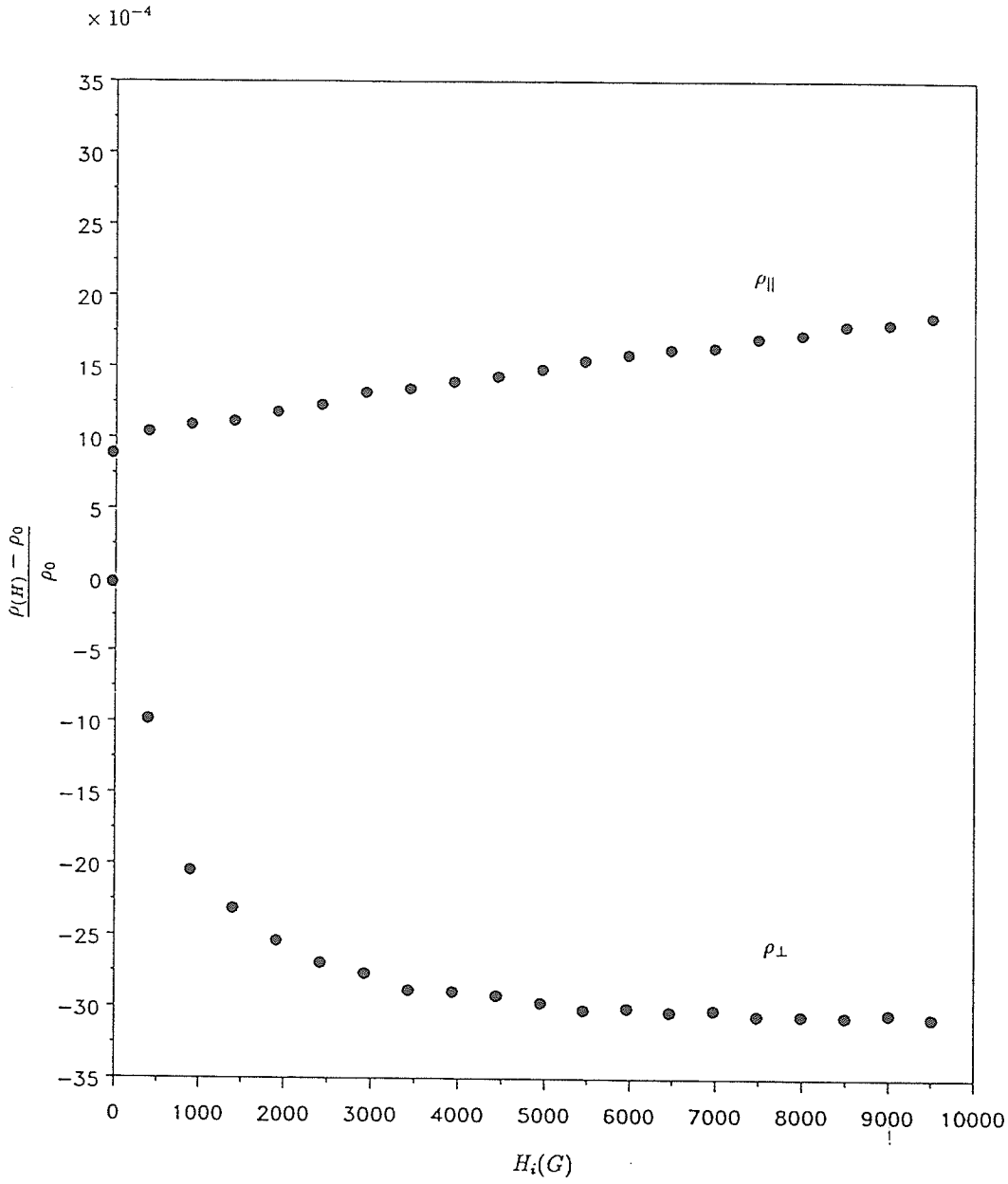

Figure A 12: Magnetoresistivity ratio vs. H_i for $Fe_{90}Zr_{10}$ at $4.2K$.

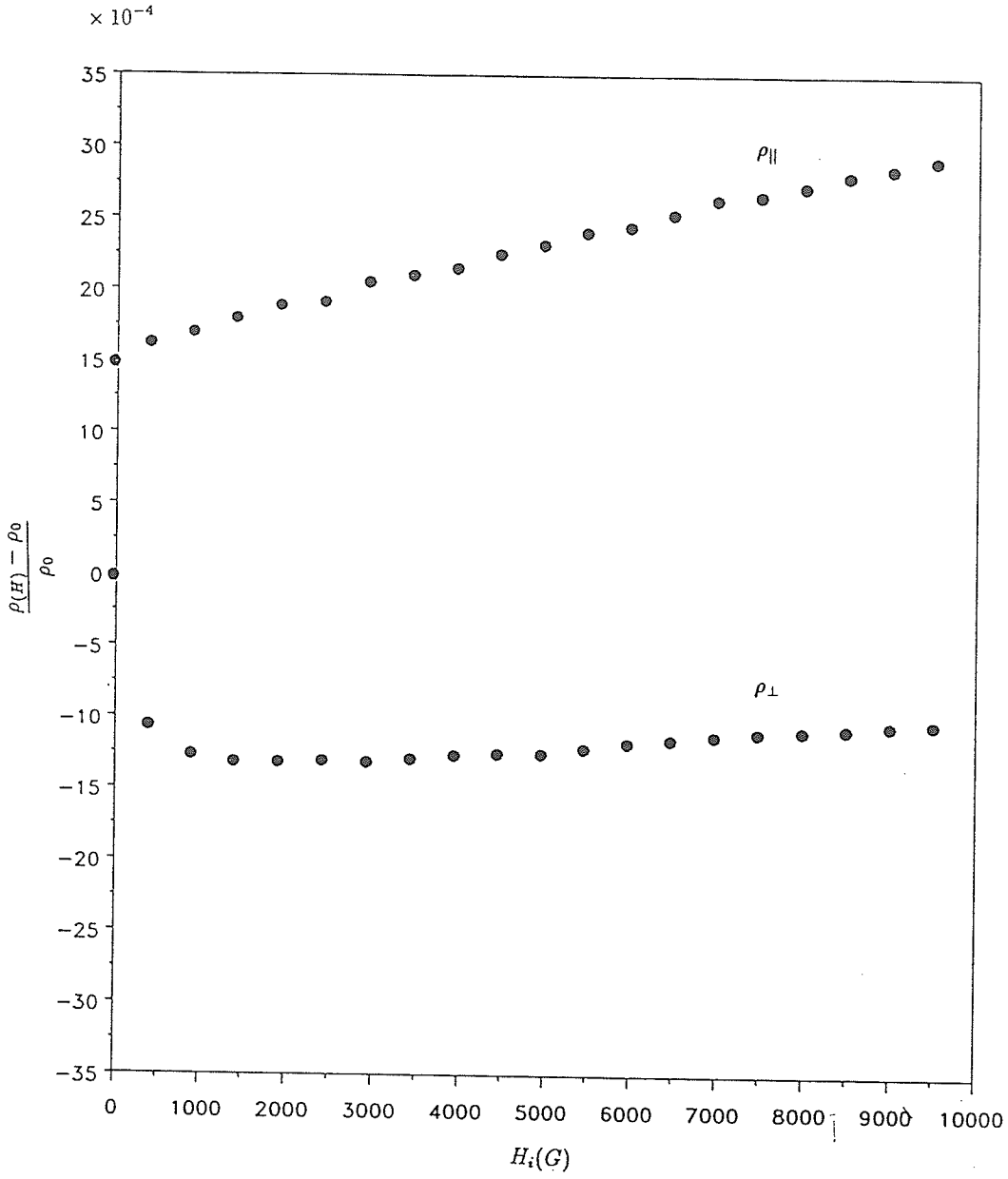

Figure A 13: Magnetoresistivity ratio vs. H_i for $Fe_{90}Zr_{10}$ at $60K$.

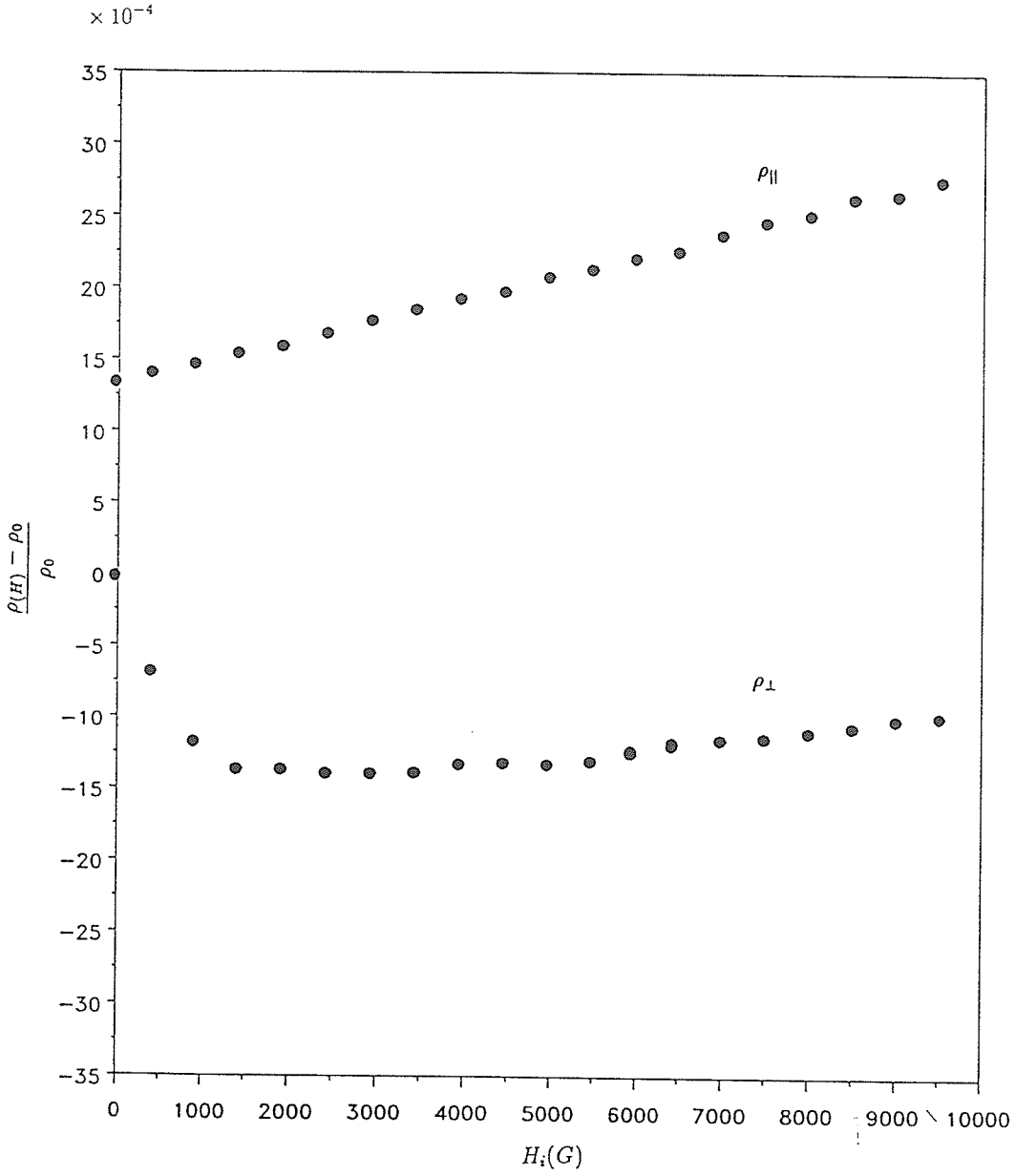

Figure A 14: Magnetoresistivity ratio vs. H_i for $Fe_{90}Zr_{10}$ at $77K$.

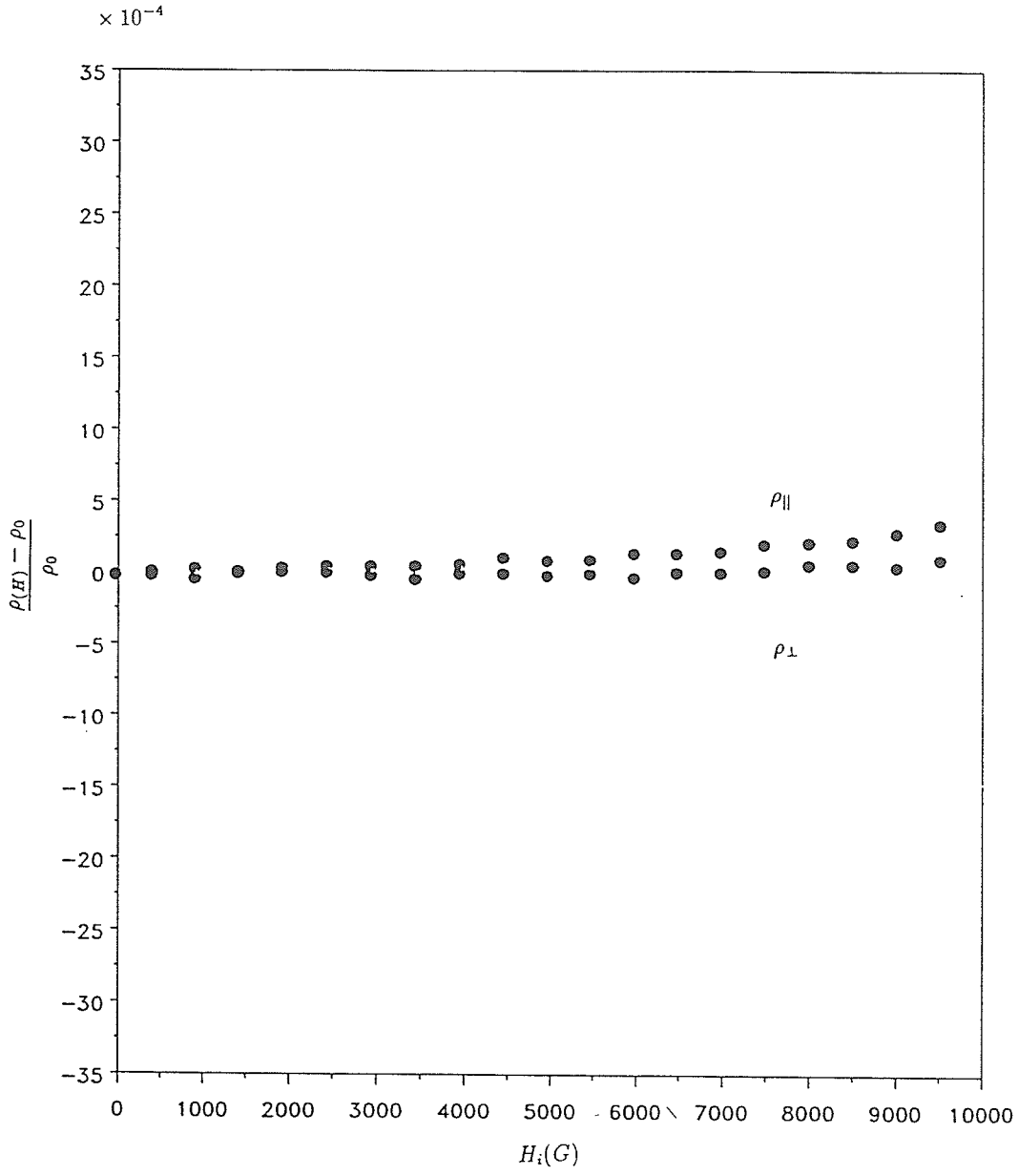

Figure A 15: Magnetoresistivity ratio vs. H_i for $Fe_{90}Zr_{10}$ at $295K$.

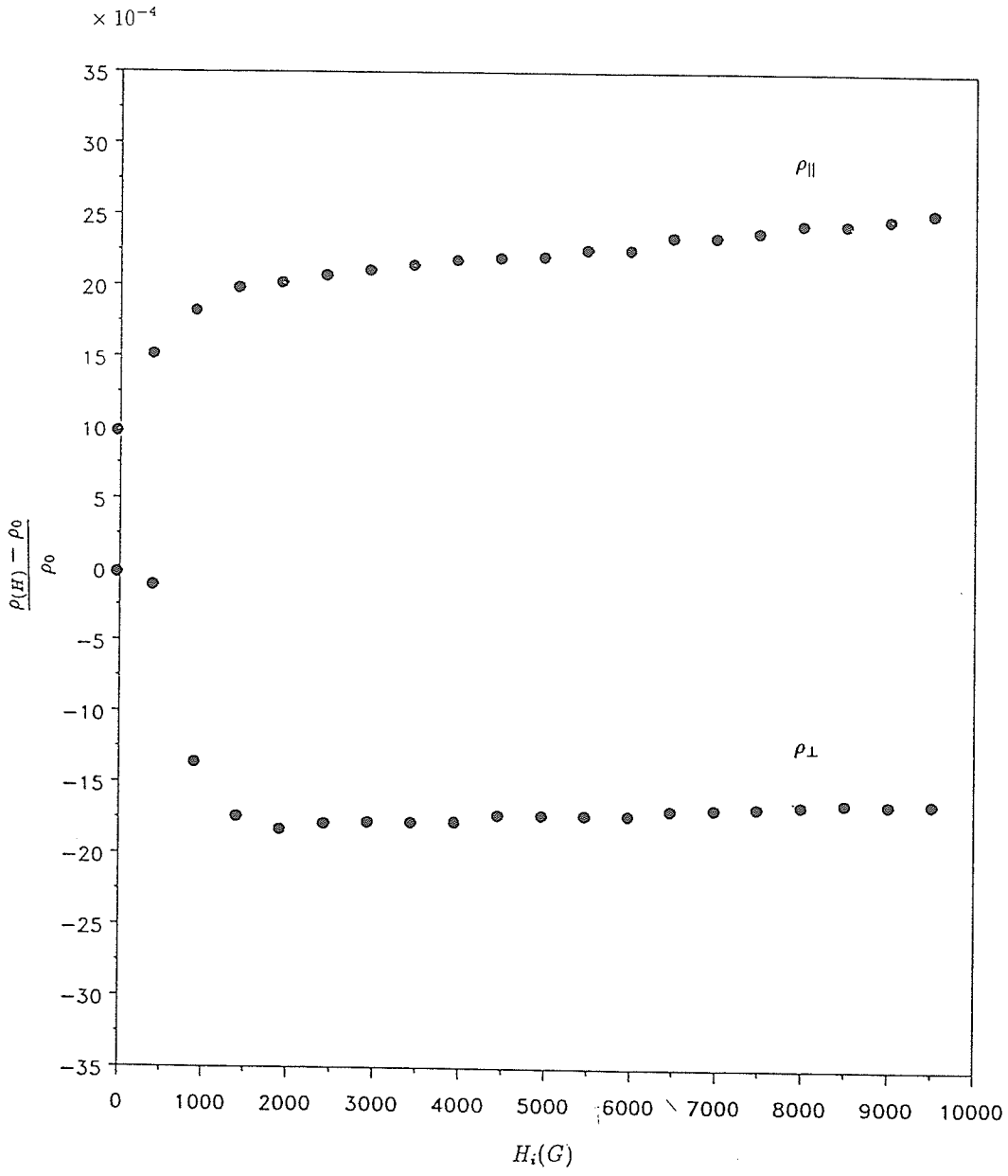

Figure A 16: Magnetoresistivity ratio vs. H_i for $Fe_{89}Zr_{11}$ at $1.5K$.

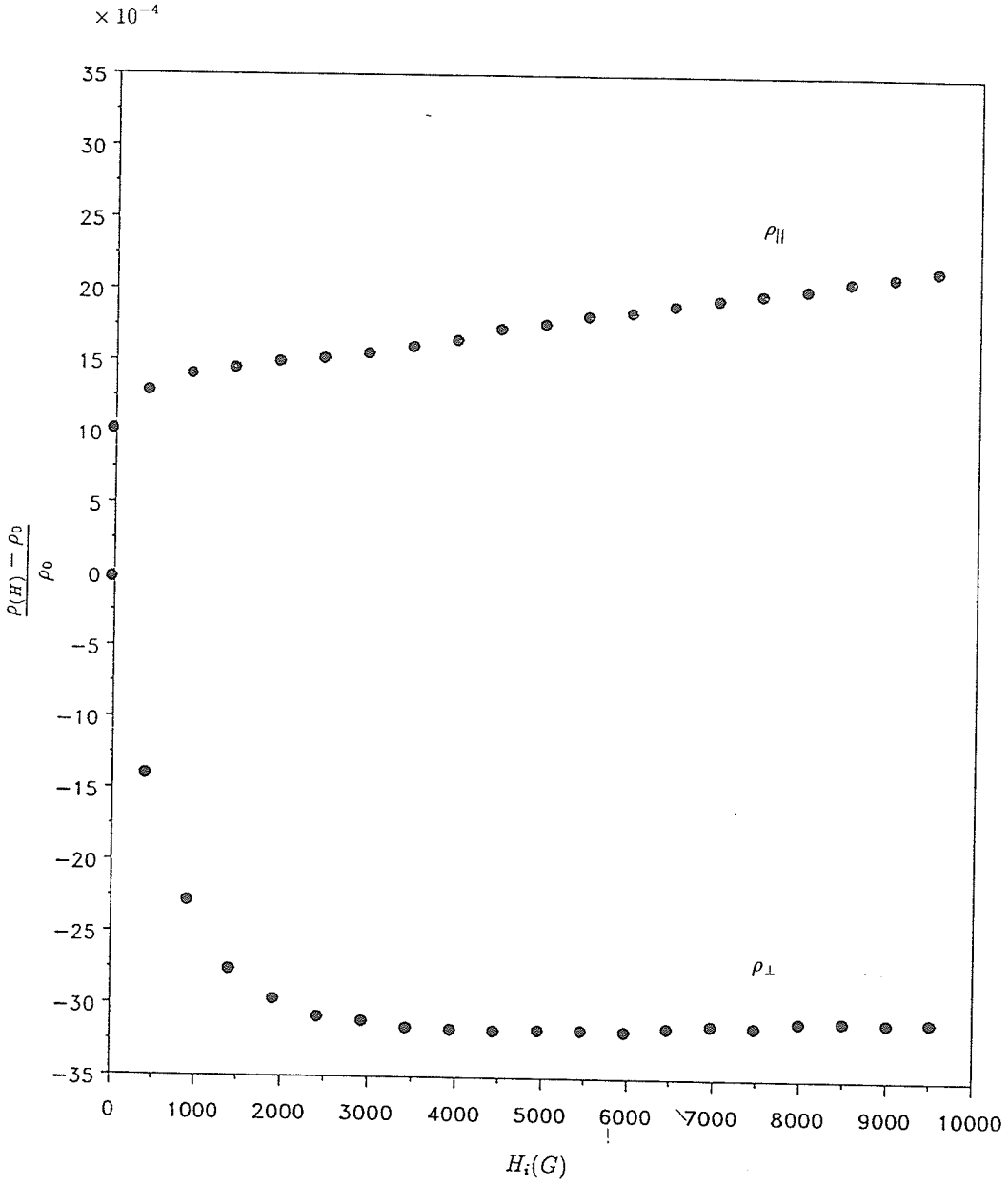

Figure A 17: Magnetoresistivity ratio vs. H_i for $Fe_{89}Zr_{11}$ at $4.2K$.

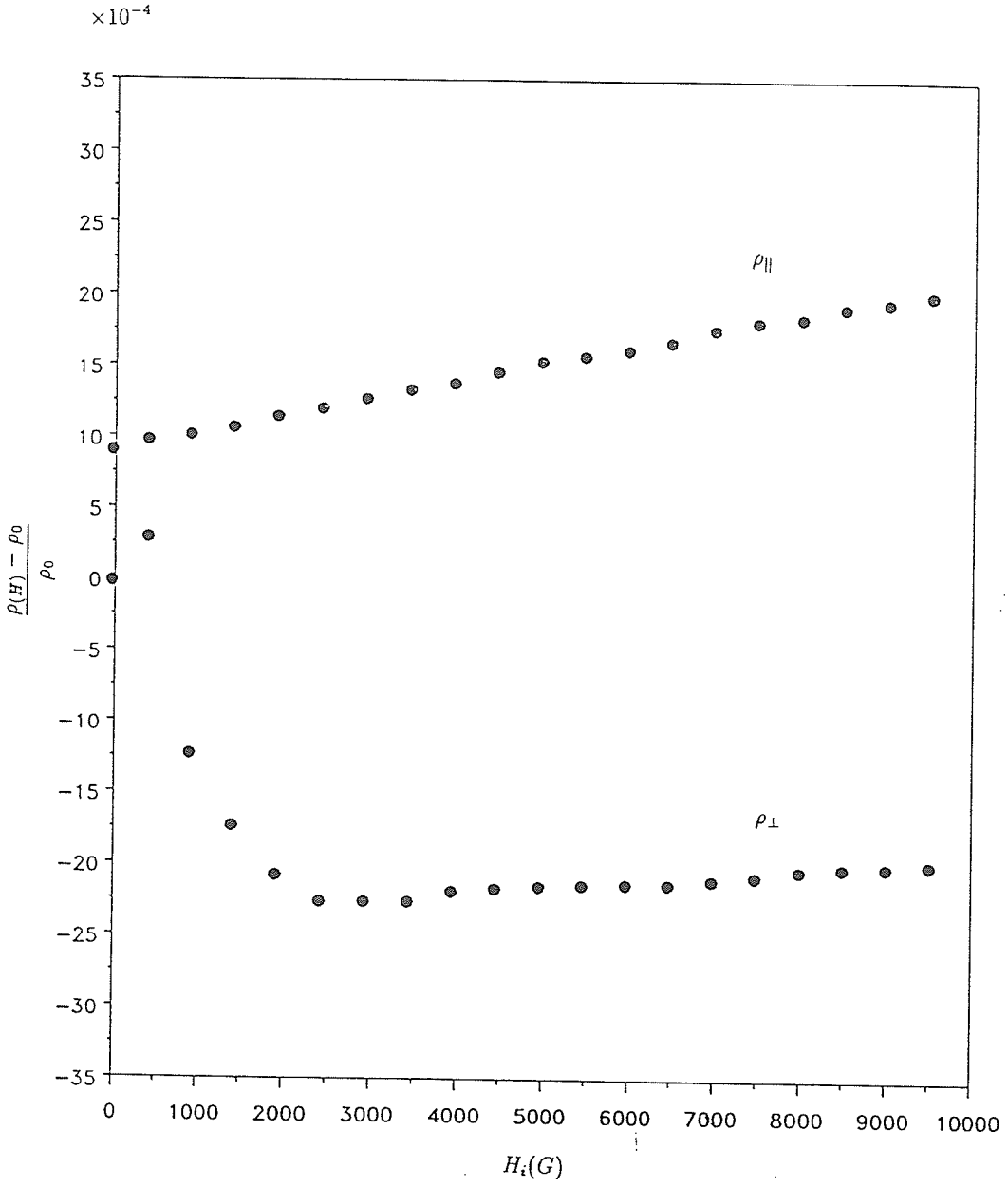

Figure A 18: Magnetoresistivity ratio vs. H_i for $Fe_{89}Zr_{11}$ at $60K$.

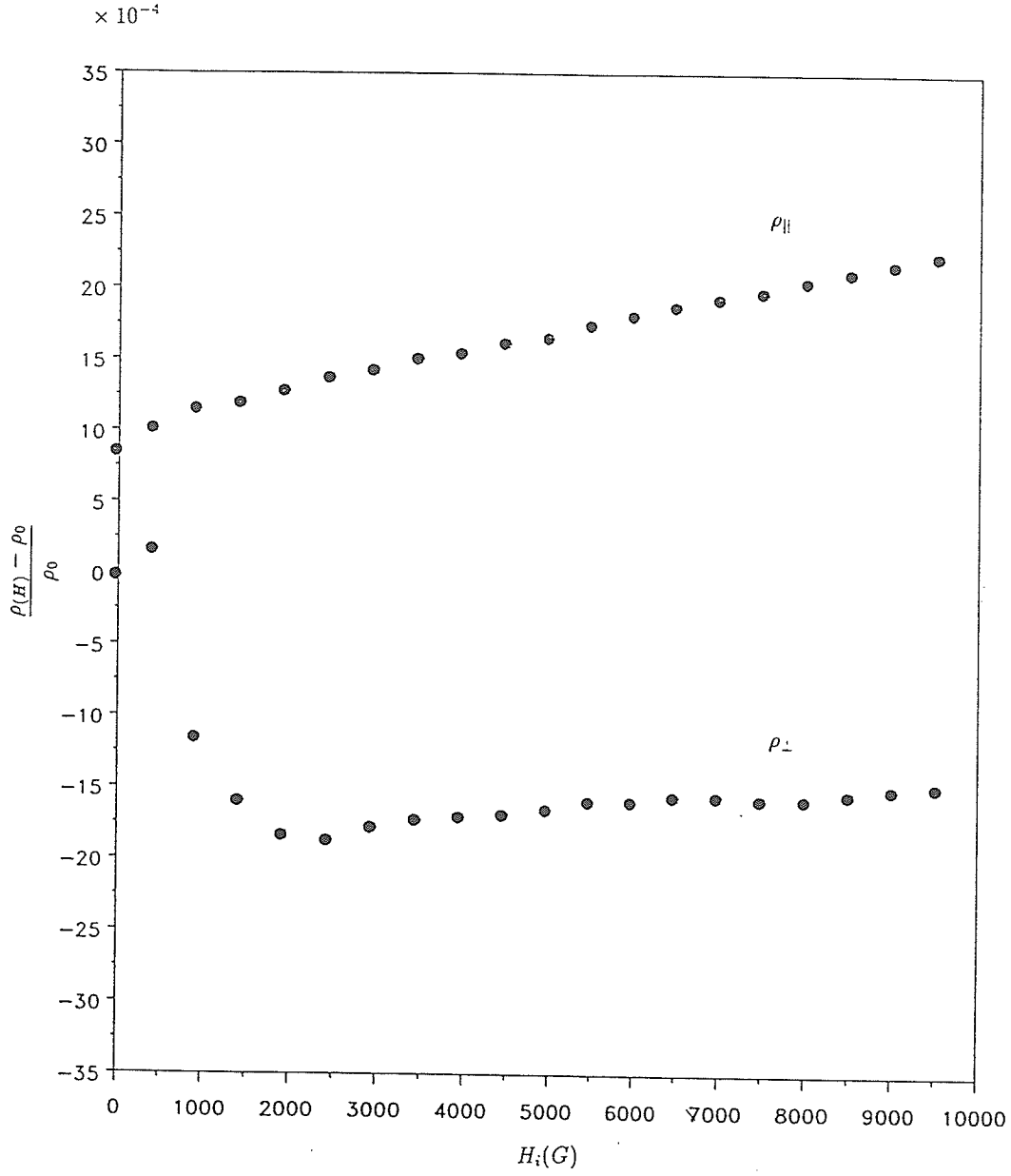

Figure A 19: Magnetoresistivity ratio vs. H_i for $Fe_{89}Zr_{11}$ at $77K$.

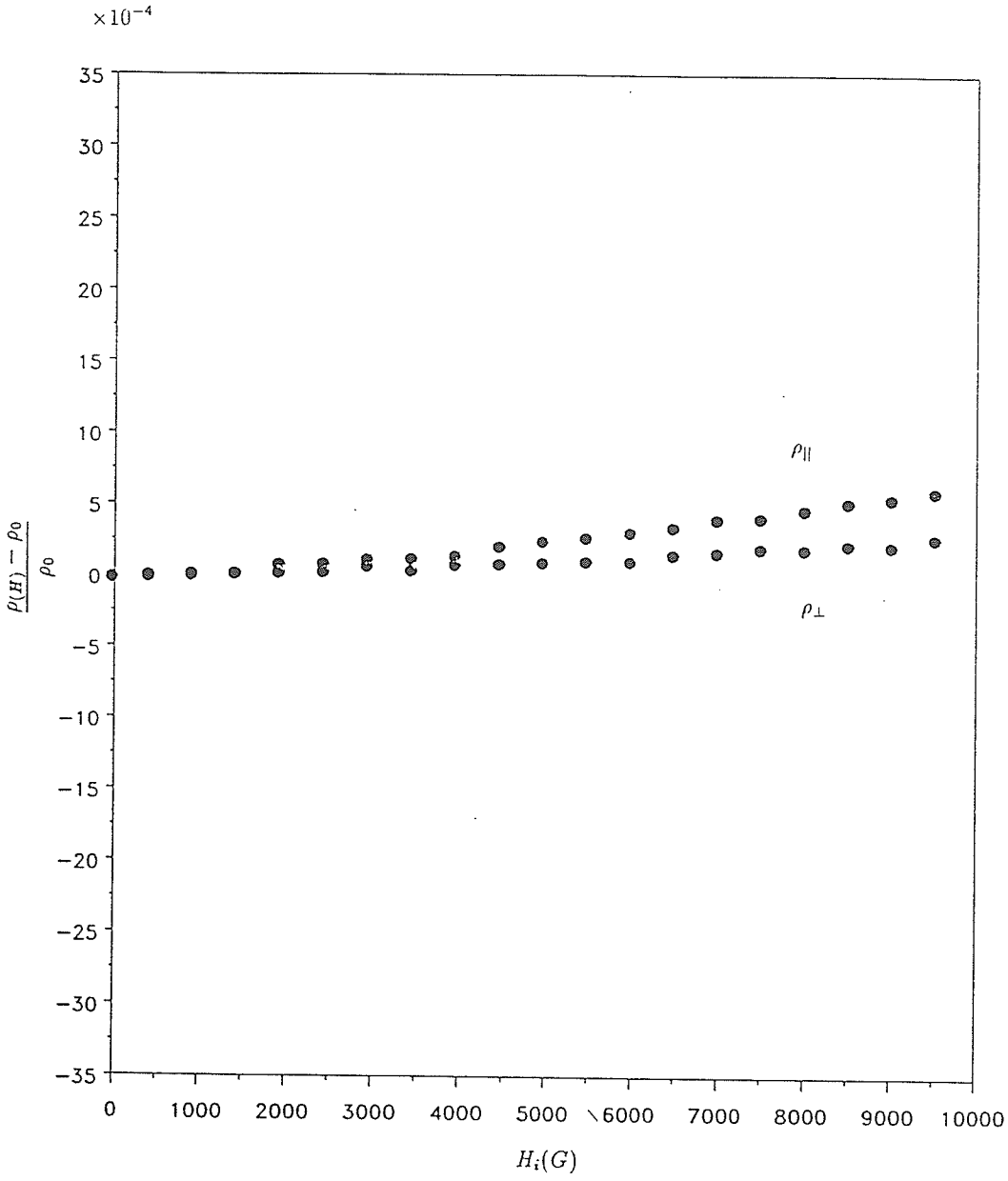

Figure A 20: Magnetoresistivity ratio vs. H_i for $Fe_{89}Zr_{11}$ at $295K$.